Numerical Simulation of Flame-Vortex Interactions in Natural and Synthetic Gas Mixtures

A Thesis
Presented to
The Academic Faculty

by

Justin D. Weiler

In Partial Fulfillment
of the Requirements for the Degree
Master of Science

School of Aerospace Engineering
Georgia Institute of Technology
July 2004

Numerical Simulation of Flame-Vortex Interactions in Natural and Synthetic Gas Mixtures

Approved by:

Suresh Menon, Committee Chair

Timothy Lieuwen

Jerry Seitzman

Date Approved: July 23, 2004

This work is dedicated to all of my friends and family ... those who have come and gone, those who have always been there, and those whom I've yet to meet.

ACKNOWLEDGEMENTS

The work presented here is the culmination of countless research hours, abstract ideas, small successes, and equally-important failures. In the end, none of it would have been possible without the support and dedication of everyone involved. To all of you, I am greatly indebted.

I would like to thank my research advisor, Dr. Suresh Menon, for having confidence in my research, and for extending his support when I "started over" on a new project halfway through. His hands-off approach - while challenging at first - forced me to think beyond simplistic convention and proved to be one of the most valuable lessons. I would also like to thank the members of my advisory committee, Dr. Tim Lieuwen and Dr. Jerry Seitzman, for taking the time to review my work and expressing a genuine interest in the project.

I owe special thanks to two of my closest friends, Dr. Chris Stone and Matthieu Masquelet, for making my time in Atlanta much more enjoyable, both in and out of work. Most would consider a *Southerner*, a *Frenchman*, and a *Yankee* living under the same roof bizarre and, at best, unlikely. I consider it a true testament to friendship.

I extend sincere gratitude and best wishes to all of my friends and colleagues in the CCL. Much of my work would not have been possible without the work of those who came before me. I want to thank Dr. Vaidyanathan Sankaran for his tireless commitment to the success of my work, as well as all of the senior students with whom I spent many hours debating, arguing, and eventually collaborating on a number of things (especially those nagging chemistry models).

While the group of students that I entered Tech with has grown thin, two individuals have remained alongside me the entire way - in class, at work, on weekends, and into the wee hours of the morning. My respect for Hossam El-Asrag and Martin Sanchez Rocha goes well beyond words, so I will simply say thank you, and wherever I go, you'll always have a friend.

Two people I cannot thank enough are my parents, Gary and Robin Weiler. Their enduring support and unremitting confidence in my many endeavors are the primary reason that I've made it this far. For years they attempted to instill in me that success in life is not what you make ***for*** yourself, but what you make ***of*** yourself. After 7 years of college, I'm glad to say that I have finally learned something.

Last, but certainly not least, I want to thank my fiancé and soon-to-be wife Jamie Lane Wallace. In the face of adversity, she has always put her best foot forward, and given no less than 100% of herself. In my time at Georgia Tech, we have had many ups and downs, but long distances can do that. Now, I look forward to our future, and to the life that I've been waiting to start since the day I first left home ... seven long years ago.

TABLE OF CONTENTS

LIST OF TABLES

LIST OF FIGURES

SUMMARY

The interactions between laminar premixed flames and counter-rotating vortex pairs in natural and synthetic gas mixtures have been computationally investigated through the use of Direct Numerical Simulations and parallel processing.

Using a computational model for premixed combustion, laminar flames are simulated for single- and two-component fuel mixtures of methane, carbon monoxide, and hydrogen. These laminar flames are forced to interact with superimposed laminar vortex pairs, which mimic the effects of a pulsed, two-dimensional slot-injection. The premixed flames are parameterized by their unstretched laminar flame speed, heat release, and flame thickness. The simulated vortices are of a fixed size (relative to the flame thickness) and are parameterized, solely, by their rotational velocity (relative to the flame speed).

Strain rate and surface curvature measurements are made along the stretched flame surfaces to study the effects of additive *syngas* species (CO and H_2) on lean methane-air flames. For flames that share the same unstretched laminar flame speed, heat release, and flame thickness, it is observed that the effects of carbon monoxide on methane-air mixtures are essentially negigible while the effects of hydrogen are quite substantial.

The dynamics of stretched CH_4/Air and $CH_4/CO/Air$ flames are nearly identical to one another for interactions with both strong and weak vortices. However, the $CH_4/H_2/Air$ flames demonstrate a remarkable tendency toward surface area growth. Over comparable interaction periods, the flame surface area produced during interactions with $CH_4/H_2/Air$ flames was found to be more than double that of the pure CH_4/Air flames. Despite several obvious differences, all of the interactions revealed the same basic phenomena, including vortex breakdown and flame pinch-off (i.e. pocket formation).

In general, the strain rate and surface curvature magnitudes were found to be lower for the $CH_4/H_2/Air$ flames, and comparable between CH_4/Air and $CH_4/CO/Air$ flames.

Rates of flame stretching are not explicitely determined, but are, instead, addressed through observation of their individual components.

Two different models are used to determine local displacement speed values. A discrepancy between practical and theoretical definitions of the displacement speed is evident based on the instantaneous results for CH_4/Air and $CH_4/H_2/Air$ flames interacting with weak and strong vortices.

NOMENCLATURE

Roman Symbols

A	surface area
A_F	flame surface-growth factor
c	speed of sound
c_f	(fuel) progress variable
$C_p,\ C_v$	constant-pressure and constant-volume specific heats
C_k	normalized concentration of kth species
d_c	vortex core diameter
D_k	diffusion coefficient of kth species
$E,\ e_i$	total and internal energies
E_A	reaction activation energy
$f()$	mathematical function of ()
$\mathbf{F}$	flux vector
$h_k,\ h^0_{f,k}$	static and formation enthalpies
K	stretch rate
K_c	stretch due to curvature
K_s	stretch due to strain
K_{glob}	global flame stretch rate
Le	Lewis number
L_x, L_y	physical x and y dimensions
$m_k,\ \bar{m}$	species and average molecular masses
M	Mach number
MW_k	molecuar weight of kth species
$\vec{n},\ n_i$	unit normal vector
N^p_x, N^p_y	number of x and y gridpoints

N_s	number of chemical species
p	static pressure
p_∞	far-field pressure
Pr	Prandtl number
$\mathbf{Q}$	state variable vector
q_i	heat flux vector
r_c	vortex core radius
$R,\ \bar{R}$	universal and specific gas constants
RR_k	normalized reaction rate of kth species
s_f	2-D flame arc length
Sc	Schmidt number
S_d	flame displacement speed
S_L	laminar flame speed
S_T	turbulent flame speed
T	static temperature
u'	velocity fluctuation
$\vec{u},\ u_i$	velocity vector
U_θ	rotational velocity
V	closed or control volume
$\dot{w}_k$	chemical source of kth species
x_n	normalized 2-D flame arc length
Y_k	mass fraction of kth species
z	mixture fraction

Greek Symbols

α	thermal diffusivity
β	characteristic length of Lamb vortex
χ_k	molar fraction of kth species

δ_F	flame thermal thickness
δ_{RZ}	reaction zone thickness
δ_{ij}	Kronecker delta
Δ	discrete differential
Δt	computational timestep
ε	NSCBC pressure recovery constant
ϕ	equivalence ratio
$\mathbf{\Phi}$	source term vector
κ	thermal conductivity
λ_i	NSCBC wave speed vector
μ	dynamic viscosity
ν	kinematic viscosity
ψ	Arrhenius constant (empirical)
θ	Arrhenius chemical rate
ρ	fluid density
τ_{ij}	viscous stress tensor
$\vec{\omega}$	vorticity vector
Ω	vorticity attenuation parameter

Math Script Symbols

$\mathscr{B}$	all non-derivative terms in the i_{th} NSCBC wave
$\mathscr{L}$	NSCBC wave amplitude variation vector
$\mathscr{R}$	ISAT retrieval rate
$\mathscr{S}$	computational speedup

Superscripts

u	unstretched value

0	initial/steady-state value
t	value at time t
T	matrix/vector transpose
n (*time integ.*)	discrete time level
$*$ (*time integ.*)	predictor time level

Subscripts

i, j, k	Cartesian index
x, y, z	Cartesian directional
θ	rotational
k (*vector*)	sum of index terms (i,j,k)
k (*scalar*)	k^{th} species
L	laminar value

Mathematical Symbols

∂	partial derivative
$\sum$	mathematical sum
$\rightleftharpoons$	reversible reaction
∇	gradient operator
$\nabla \cdot \vec{f}$	divergence of vector $\vec{f}$
$\nabla \times \vec{f}$	curl of vector $\vec{f}$
$\int_V$	volume integral
$\oint_S$	surface integral

Abbreviations and Acronyms

CFD	Computational Fluid Dynamics

DNS	Direct Numerical Simulation
DI	direct numerical integration
$ECBC$	Euler Characteristic Boundary Conditions
FGV	flame-generated vorticity
(F/A)	fuel-to-air ratio
H/C	hydrocarbon
$ISAT$	*In Situ Adaptive Tabulation*
$LODI$	local one-dimensional inviscid
$NSCBC$	Navier-Stokes Characteristic Boundary Conditions
UHC	unburned hydrocarbon

CHAPTER I

INTRODUCTION

Most fields of scientific research draw knowledge from multiple disciplines. Turbulent combustion is certainly no exception. It is the combination of turbulent flows and combustion, two very complicated, and often perplexing, physical phenomenon. The study of either phenomena provides a sound degree of difficulty that is rivaled only by the study of their interaction with one another. To understand their individual behavior is to understand only a small part of most physical combustion processes.

A majority of combustion processes take place in turbulent flows. The interactions between fluid motion and chemical reaction is as dynamic as the flow itself. For example, a disturbance issued toward a uniform reaction layer will likely cause non-uniformity throughout that reaction layer. This leads to either attenuation of the disturbance or further disruption of the adjacent fluid. In either case, it is clear that neither fluid motion nor chemical reaction are passive with respect to one another.

The nature of fluid-flame interactions also depends on the particular frame of interest. On a global scale, the fluid responds to the geometry and input flow characteristics of the combustion device. On a local scale, the fluid responds to neighboring fluid motion, as well as thermo-chemical gradients in the vicinity of the flame. The former is generally regarded as an engineering problem, while the latter- representing a focal point of this study- is regarded as a scientific problem.

Whether you're considering global, or local fluid-flame interactions, the choice of fuel can have a considerable effect on this interaction. The use of hydrocarbon (H/C) fuels in practical combustion devices, such as gas turbines and internal combustion engines, is an enduring practice. However, growing environmental concerns have prompted the consideration of alternative fuel sources for energy production. Hydrogen heads up a short list of alternative fuels with the potential to provide adequate energy and simultaneously

reduce harmful pollutant emissions that are characteristic of hydrocarbon fuel combustion.

The quality and availability of hydrogen fuel generally depend on two factors: the cost of production, and the method of acquisition. Purification techniques during production carry a greater price tag, therefore, the need for increased quality mandates a higher cost. One technique for hydrogen production that has recently been investigated is the production of synthetic gas (commonly referred to as *syngas*) from natural gas. This particular technique is of interest to the current study primarily for its affiliation with methane (a widely-studied, clean-burning fuel) and for specific characteristics of the resulting mixture.

Further discussion regarding *syngas* characteristics, and the physics of fluid-flame interactions is provided throughout this chapter. Beyond scientific discussion, the distinguishing features and specific objectives of this study are also addressed.

1.1 Natural and Synthetic Gases

Natural gas has been extensively studied and employed in combustion processes ranging from home heating to internal combustion engines. Although it is regarded as one of the cleaner, more-efficient fuels in use, natural gas combustion still presents two long-term considerations: (1) renewability, and (2) the inevitable release of harmful pollutants including carbon monoxide, CO, nitrogen oxides, NO_x, and unburned hydrocarbons, $UHCs$, which can result from inefficient, or incomplete combustion. In terms of availability, natural gas is one of the Earth's most abundant fossil fuels, and requires relatively little processing prior to use [3]. However, recent energy studies have shown that natural gas meets upward of 30% of the energy demand in the United States alone [4]. Increased energy needs, coupled with receding supply and interest in petroleum-based counterparts, may drive such figures even higher in the coming years [5].

Synthetic gas (a.k.a. synthesis gas or *syngas*) is a term used to describe the general mixture that is produced during the formation of gaseous hydrogen, H_2, from processed H/C fuels. More specifically, processes such as steam reformation ($CH_4 + H_2O + heat$) and dry reformation ($CH_4 + CO_2 + heat$) of natural gas [6] result in the production of H_2, CO, and any variety of carbon dioxide, CO_2, water vapor, H_2O, and nitrogen, N_2, that are

derived from partial oxidation of methane, CH_4 [7]. According to James et al. [8], natural gas is the primary resource for *syngas* production. However, several other materials, such as coal, oil, solid waste, and wood, are being investigated as potential H/C sources.

The direct production of *syngas* from subterranean natural gas often requires the removal of naturally-present sulfur concentrations to prevent the emission of sulfur dioxide, SO_2, into the atmosphere. Production by steam or dry reformation can be accomplished using the waste heat and product concentrations (H_2O and CO_2) of other H/C-fueled processes such as natural gas turbines. As mentioned earlier, the final *syngas* composition depends greatly on the manner in which it is produced. As with most practical analyses, the study contained herein assumes natural gas to be composed primarily of methane, and *syngas* to be a combination of strictly carbon monoxide and hydrogen gas, having negligible product concentrations related to H/C oxidation.

1.2 Flame-Vortex Interactions

The flame-vortex interaction is a very useful tool for analyzing the physics of stretched flame surfaces. In addition, the premise upon which it is applied is quite simple. A two-dimensional, laminar, counter-rotating vortex pair (a.k.a. *toroid*) is convected toward a planar flame front and the two make contact with one another, resulting in areodynamic stretching of the flame surface. Although vortex pairs and flame fronts are naturally three-dimensional in space, the vortices generated here are essentially symmetric along their rotational axis and the flame initially propagates through a uniform reactant mixture, making it essentially planar. These assumptions are applied to both experimental and numerical studies, as will be further discussed in later sections.

Flame stretch is, perhaps, the primary phenomena associated with turbulent combustion. The goal of flame-vortex interactions is to address turbulent combustion on a fundamental level. This is accomplished by using a simplified flame and a simplified, non-uniform flowfield, both of which can be represented in 2-D. The use of laminar physics in representing turbulent phenomenon implies a degree of inconsistency. However, such a configuration

exploits the most-fundamental activity occurring along a turbulent flame front. That activity is individual fluid structures, locally interacting with a small segment of, what is essentially, a laminar flame surface.

1.2.1 Flame Stretch Definition

Perhaps, the most fundamental characteristic separating turbulent flames from laminar flames is the change in flame surface area. The term *flame stretch* (denoted by K) is synonymous with changes in flame surface area, as they are one in the same. As stated by Poinsot and Veynante [9], *flame stretch* also implies changes to the flame structure due to non-uniformity of the flowfield. Furthermore, it is defined by Candel and Poinsot [10] as the fractional rate of change of a particular flame surface element, which can be quantified as

$$K \equiv \frac{1}{A}\frac{dA}{dt} \tag{1}$$

where A represents the flame surface element of interest, and dt is a specified time period.

The non-uniformity of a divergent reactant stream (e.g. counterflow or stagnation flow) can result in a planar stretched flame. The divergent motion of fluid results in non-zero strain rates along the flame surface, and typically causes positive stretching, in which the flame surface area is increased ($dA > 0$). The mathematical equivalent of Eqn. 1 for purely-strained flames can be written as

$$K = \nabla_t \cdot \vec{u} \tag{2}$$

where ∇_t represents the tangential gradient operator acting on the local velocity vector, $\vec{u}$. Such studies of purely-strained flames are frequently used to catalog stretched flame characteristics for later use in turbulent flame analyses (e.g. modeling and simulation).

However, further examination of wrinkled, turbulent flame fronts has revealed that specific regions along the flame surface propagate at different speeds (e.g. Sinibaldi et al.

[11] and Echekki & Chen [12]). This variation has been linked to the local curvature of the flame front. The flame's orientation has a direct impact on thermo-chemical gradients in the vicinity of the reaction zone, and consequently changes its propagation characteristics. This effect is in addition to the aforementioned strain contributions, meaning that the net stretch of a curved flame surface is a function of two components:

$$K = K_s + K_c \ . \tag{3}$$

Here K_s and K_c are the strain and curvature contributions, respectively. Proper representation of the strain term has been given in Eqn. 2, and a similar mathematical form can be given to the curvature term, K_c, yielding:

$$K = \nabla_t \cdot \vec{u} + S_d(\nabla_t \cdot \vec{n}) \tag{4}$$

Equation 4 is a more comprehensive form of Eqn. 1 through which both effects (strain and curvature) are accounted for. Here, the local curvature is denoted by $\nabla_t \cdot \vec{n}$ where $\vec{n}$ is the flame-normal unit vector. Since locally curved flame segments demonstrate different propagation rates, a local displacement speed, S_d, must be employed.

1.2.2 Vortex Pairs to Represent Turbulent Flow

The laminar vortex pair represents a fundamental fluid structure occurring within a turbulent flow (i.e. an eddy). Although the toroid, itself, is laminar, it produces a non-uniform flow similar to that experienced at each individual scale of motion in a turbulent flow. The choice of a counter-rotating vortex pair over a single vortex is based on the following factors:

- A symmetric pair is easily generated and controlled by injection of fluid through a rectangular slot
- A single vortex tends to *roll* along the flame surface without resistance from adjacent fluid movement

- A counter-rotating pair is more-capable of sustaining rotation as it convects due to mutual contributions from each core

Since a single fluid structure is employed, the consideration of multiple turbulence scales is unnecessary. The simplicity, here, lies in the interpretation and analysis of the problem, which can become quite tedious in turbulent combustion.

The use of a 2-D isotropic turbulence field is very common in numerical simulations, but is not feasible for experimental studies for three reasons: (1) taking measurements along a highly-turbulent, stretched flame surface is very difficult, (2) the unpredictable nature of turbulence makes repeatability of the flowfield nearly impossible, and (3) turbulent flowfields involve vortex stretching, which is a 3-D phenomena. The vortex toroid addresses all three of these issues, and simultaneously exposes the relevant physics of stretched flames.

The use of a single fluid structure results in an isolated, observable segment of the flame front that is stretched, thus simplifying data acquisition and observation. At the same time, the conditions by which the toroid is generated can be fixed, and quite easily repeated. However, the most important characteristic of the toroid is that the flowfield can be analyzed in 2-D, based on the axi-symmetry of the vortices. For these reasons, the laminar vortex pair is the simplest way to mimic turbulent flow characteristics while alleviating much of the difficulty that accompanies them.

1.2.3 Influence of Mixture Properties on Stretched Flames

Reactant-stream composition is one of the predominant characteristics influencing stretched flame fronts. This is particularly true for stretched flames with non-zero curvature components. In such cases, a phenomena referred to as *preferential diffusion* can be used to describe the qualitative response of the flame to specific fuel-oxidizer mixtures.

Preferential diffusion simply implies that the relative diffusivities of fuel and oxidizer species are not always in balance with one another. When this occurs, the mass of one species typically has a greater tendency to diffuse throughout the mixture. The "preferred" mode of diffusion for any mixture is that which occurs most easily. Species with lower molecular weights have greater mobility, and usually dictate changes to the local composition.

Hydrocarbon-air mixtures are often used to demonstrate the relative effects of species diffusivity. Hydrocarbon fuels such as methane and propane ($C_3H_8,\ MW \approx 44$) have very similar molecular weights when compared to higher hydrocarbons. However, their diffusive properties are vastly different when considering H/C-air mixtures. The following inequality,

$$MW_{CH_4} \ < \ MW_{Air} \ < \ MW_{C_3H_8}$$

demonstrates that fuel molecules are more diffuse in methane-air mixtures, while in propane-air mixtures, the oxidizer molecules are more diffuse.

In premixed systems, this disproportionality results in stoichiometry variations near the flame. Consider a negatively-curved flame front (concave to the cold reactants) that is subjected to a lean fuel-air mixture. For the case where $MW_{fuel} < MW_{air}$ (e.g. methane-air), the mobile fuel rapidly diffuses outward toward the flame, making the reactant stream increasingly lean ahead of the flame. When $MW_{fuel} < MW_{air}$ (e.g. propane-air) the reactant stream becomes more-stoichiometric ahead of the flame due to outward diffusion of oxygen molecules. Naturally, the inverse is true for each of these two scenarios when the mixture is either fuel-rich, or the flame front is positively-curved (convex to cold reactants).

The implications of preferential diffusion are anything but trivial. Reaction intensity is highly-dependent on stoichiometry, therefore, this phenomena becomes extremely important in lean mixtures where localized quenching is a concern. Mizomoto et al. [13] and Law et al. [14] have studied these effects using negatively-curved bunsen flames with a variety of fuels and stoichiometries. Their findings have provided substantial insight into the causes of localized quenching, and the behavior of different fuel types in highly-curved flames. Lean mixures having sub-unit Lewis numbers (e.g. CH_4/Air) experienced weakened burning at the flame tip, while lean mixtures with Lewis numbers greater than 1 (e.g. C_3H_8/Air) experienced intensified burning. As mentioned before, the opposite was true for rich mixtures. However, in the case of fuel-rich mixtures, the concern is not only flame quenching, but also excessive "dumping" of H/C fuel molecules through the weakened flame tip.

1.3 Previous Studies

Numerous studies have been conducted regarding the two key points of this study. Multi-component fuel mixtures- primarily those containing CH_4, CO, and H_2- have been studied in various configurations to address their respective effects on steady laminar flame characteristics. At the same time, flame-vortex interactions have been widely-used in the study of unsteady laminar flame characteristics.

Extensive work has been performed on both fronts, resulting in an abundance of technical information. A comprehensive review of all relevant experimental and numerical work would be highly impractical, therefore, a handful of studies (representing specific techniques and conclusions) have been selected. Discussion of these studies is provided in the following two sections.

1.3.1 Multicomponent Fuel Mixtures

Several studies have shown that the use of multiple fuel components can be of tremendous value to combustion performance. Early studies by Scholte and Vaags [15] revealed that various fuel mixtures (namely H_2/CO, H_2/CH_4, and CH_4/CO in air) produce a wide variety of unstretched laminar flame speeds, S_L^u.

When the H_2/CO fuel mixture was varied between pure carbon monoxide and pure hydrogen, the laminar flame speed increased by more than 20 times the pure CO/Air value. The trend for CH_4/CO fuel was slightly different. Between pure carbon monoxide and pure methane fuel, there is a peak flame speed value, corresponding to an optimal mixture. At that point, the fuel volume was 10% CH_4 and 90% CO, with a flame speed that was 3.2 times that of the CO/Air flame and 1.9 times that of the CH_4/Air flame.

The data for H_2/CH_4 fuel produced trends that were similar to those for the H_2/CO fuel. Since flame speeds for pure CH_4/Air mixtures are typically greater than pure CO/Air flame speeds, the jump is not as pronounced. However, a 7-fold increase in flame speed between pure methane and pure hydrogen is compelling evidence that multicomponent fuel mixtures can have a profound effect on flame propagation.

Similar studies were later performed by Vagelopoulos and Egolfopoulos [16] using twin

counterflow CO/Air flames with hydrogen and methane as separate fuel additives. These studies were quite conclusive, as they, too, revealed a wide variety of flame behavior for various fuel mixtures. For $CO/H_2/Air$ flames, fuel mole fractions ($\chi_{fuel} = \chi_{CO} + \chi_{H_2}$) of 0.14, 0.17, and 0.20 were used. At higher mole fractions (0.17 and 0.20), the volume of hydrogen present in the mixture had a substantial impact on the unstretched laminar flame speed. Increases in flame speed were as large as 200% (10 cm/s to 30 cm/s) for the addition of 25% hydrogen ($\chi_{CO} = 0.15,\ \chi_{H_2} = 0.05$ for $\chi_{fuel} = 0.20$).

At the lower fuel mole fraction ($\chi_{fuel} = 0.14$), the volume of hydrogen present had only a slight impact on the unstretched laminar flame speed. However, further investigation into the extinction strain rates revealed that between $\chi_{H_2} = 0.016$ and $\chi_{H_2} = 0.044$, extinction strain rates increased from approximately 200/s to 750/s. Similar strain rate observations were made for $CO/CH_4/Air$ flames, although the flame speed trends were comparable to those reported by Scholte and Vaags for such fuel mixtures.

As mentioned in Sec. 1.1, refinement processes often lead to the production of both CO and H_2. However, much more attention is dedicated to the latter of the two, as per the aforementioned conclusions. This is further evident by the vast number of studies centered around hydrogen-enrichment.

Milton and Keck [17] studied the effects of pressure on the burning velocities of stoichiometric H/C-hydrogen-air mixtures, using an experimental combustion bomb. When the flame speed was plotted against the chamber pressure, a double-peak trend was observed in methane-hydrogen and propane-hydrogen fuel mixtures. In both cases, the flame speed experienced a peak shortly after initiation (p = 1atm), followed by a gradual decrease around 2.5 atm, then a rise into a second peak as the chamber pressure approached 5 atm. Neither the acetylene-hydrogen, nor the pure H/C fuel mixtures experienced such behavior when subjected to the same range of pressures. It was concluded that no clear relationship between fuel mixing parameters (H-atom fraction and H/C ratios) and pressure was evident.

Kido et al. [18, 19] have used hydrogen-enriched H/C-air flames to study extinction and flame propagation in spark-ignition (SI) engines. It is typically desirable to use lean H/C fuel mixtures in practical combustion processes, however, there are some acknowledged

concerns in doing so. For instance, in SI engines, performance is often hampered by misfire, which stems from low turbulent flame speeds (S_T) and flame blowout due to excessively lean mixtures. The spherical flame studies by Kido et al. have revealed that the addition of small amounts of hydrogen to lean methane-air and propane-air mixtures generally results in greater turbulent flame speeds for increasing turbulence intensities. They conclude that the low fuel-to-air flammability limit and high flame speed of hydrogen make it a viable option for delaying flame extinction and increasing turbulent flame speed in systems with low pollutant emission requirements.

Similar work toward the influences of hydrogen on flame speed has been performed by Yu et al. [20], and Sher et al. [21]. However, studies such as the aforementioned by Vagelopoulos and Egolfopoulos, reveal that flame speed augmentation is only part of the benefit to hydrogen-enhancement.

In combined experimental/numerical studies, Ren et al. demonstrated that fuel reformation cycles can be used to increase combustion efficiency and simultaneously decrease the emission of carbon oxides (CO and CO_2). The recycling of reformed CH_4 (as CO and H_2) was shown to effectively increase flame extinction strain rates and re-define the operational lean limit of the primary fuel [22]. At the same time, it was determined that the presence of hydrogen accelerated the formation of OH radicals by

$$H + O_2 \rightleftharpoons OH + O,$$

thus increasing the rate of the reactions

$$CH_4 + OH \rightleftharpoons CH_3 + H_2O$$
$$CO + OH \rightleftharpoons CO_2 + H,$$

which contribute to reduction of the CO_2 formation layer which, consequently, reduces CO emission [6]. These reductions are in addition to the consumption of CO_2 product mass

during the reformation process.

In a more-practical examination, Schefer et al. [23] employed hydrogen-enrichment in a lean premixed swirl-stabilized burner. Blowout maps of lean methane-air flames were developed for reactant flow rates between 500 and 1100 slm (litres per minute) and additive hydrogen volume fractions of 0, 12, 22, and 29%. At the greatest flow rate (i.e. strain rate), flames without hydrogen became unstable at T=1600K and blew out around 1540K. For the same flow rate, flames with 29% hydrogen became unstable around 1500K and blew out around 1380K. The ability to operate at lower combustion temperatures also revealed a strong decrease in the emission of carbon monoxide. Measurements of CO and NO_x emissions were taken for pure CH_4 flames and 55/45 CH_4/H_2 flames. While the NO_x formation away from the flame remained approximately the same, the CO formation near and away from the flame was reduced by nearly an order of magnitude in the presence of hydrogen.

It is clear from these studies that the use of multicomponent fuels can substantially benefit combustion performance. The effects on strain rates and propagation velocities have been addressed throughout the preceding studies. The possible translation of these effects to aerodynamically stretched flames is of interest to the current study.

1.3.2 Flame-Vortex Interaction and Unsteady Flame Stretch

As discussed in Sec. 1.2, the flame-vortex interaction is an easy, yet practical, way to analyze stretched flames. Several research groups have taken full advantage of this very concept. However, the analysis of flame-vortex interactions relies heavily on a broader framework of stretched flame fundamentals.

Like many facets of combustion, flame stretch is difficult to observe with sufficient frequency and accuracy. Therefore, it is based largely on theoretical interpretation, rather than experimental correlation. This has given rise to an abundance of numerical studies.

Chen and Echekki have contributed several numerical studies of turbulent stretched flames. Most of their studies have used a laminar premixed flame evolving in a randomly-generated 2-D isotropic turbulence field. This technique effectively produced wrinkled flame

fronts with local strain and curvature variations. In [24], they observed these variations and presented the flame statistics as pdfs (probability density functions) of strain and curvature.

In the randomly-generated turbulence field, the local curvature pdf was centered strongly at zero, meaning that along the flame surface the amount of positive and negative curvature was approximately equal (i.e. mean curvature was zero). The tangential strain rate, however, was not evenly distributed. The mean strain rate was positive (extensive), and the incidents of negative (compressive) strain rates were much less frequent. The observation of a non-zero mean strain and a zero mean curvature is compelling evidence of localized flame stretching, and variable propagation (a.k.a. displacement) speeds.

In collaboration with Gran, Echekki and Chen used their numerical simulations to study negative flame speeds in unsteady premixed flames. A formulation for the displacement speed, S_d, was developed and implemented based on the transport equation for a single mass fraction defining the flame surface. The formulation treated the value of S_d as the sum of three components: flame-tangent (S_d^t), flame-normal (S_d^n), and reactive (S_d^r).

It was shown that contributions due to flame-tangent diffusion decreased linearly with curvature, as did flame-normal contributions under *moderate* curvatures. However, in highly-curved regions, the flame-normal contributions demonstrated the opposite behavior. Contributions due to reaction were much less substantial, and varied only in the vicinity of curvature transition (i.e. negative $\leftrightarrow$ positive). The greatest contributions to negative displacement speeds were observed for the flame-tangent component, in which negative S_d^t values were observed to be as large as $10 \times S_L$.

These findings met opposition from studies by Sinibaldi et al. [11, 25], who reported that, in their experiments, negative displacement speeds were not observed for any degree of stretching. They used flame-vortex interactions to examine displacement speeds and stretch rates along wrinkled flames. Local displacement speeds were defined as the velocity defect between the flame and the incoming reactants (determined from lab coordinates). In H/C-air flames, both positive and negative curvature generally resulted in displacement speeds greater than the unstretched laminar flame speed. However, the values typically remained below $4 \times S_L$ and were reflected in the net stretch rate contributions, where flame

strain was the dominant factor. The lone consensus between numerical and experimental displacement speeds is their remarkable sensitivity to surface curvature.

Experimental flame-vortex interactions were also performed by Roberts et al. [26] to study quenching of lean H/C-air flames. The goal of this study was to isolate the conditions of the flame and the conditions of a single fluid structure to better define the regimes of turbulent combustion. Vortices having the same strength, but ranging in size from 1.0 to 3.1 times the flame thickness, were observed to quench lean methane-air flames (at $\phi = 0.55$) over a variety of strain rates. However, propane-air flames as lean as $\phi = 0.50$ and ethane-air flames as lean as $\phi = 0.56$ did not experience quenching at comparable strain rates.

Additional methane-air data was used to define a single-vortex quenching curve on the turbulent combustion diagram. A similar quenching curve was proposed by Poinsot et al. [27]. Their calculations were based on quenching data provided by simulated flame-vortex interactions under an imposed heat loss term [28]. The particular method used to induce quenching predicted a broader range of turbulence capacities, for which greater u'/S_L values could be achieved at comparable eddy sizes.

The importance of this technique was highlighted by Patnaik and Kailasanath [29], who systematically varied radiative heat losses to induce quenching. A range of burnt gas temperatures (1250K-1400K) were enforced during interactions between lean methane-air flames ($\phi = 0.56$) and vortices representing three different strengths. A radiative quenching limit was observed for each of the vortex strengths, producing a linear relationship between increasing vortex strength and increasing radiative heat loss.

In addition to quenching and unsteady stretch, flame-vortex interactions have been used to study subsequent flowfield effects. Mueller et al. [1] used flame-vortex interactions to study the generation and attenuation of vorticity during unsteady flame stretching. Incident vortices of various strength and size were convected toward laminar premixed propane-air flames. *Weak* vortices were characterized by low u'/S_L and high d_c/δ_F, whereas *strong* vortices were characterized by the exact opposite.

Weak incident vortices were observed to be completely attenuated (dissipated) during interaction with the flame. However, this led to creation of a finite counter-rotating, or

flame-generated, vorticity (denoted FGV). The FGV was shown to be nearly equal to the vorticity of the incident structure. Similar, but less-substantial, observations were made for *intermediate* vortices in which the incident structure was approximately 80% attenuated, and FGV amounted to approximately 8-10% of the incident value.

Strong vortices completely survived the interaction and were observed to locally quench the flame at the leading edge of the structure. No FGV was present, and based on the degree of the initial vorticity, it was not likely to be substantial.

The generation of new vorticity was entirely attributed to baroclinic torque in the vorticity transport equation:

$$\frac{D\vec{\omega}}{Dt} = -\underbrace{\vec{\omega}\left(\nabla\cdot\vec{u}\right)}_{Dilatation} + \underbrace{\left(\nu\nabla^2\vec{\omega}\right)}_{Viscous} + \underbrace{\frac{\nabla\rho\times\nabla p}{\rho^2}}_{Baroclinic} \quad . \tag{5}$$

The misalignment of pressure and density gradients caused the third term on the right-hand side to be non-zero. Hydrostatic pressure gradients (caused by gravity) and hydrodynamic pressure gradients (caused by the low-pressure vortex center) typically led to counter-rotating vorticity just behind the flame [1].

Attenuation of the vorticity was attributed to the first two terms in Eqn. 5. The first term represents dilatation, which- for a fixed mass of fluid- leads to the attenuation of vorticity by gas expansion through the flame. The second term represents attenuation by viscous diffusion. As discussed by Mueller et al., a vortex core that is highly concentrated becomes spatially diffuse due to viscous effects, and consequently has a limited effect on the flame structure. The combined effects of these two terms led to substantial attenuation in *weak* and *intermediate* vortices, while they played an insignificant role in the *strong* vortices.

1.4 Objectives

The goal of this study is to determine if, and how, *syngas* impacts the dynamics of stretched methane-air flames through the use of numerical simulation. Successful completion of this task hinges on several intermediate steps that must be taken in order to highlight the basic physics of the problem, and ensure validity of the simulations. The following objectives

address each of these intermediate steps and provide an appropriate breakdown of the overall goal.

(1) Chemical Mechanism Validation

The first, and most-critical, objective of this study is the selection and validation of a reduced chemical mechanism to describe the finite-rate chemical evolution of the reacting mixture. Such reduced chemical mechanisms employ assumptions regarding individual reaction physics, and effectively eliminate many steps that may not be ultimately significant. The mechanism must be equipped to handle all relevant chemical species in a reliable fashion, while imposing the lowest computational burden possible. GRI-Mech 3.0 [30] is the most-detailed chemical mechanism currently available and is, therefore, used as a reference mechanism.

The Premix [31] and OPPDIF [32] packages in Chemkin-II [33] are a useful combination for testing the reduced chemical mechanism against the full mechanism. In Premix, 1-D simulations of freely-propagating laminar flames are used to study the steady, unstretched flame characteristics in a uniform flow, while in OPPDIF, the characteristics of similar laminar flames are studied under strained (non-uniform flow) conditions. These two packages will be utilized to test the validity of the reduced chemical mechanisim over the desired range of fuel mixtures.

(2) DNS of Laminar Premixed Flames

Following validation of the chemical mechanism, simulations comparable to those performed for steady laminar flames, in Premix, must be sucessfully performed by the DNS code that is to be used for the subsequent flame-vortex simulations. The purpose of this step is to ensure that the code is capable of reproducing a flame that is equivalent to that of an extensively-tested, and widely-accepted software package. During the chemical mechanism validation, specific flame cases will be selected for testing under strained conditions. These same cases will be used for validation of the DNS code.

A 1-to-1 comparison of flow variables, and chemical source terms will be performed on the Premix and DNS solutions. In doing so, the flow solver and chemistry solver can be tested simultaneously for consistency and robustness. The Premix solution is computed at

an assumed steady state, while the DNS solution is dynamic and may require relaxation time, based on the accuracy of the initialization. When this is the case, the code must be taken to an *observed* steady state before a valid comparison can be made.

(3) Simulation of Laminar Flame-Vortex Interaction

Once the DNS code is capable of reproducing laminar premixed flames, it must demonstrate the ability to reproduce realistic flame-vortex interactions. As will be discussed in the following chapters, several underlying assumptions are made during the mathematical and computational formulation of the problem. This means that the code is not likely to fully replicate every detail of an experimental flame-vortex interaction. However, the qualitative characteristics should be within the limits of explanation, and some comparable quantitative trends should exist.

Flame and vortex parameters will be adapted from published experimental data, and applied in the DNS. Multiple simulations will then be performed using different vortex configurations on a fixed-property methane-air flame. These simulations will be treated as the control cases for the subsequent simulations.

(4) Simulation of Flame Stretch for Two-Component Fuels

After the methane-air flame-vortex interactions have been successfully performed, the remaining computational work is rather passive. The flame-vortex simulations must then be performed using the selected two-component fuel cases (from Objective 1), in order to observe the effects of those mixtures on stretched flames. At that point, the flame parameters and vortex configurations will already be defined, thus simplifying the process.

After the required simulations have been completed, a qualitative and quantitative analysis will be performed on all of the cases. Analogous cases will then be compared, and conclusions will be made regarding their respective similarities, and differences. Theoretical interpretations will then be provided to tie the conclusions together as well as provide some possible extensions to future applications.

CHAPTER II

PHYSIO-MATHEMATICAL FORMULATION

A Direct Numerical Simulation has been selected as the most-fitting technique to study the problem at hand. The physics of this particular problem are governed primarily by partial differential equations that require solution by iterative methods. The DNS performs numerical integration of the exact, unfiltered equations of motion in space and time, in addition to temporal integration of chemical source terms (hence the name, *direct numerical simulation*). This chapter covers the physical relationships and associated mathematics that are used to simulate the flame-vortex interactions in this study.

2.1 Governing Equations

The DNS solves the compressible, reacting, multi-species Navier-Stokes equations for mass, momentum, and energy, with species conservation. The respective mathematical forms are shown here, in index form:

$$\frac{\partial \rho}{\partial t} = -\frac{\partial \rho u_i}{\partial x_i} \tag{6}$$

$$\frac{\partial}{\partial t}\rho u_i = -\frac{\partial}{\partial x_j}\left[\rho u_i u_j + p\delta_{ij} - \tau_{ij}\right] \tag{7}$$

$$\frac{\partial \rho E}{\partial t} = -\frac{\partial}{\partial x_i}\left[(\rho E + p)u_i + q_i - u_j \tau_{ji}\right] \tag{8}$$

$$\frac{\partial \rho Y_k}{\partial t} = -\frac{\partial}{\partial x_i}\left[\rho(u_i + \sum_{k=1}^{N_s} D_k \frac{\partial Y_k}{\partial x_i})Y_k\right] + \dot{w}_k \tag{9}$$

where ρ is the fluid density, u_i is the fluid velocity vector, p is the static pressure, τ_{ji} is the viscous (shear) stress tensor, E is the total energy, and q_i is the heat flux vector. The terms Y_k, D_k, and $\dot{w}_k$ represent the mass fraction, species diffusion coefficient, and chemical source term of the kth species, respectively.

At relatively low temperatures and atmospheric pressures, the gas properties (density, pressure, and temperature) can be related by the ideal gas law,

$$p = \rho \bar{R} T \ . \tag{10}$$

Here T is the gas temperature, and $\bar{R}$ is the mixture specific gas constant, computed from the universal gas constant, R, and the mixture molecular weight, MW_{mix}, by

$$\bar{R} = \frac{R}{MW_{mix}} = \frac{R}{\sum_{k=1}^{N_s} Y_k MW_k} \ . \tag{11}$$

The energy equation contains several terms that are given in general form. A useful relationship between the total energy, heat flux, and shear stress does not exist, therefore, they must be individually examined. The total energy, E, is broken into two components, as shown by

$$E = e_i + \frac{1}{2} u_k^2 \ . \tag{12}$$

The first term, e_i, is the internal (thermo-chemical) component, and the second, $u_k^2/2$, is the kinetic component. Due to the broad range of temperatures experienced during combustion, it is safe to assume that the calorically-perfect gas assumption (of constant specific heats) is not valid. A thermally-perfect gas (TPG) formulation is applied, making each specific heat value a function of the local temperature. The internal energy can be rewritten as

$$e_i = \int_{T_0}^{T} C_v \ dT \ , \tag{13}$$

where T_0 is a reference temperature, and C_v is the constant-volume specific heat. The specific heat value is determined on a mixture basis using

$$C_v = \left(\sum_{k=1}^{n} C_{p,k} Y_k \right) - \bar{R} \ , \tag{14}$$

in which $C_{p,k}$ is the constant-pressure specific heat of the kth species, computed from polynomial curvefit data, and temperature.

The shear stress, τ_{ji}, can be expanded to

$$\tau_{ji} = \mu \left[\left(\frac{\partial u_j}{\partial x_i} + \frac{\partial u_i}{\partial x_j} \right) - \frac{2}{3} \frac{\partial u_k}{\partial x_k} \delta_{ji} \right] \ , \tag{15}$$

which demonstrates the fact that the gas mixture behaves as a Newtonian fluid, for which shear stress is a linear function of the strain rate [34]. The proportionality constant, μ, represents the molecular viscosity, and δ_{ji} is the Kronecker delta function (1 for $i = j$, and 0 for $i \neq j$). The molecular viscosity is highly temperature-dependent, and is often approximated using Sutherland's Law ($\mu = f(T)$). However, the importance of molecular transport in this study warrants the use of a more precise model (to be described in the next section), for which viscosity is not a single function of temperature.

The heat flux vector, q_i, is composed of terms related to thermal conduction and enthalpy diffusion. The system is assumed to be adiabatic, with negligible radiative heat losses, and negligible heat flux related to Dufour effects (thermal transport resulting from species concentration gradients). Based on these assumptions, the heat flux can be shown as

$$q_i = -\kappa \frac{\partial T}{\partial x_i} + \rho \sum_{k=1}^{n} h_k D_k \frac{\partial Y_k}{\partial x_i} \ . \tag{16}$$

The first term represents Fourier's Law of conduction, in which the temperature gradient, $\partial T / \partial x_i$, induces a heat flux on the order of κ, the thermal conductivity of the mixture. The second term describes the heat flux related to enthalpy diffusion. The species enthalpy, h_k, is given by the more useful form

$$h_k = h_{f,k}^0 + \int_{T_0}^{T} C_{p,k}\, T dT \tag{17}$$

where $h_{f,k}^0$ is the heat of formation at reference temperature T_0.

2.1.1 Chemical Source Terms

The preceding relationships are all based on the fact that energy is neither created, nor destroyed in a closed system. According to Eqns. 6 and 9, the same is true for mass. In the species equation (9), the movement of mass between chemical species is balanced by the chemical source terms, $\dot{w}_k$. Each chemical source term represents the time-rate-of-change of that particular species' concentration, as shown by

$$\dot{w}_k = \frac{d[k]}{dt} = \frac{d}{dt}\rho Y_k \ . \tag{18}$$

Unlike terms in the energy equation, the individual chemical source terms are not computed using strictly-independent forms. Instead, they collectively make up a set of linear ODEs (ordinary differential equations) that must be solved simultaneously. Similarly, the individual ODEs do not have a general assigned form, as they depend on the specific set of reactions under consideration. For example, species A may be represented in two reversible reaction steps, such as

$$(1) \quad A + B \ \rightleftharpoons \ C + D$$

$$(2) \quad E + F \ \rightleftharpoons \ A + G \ .$$

Species A will then have four contributions to its chemical source term: 2 formation and 2 consumption. In reaction step (1), A is consumed by B during the *forward* reaction (left to right), but it is also formed during the *reverse* reaction (right to left) by C and D. Similar forward and reverse reactions exist for step (2).

By convention, the rates of consumption and formation are opposite in sign, but are not necessarily equal in magnitude. Each forward and reverse reaction has an associated chemical rate that can be described by an Arrhenius expression of the form

$$\theta = \psi e^{-E_A/RT}, \tag{19}$$

where θ is the chemical rate, ψ is an empirical constant, E_A is the activation energy of the reaction, R is the universal gas constant, and T is the temperature. In the two reversible reaction steps given above, values $\theta_{f,1}$ and $\theta_{r,1}$ can be used to represent the forward and reverse rates for reaction step (1). Similarly, $\theta_{f,2}$ and $\theta_{r,2}$ can be used to represent the forward and reverse rates for step (2).

Determination of the chemical source term for species A is then nothing more than an application of these rates to the respective species concentrations. In full form, $\dot{w}_A$ can be written as

$$\dot{w}_A = \frac{d[A]}{dt} = -\theta_{f,1}[A][B] + \theta_{r,1}[C][D] + \theta_{f,2}[E][F] - \theta_{r,2}[A][G], \tag{20}$$

in which $[A], ..., [G]$ represent the species concentrations. An expression like this exists for all N_s species in the system. However, from Eqn. 19 it is known that the chemical rates, θ, are also nonlinear functions of temperature. Therefore, it can be concluded that the chemical evolution of N_s species is described by a set of N_s coupled, first-order ODEs of the form $\dot{w}_k = f([1], ..., [N], T)$.

In simulating lean H/C-air flames, it is useful to employ a diluent formulation which takes advantage of the fact that there is often an abundant, and essentially inert n^{th} species. Air is approximately 79% nitrogen (N_2), by volume, therefore, in lean H/C-air flames it makes up a substantial portion of the system's mass. In terms of reactivity, N_2 primarily contributes to slower reaction mechanisms (such as NO_x formation) that yield relatively low concentrations.

This is considerably important to the numerical solution of N_s ODEs. The chemical rates, θ, often vary by orders of magnitude, making the ODE set particularly *stiff*, and more difficult to solve [35]. If the n^{th} species is effectively passive, then the dimension of the set can be reduced to $N_s - 1$ by using $\dot{w}_n = 0$ and the mass closure

$$Y_n = 1 - \sum_{k=1}^{n-1} Y_k - \sum_{k=n+1}^{N_s} Y_k \ . \tag{21}$$

Here, the chemical source term of the n^{th} species is assumed to be zero, and once the $N_s - 1$ ODEs have evolved some Δt, the leftover mass is absorbed by the n^{th} species.

2.1.2 Heat and Mass Transport

In an attempt to preserve physical accuracy, multicomponent formulations for heat and mass transport properties are employed. This technique is designed to address the variable nature of scalar transport values when considering several chemical species and an undetermined range of thermo-chemical states. In many cases, these variations are regarded to be negligible. However, in dealing with the combination of stretched flames and multicomponent fuels, the transport plays a vital role in determining flame behavior.

In many studies, such as those by Chen et al. [36, 37], fixed dimensionless parameters, like Schmidt (Sc), Prandtl (Pr), and Lewis (Le) numbers, are used to account for the relative magnitudes of transport properties. More specifically, these values provide fixed relationships between kinematic visosity, ν, species diffusivity, D_k, and thermal conductivity, κ, all of which exist in the preceding governing equations. The dimensionless transport properties are related to one another by

$$Sc = LePr \iff \left(\frac{\nu}{D_{k/mix}}\right) = \left(\frac{\alpha}{D_{k/mix}}\right)\left(\frac{\nu}{\alpha}\right) \tag{22}$$

where values for viscosity and thermal diffusivity (α) are usually mixture-averaged, and species diffusion coefficients are either mixture-averaged (D_{mix}) or individually-defined (D_k). (The latter is achieved by specifying Sc or Le values for each species.)

In the multicomponent formulation, values for dynamic viscosity ($\mu = \rho\nu$) species diffusivity, and thermal conductivity are individually-computed with regard to all chemical species. As revealed in the previous section, these values are of importance to the viscous stress tensor, the species flux vector, and the heat flux vector, respectively.

Temperature-dependent, pure-species transport properties are computed from third-order (S=4) polynomial curvefit data in the following fashion:

$$ln\ \mu_k = \sum_{n=1}^{S} a_{n,k}(ln\ T)^{n-1} \tag{23}$$

$$ln\ \kappa_k = \sum_{n=1}^{S} b_{n,k}(ln\ T)^{n-1} \tag{24}$$

$$ln\ D_{jk} = \sum_{n=1}^{S} d_{n,jk}(ln\ T)^{n-1}. \tag{25}$$

Here, D_{jk} represents the binary diffusion coefficient pairs (for species j into each species k), and $a_{n,k}$, $b_{n,k}$, and $d_{n,jk}$ are the respective curvefit coefficients [38]. Viscosity (Eqn. 24) and thermal conductivity (Eqn. 25) are both independent of pressure, and are averaged over the mixture according to

$$\bar{\mu} = \sum_{k=1}^{N} \chi_k \mu_k \tag{26}$$

$$\bar{\kappa} = \sum_{k=1}^{N} \chi_k \kappa_k, \tag{27}$$

where χ_k is the molar fraction of the kth species. However, more attention is given to the treatment of multicomponent diffusion coefficients.

The binary diffusion coefficients computed from Eqn. 25 are represented in the following matrix, M,

$$M_{ij} = \frac{16T}{25p} \sum_{k=1}^{N} \frac{\chi_k}{m_i D_{ik}} \left[m_j \chi_j (1 - \delta_{ik}) - m_i \chi_j (\delta_{ij} - \delta jk) \right] \tag{28}$$

as given by Dixon-Lewis [39]. Here, m_i is the molecular mass of species i, D_{ik} are the binary diffusion coefficients, and the δ values represent very small offset constants for the binary diffusion coefficients that provide mathematical continuity in the limit of a pure species [40]. The multicomponent diffusion coefficients are then determined from Eqn. 28 by

$$D_{ij} = \chi_i \frac{16T}{25p} \frac{\bar{m}}{m_j} (P_{ij} - P_{ii}) \tag{29}$$

where P is the inverse of matrix M ($P = M^{-1}$) and $\bar{m}$ is the average molecular mass of the mixture.

CHAPTER III

COMPUTATIONAL TECHNIQUE

In the preceding chapter, the representative DNS equations for fluid dynamics and chemistry were presented. This chapter outlines the numerical technique that is used to solve those governing equations. A breakdown of the equations into numerical form is presented, and extended to a computational grid which provides a discretized representation of the flowfield. A set of boundary conditions are discussed for closure of the numerical scheme, and further discussion into problem initialization is provided. Although the current study is fundamentally 2-D, the technique is formulated and presented in 3-D, with subsequent discussion of its extension to 2-D problems.

3.1 Numerical Integration Scheme

To solve the conservation equations of the DNS, a technique that combines a finite-volume spatial scheme with an explicit time-integration scheme is employed. These spatial and temporal schemes have been widely-tested in previous studies, and offer the benefits of simple implementation and reliable stability.

3.1.1 Finite-Volume Scheme

The fundamental conservation equations used in DNS can be represented by a single, general form which is written as

$$\frac{\partial \mathbf{Q}}{\partial t} + \nabla \cdot \mathbf{F} = \mathbf{\Phi} \ . \tag{30}$$

In this simplified form, the conserved variables are represented by a state vector, $\mathbf{Q}$. The time-rate-of-change of the state vector, $\mathbf{Q}$, is controlled by elements of its flux vector, $\mathbf{F}$, and its source vector, $\mathbf{\Phi}$. When expanded to 3-D, the compact forms of these vectors contain

several terms, as shown here:

$$\mathbf{Q} = (\rho,\ \rho u,\ \rho v,\ \rho w,\ E,\ \rho Y_k)^T \tag{31}$$

$$\mathbf{\Phi} = (0,\ 0,\ 0,\ 0,\ 0,\ \dot{w}_k)^T \tag{32}$$

$$\mathbf{F} = (\mathbf{F_x},\ \mathbf{F_y},\ \mathbf{F_z})\ . \tag{33}$$

Spatial integration of Eqn. 30 over a finite, constant volume, V, produces a new equation of the form:

$$\frac{\partial}{\partial t}\int_V \mathbf{Q}\ dV + \int_V \nabla\cdot\mathbf{F}\ dV = \int_V \mathbf{\Phi}\ dV\ . \tag{34}$$

The second term in Eqn. 34 can take advantage of the Gaussian divergence theorem to integrate elements of the flux vector, $\mathbf{F}$, over their respective surface elements in vector $d\mathbf{S}$=($d\mathbf{S_x}$, $d\mathbf{S_y}$, $d\mathbf{S_z}$) [41]. In doing so, the second term becomes

$$\int_V \nabla\cdot\mathbf{F}\ dV = \oint_S \mathbf{F}\cdot d\mathbf{S}\ . \tag{35}$$

The elements of d$\mathbf{S}$ make up the boundary of the control volume and are defined by surface-normal components that are directed outward from the volume interior.

The nature of the laminar flame problem facilitates the use of a uniform, hexagonal computational grid. Given in integral form, Eqn. 34 can be applied to virtually any volume imaginable [41]. However, the uniform grid provides the lowest likelihood of error and can take advantage of the exact 3-D Cartesian vector components. Moreover, the use of a uniform grid obviates the need for spatial transformations and further information storage. When extended to a constant-volume, hexagonal grid, Eqn. 34 can be represented by

$$\frac{\partial\mathbf{Q}}{\partial t} + \frac{1}{V}(\mathbf{F_x}\,d\mathbf{S_x} + \mathbf{F_y}\,d\mathbf{S_y} + \mathbf{F_z}\,d\mathbf{S_z}) = \mathbf{\Phi}\ . \tag{36}$$

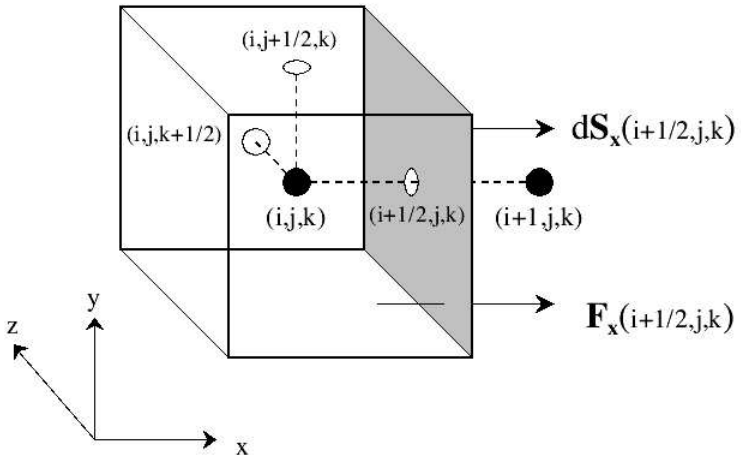

Figure 1: Conceptual diagram of the finite-volume cell showing two cell-center points with flux and surface vectors acting on the shaded cell face.

Each of the flux vector elements can then be broken into its inviscid (Euler) and viscous components as shown by the following set of equations:

$$\mathbf{F_x} = \begin{pmatrix} \rho u \\ \rho u u + p \\ \rho u v \\ \rho u w \\ u(\rho E + p) \\ \rho u Y_k \end{pmatrix} - \begin{pmatrix} 0 \\ \tau_{xx} \\ \tau_{xy} \\ \tau_{xz} \\ u\tau_{xx} + v\tau_{xy} + w\tau_{xz} - q_x \\ \rho D_k \frac{\partial Y_k}{\partial x} \end{pmatrix} \tag{37a}$$

$$\mathbf{F_y} = \begin{pmatrix} \rho v \\ \rho v u \\ \rho v v + p \\ \rho v w \\ v(\rho E + p) \\ \rho v Y_k \end{pmatrix} - \begin{pmatrix} 0 \\ \tau_{yx} \\ \tau_{yy} \\ \tau_{yz} \\ u\tau_{yx} + v\tau_{yy} + w\tau_{yz} - q_y \\ \rho D_k \frac{\partial Y_k}{\partial y} \end{pmatrix} \tag{37b}$$

$$\mathbf{F_z} = \underbrace{\begin{pmatrix} \rho w \\ \rho w u \\ \rho w v \\ \rho w w + p \\ w(\rho E + p) \\ \rho w Y_k \end{pmatrix}}_{\textbf{Euler Flux}} - \underbrace{\begin{pmatrix} 0 \\ \tau_{zx} \\ \tau_{zy} \\ \tau_{zz} \\ u\tau_{zx} + v\tau_{zy} + w\tau_{zz} - q_z \\ \rho D_k \frac{\partial Y_k}{\partial z} \end{pmatrix}}_{\textbf{Viscous Flux}} \tag{37c}$$

When applying the finite-volume scheme in 2-D, the third-dimension fluxes are simply turned off (i.e. $\mathbf{F_z} = 0$). Similarly, all third-dimension vector components (e.g. $f(w)$, τ_{xz}, τ_{yz}) must be set to zero since fluid motion is neglected in that particular direction. While some directional values are not computed, specification of finite cell volumes is still required for state varibles and volumetric source terms. Therefore, the 3-D finite-volume formulation is still applied in 2-D computations.

3.1.2 Explicit Time-Integration Scheme

Numerical integration of Eqn. 36 is performed using a modified form of MacCormack's explicit predictor-corrector scheme [42], that is second-order accurate in time and fourth-order accurate in space (on uniform grids). In this technique, the state vector time-derivative is reduced to a finite-difference expression which is then split into two stages (referred to as the *predictor* and the *corrector* [41]). In these two stages, Eqn. 36 can be re-written- in terms of the time-derivative of $\mathbf{Q}$- as

$$\begin{aligned} \mathbf{Q}^{(\star)} &= \mathbf{Q}^{(n)} + \mathrm{d}\mathbf{Q}^{(n)} && (Predictor) \\ \mathbf{Q}^{(n+1)} &= \tfrac{1}{2}\left[\mathbf{Q}^{(n)} + \mathbf{Q}^{(\star)} + \mathrm{d}\mathbf{Q}^{(\star)}\right] && (Corrector), \end{aligned} \tag{38}$$

where (n) represents the discrete time level, $(\star)$ represents values at the *predictor* time level, and $(n+1)$ represents values at the *corrector* time level.

The $\mathrm{d}Q$ terms represent the combined (residual) contribution from the respective flux $\mathbf{F}$ and source $\mathbf{\Phi}$ vectors. These residual terms are of the form

$$
\begin{aligned}
d\mathbf{Q}^{(n)} &= -\Delta t \left[\frac{1}{V} \left(\Delta \mathbf{F}_x^{+(n)} d\mathbf{S_x} + \Delta \mathbf{F}_y^{+(n)} d\mathbf{S_y} + \Delta \mathbf{F}_z^{+(n)} d\mathbf{S_z} \right) - \mathbf{\Phi^{(n)}} \right] \\
d\mathbf{Q}^{(*)} &= -\tfrac{1}{2} \Delta t \left[\frac{1}{V} \left(\Delta \mathbf{F}_x^{-(*)} d\mathbf{S_x} + \Delta \mathbf{F}_y^{-(*)} d\mathbf{S_y} + \Delta \mathbf{F}_z^{-(*)} d\mathbf{S_z} \right) - \mathbf{\Phi}^{(*)} \right]
\end{aligned}
\tag{39}
$$

where $\Delta\mathbf{F}$ is the flux differential between sequential parallel faces, given as

$$
\begin{aligned}
\Delta \mathbf{F_x} &= \mathbf{F_x}_{(i+1/2,j,k)} - \mathbf{F_x}_{(i-1/2,j,k)} \\
\Delta \mathbf{F_y} &= \mathbf{F_y}_{(i,j+1/2,k)} - \mathbf{F_y}_{(i,j-1/2,k)} \\
\Delta \mathbf{F_z} &= \mathbf{F_z}_{(i,j,k+1/2)} - \mathbf{F_z}_{(i,j,k-1/2)}
\end{aligned}
\tag{40}
$$

The (+) and (-) superscripts in Eqn. 39 respectively denote forward and backward differencing. By convention, the finite-volume scheme stores known information at the cell center, which is specified by some (i, j, k) location. Fluxes are then projected onto the cell faces, which are located halfway between adjacent cell centers (on uniform grids). Since there is no information supplied at midpoint locations, finite-differencing must be used to extrapolate flux information from the neighboring cell centers, orthogonal to that cell face [43].

The second-order accurate differencing, used in the orignial MacCormack scheme, is achieved through an alternating sequence of the following flux values:

$$
\begin{array}{cccc}
\overbrace{\qquad\qquad\qquad\qquad}^{\textbf{Forward}} & & & \overbrace{\qquad\qquad\qquad\qquad}^{\textbf{Backward}} \\
\mathbf{F^+_x}_{(i+1/2,j,k)} = \mathbf{F_x}_{(i+1,j,k)} & & & \mathbf{F^-_x}_{(i+1/2,j,k)} = \mathbf{F_x}_{(i-1,j,k)} \\
\mathbf{F^+_y}_{(i,j+1/2,k)} = \mathbf{F_y}_{(i,j+1,k)} & \quad and \quad & & \mathbf{F^-_y}_{(i,j+1/2,k)} = \mathbf{F_y}_{(i,j-1,k)} \\
\mathbf{F^+_z}_{(i,j,k+1/2)} = \mathbf{F_z}_{(i,j,k+1)} & & & \mathbf{F^-_z}_{(i,j,k+1/2)} = \mathbf{F_z}_{(i,j,k-1)}
\end{array}
\tag{41}
$$

The purpose of alternating between forward and backward differencing is to prevent the introduction of a directional bias [43]. However, second-order spatial accuracy is not always sufficient for DNS. In response to this, Nelson [44] has proposed a modified "2-4" MacCormack scheme that improves the extrapolation of flux values to cell faces, yielding fourth-order spatial accuracy.

The modified "2-4" MacCormack scheme uses information from four different cells to perform the forward and backward differencing. Information from the $(i-1)$, (i), $(i+1)$, and $(i+2)$ cell centers is supplied to the $(i+1/2)$ cell face in the following fashion:

$$\begin{aligned} \mathbf{F}^{+}_{\mathbf{x}\,(i+1/2,j,k)} &= \tfrac{1}{6}\left(2\mathbf{F}_{\mathbf{x}(i,j,k)} + 5\mathbf{F}_{\mathbf{x}(i+1,j,k)} - \mathbf{F}_{\mathbf{x}(i+2,j,k)}\right) \quad (Forward) \\ \mathbf{F}^{-}_{\mathbf{x}\,(i+1/2,j,k)} &= \tfrac{1}{6}\left(2\mathbf{F}_{\mathbf{x}(i+1,j,k)} + 5\mathbf{F}_{\mathbf{x}(i,j,k)} - \mathbf{F}_{\mathbf{x}(i-1,j,k)}\right) \quad (Backward) \end{aligned} \tag{42}$$

Similar formulations are used for extrapolation to the $(j+1/2)$ and $(k+1/2)$ cell faces, but are omitted for brevity.

3.2 Boundary Conditions

The boundary conditions of the DNS are adapted from the thermally-perfect, multi-species, reactive Navier-Stokes Characteristic Boundary Conditions (NSCBC), proposed by Baum et al. [45]. All four of the domain boundaries are referred to as *free* boundaries, meaning that they are fluid, not solid [41]. The reactant stream enters the domain through a fixed-pressure/fixed-velocity, subsonic inflow boundary, and the product stream exits through a partially-reflective, subsonic outflow boundary. Periodic conditions are applied at the upper and lower (streamwise) boundaries which preserves the symmetry of the flowfield when the counter-rotating vortex pair is properly-centered.

Selection of the NSCBC at the inflow and outflow boundaries is based, strictly, on the nature of the problem. The combined effects of fluid dynamics and chemistry are far too complex to employ generic, simplified boundary conditions and still obtain a well-posed problem. The selection of periodic streamwise boundaries stems from preliminary tests with simplified flame-vortex simulations.

Typically, in flame-vortex simulations, a slip wall boundary is employed at the center of the flowfield to induce symmetry and, consequently, reduce the computation by 50%. Unfortunately, physical and mathematical interpretations of the problem mandate implementation of a slip wall at both streamwise boundaries. This combination has demonstrated an uncontrolled reflection of acoustic waves in the transverse direction, ultimately destroying the vortex.

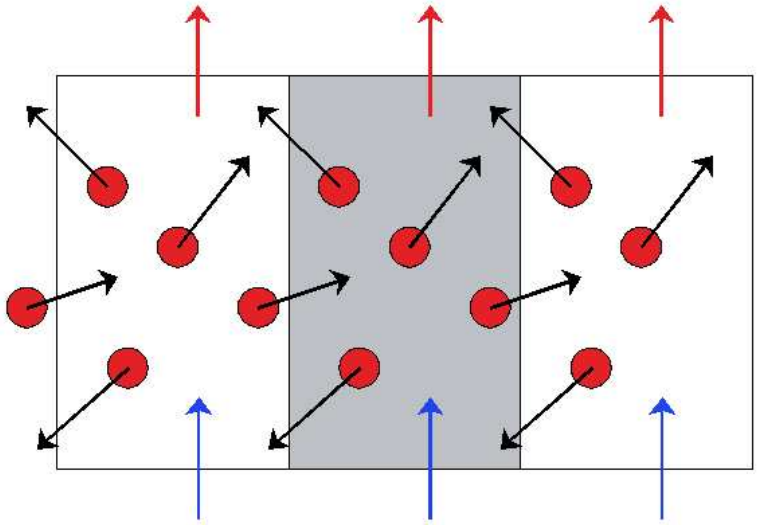

Figure 2: Conceptual figure of periodic boundary conditions applied at the vertical walls. The shaded region represents the computational domain, and the adjacent regions represent its infinite replicas.

3.2.1 Periodic Boundary Conditions

Periodicity is realized in the direction perpendicular to the incoming reactant stream. This is most-effectively described as an infinite repetition of the flowfield in the assigned direction of periodicity. It assumes that exact replicas of the 2-D flowfield are located adjacent to the periodic boundaries, thus enforcing the fundamental conservation principles of the system. Any mass that enters or exits the domain through a periodic boundary is assumed to enter or exit through its respective periodic counterpart. Figure 2 illustrates the basic concept of periodic boundary conditions.

When correctly implemented, the streamwise periodic boundaries enforce symmetry of the non-uniform flowfield. The dimensions of the domain, as well as the vortex, are chosen such that the flame experiences nearly-uniform, free-stream conditions near the streamwise boundaries. However, any fluid that happens to enter or exit the domain will be countered at the opposite boundary. This also alleviates excessive reflection of acoustic waves that are characteristic of the perfectly-reflecting wall boundaries.

3.2.2 Characteristic Boundary Conditions

Acoustic wave propagation is a consistent feature of unsteady combustion simulations, based on compressibility requirements. In a truly-physical sense, the free boundaries being used in these simulations allow for the passage of acoustic waves without any amplification or diminishment of the disturbance. Therefore, the analogous computational boundaries should be capable of the same thing. The thermally-perfect, multi-species NSCBC use a characteristic wave analysis to facilitate this for reacting flows.

The concept of characteristic wave analysis is fairly simple. For inviscid (Euler) equations of motion, it has been shown that terms in the streamwise, x_i-direction can be represented by characteristic waves propagating in that same direction [46]. Such boundary conditions are referred to as the Euler Characteristic Boundary Conditions (ECBC). The ECBC have been extended to viscous (Navier-Stokes) equations of motion through the original NSCBC [47]. While the original NSCBC allow for characteristic wave analysis of many practical flows, they are somewhat limited by the assumption of a perfect gas with constant, homogeneous thermodynamic properties. This effectively restricts the former NSCBC to non-reacting systems for which changes in heat capacity and composition at the boundaries are negligible [45]. The multi-species, reacting NSCBC are designed to address this issue.

As noted by Baum et al., centered schemes- similar to that used in the current DNS- typically provide very little numerical dampening which can cause numerical wave formation in the presence of high-wave-number instabilities. They further note that these numerical waves are purely non-physical and they may experience propagation velocities that oppose those of the physical characteristic velocities. In such a case, reflection of numerical waves from the boundaries can result in disturbance of the existing physical waves, or generation of new physical waves.

Extensive analysis has been performed by Baum et al. [45], Thompson [46], and Poinsot et al. [47] to address the formation and propagation of numerical waves. The cumulative result of these studies is the following set of conservation equations:

$$
\begin{aligned}
\tfrac{\partial \rho}{\partial t} + \tfrac{\rho \bar{C}_p}{c^2}\left(\mathscr{L}_1 + \mathscr{L}_{N_s+5}\right) + \mathscr{L}_{N_s+4} + \mathscr{B}_1 &= 0 \\
\tfrac{\partial E}{\partial t} + \left(\tfrac{u^2+v^2+w^2}{2} + \sum_{k=1}^{N_s} h_k Y_k\right)\left(\tfrac{\rho \bar{C}_p}{c^2}\left(\mathscr{L}_1 + \mathscr{L}_{N_s+5}\right) + \mathscr{L}_{N_s+4}\right) &+ \\
\rho u \tfrac{\bar{C}_p}{c}\left(\mathscr{L}_{N_s+5} - \mathscr{L}_1\right) + \rho v \mathscr{L}_2 + \rho w \mathscr{L}_3 + \rho \sum_{k=1}^{N_s}\left[\left(\bar{C}_p - \tfrac{h_k W_k}{WT}\right)\mathscr{L}_{k+3}\right] &- \\
\tfrac{h_1 W_1}{W}\,\mathscr{L}_{N_s+4} + \mathscr{B}_2 &= 0 \\
\tfrac{\partial(\rho u)}{\partial t} + \tfrac{\rho \bar{C}_p}{c^2}\left[(u-c)\,\mathscr{L}_1 + (u+c)\,\mathscr{L}_{N_s+5}\right] + u\mathscr{L}_{N_s+4} + \mathscr{B}_3 &= 0 \\
\tfrac{\partial(\rho v)}{\partial t} + \tfrac{\rho v \bar{C}_p}{c^2}\left(\mathscr{L}_1 + \mathscr{L}_{N_s+5}\right) + \rho\mathscr{L}_2 + v\mathscr{L}_{N_s+4} + \mathscr{B}_4 &= 0 \\
\tfrac{\partial(\rho w)}{\partial t} + \tfrac{\rho w \bar{C}_p}{c^2}\left(\mathscr{L}_1 + \mathscr{L}_{N_s+5}\right) + \rho\mathscr{L}_3 + w\mathscr{L}_{N_s+4} + \mathscr{B}_5 &= 0 \\
\tfrac{\partial(\rho Y_1)}{\partial t} + \tfrac{\rho Y_1 \bar{C}_p}{c^2}\left(\mathscr{L}_1 + \mathscr{L}_{N_s+5}\right) - \tfrac{W_1}{W}\tfrac{\rho}{T}\mathscr{L}_3 + \left(Y_1 - \tfrac{W_1}{W}\right)\mathscr{L}_{N_s+4} + \mathscr{B}_6 &= 0 \\
\tfrac{\partial(\rho Y_j)}{\partial t} + \tfrac{\rho Y_j \bar{C}_p}{c^2}\left(\mathscr{L}_1 + \mathscr{L}_{N_s+5}\right) - \tfrac{W_j}{W}\tfrac{\rho}{T}\mathscr{L}_{j+3} + Y_j\mathscr{L}_{N_s+4} + \mathscr{B}_{j+5} &= 0
\end{aligned}
\tag{43}
$$

In this equation set, the $\mathscr{L}_i$'s represent variations of incoming and outgoing wave amplitudes, where $j = 2, .., N_s$. The $\mathscr{B}_i$'s represent all additional terms in the Navier-Stokes equations (viscous, diffusive, and reactive) that do not have first derivatives of primitive variables (ρ, T, u, v, w Y_1, ..., Y_{N_s}) in the streamwise (x) direction. The wave amplitude variations can be expressed by

$$
\mathscr{L}_i = \lambda_i \begin{pmatrix}
\left(\frac{1}{2}\frac{(\gamma-1)T}{\gamma\rho}\right)\frac{\partial \rho}{\partial x} + \left(\frac{1}{2}\frac{\gamma-1}{\gamma}\right)\frac{\partial T}{\partial x} - \left(\frac{1}{2}\frac{c}{\bar{C}_p}\right)\frac{\partial u}{\partial x} + \sum_{k=1}^{N_s}\left(\frac{1}{2}\frac{(\gamma-1)\bar{W}T}{\gamma W_k}\right)\frac{\partial Y_k}{\partial x} \\
\frac{\partial v}{\partial x} \\
\frac{\partial w}{\partial x} \\
\left(\frac{(1-\gamma)T}{\gamma\rho}\right)\frac{\partial \rho}{\partial x} + \left(\frac{1}{\gamma}\right)\frac{\partial T}{\partial x} - \left(\frac{\bar{W}T}{W_1}\right)\frac{\partial Y_1}{\partial x} + \sum_{k=1}^{N_s}\left(\frac{\bar{W}T}{\gamma W_k}\right)\frac{\partial Y_k}{\partial x} \\
- \left(\frac{\bar{W}T}{W_j}\right)\frac{\partial Y_j}{\partial x} \\
\left(\frac{\gamma-1}{\gamma}\right)\frac{\partial \rho}{\partial x} - \left(\frac{\rho}{\gamma T}\right)\frac{\partial T}{\partial x} - \sum_{k=1}^{N_s}\left(\frac{\bar{W}\rho}{W_i\gamma}\right)\frac{\partial Y_k}{\partial x} \\
\left(\frac{1}{2}\frac{(\gamma-1)T}{\gamma\rho}\right)\frac{\partial \rho}{\partial x} + \left(\frac{1}{2}\frac{\gamma-1}{\gamma}\right)\frac{\partial T}{\partial x} + \left(\frac{1}{2}\frac{c}{\bar{C}_p}\right)\frac{\partial u}{\partial x} + \sum_{k=1}^{N_s}\left(\frac{1}{2}\frac{(\gamma-1)\bar{W}T}{\gamma W_k}\right)\frac{\partial Y_k}{\partial x}
\end{pmatrix}
$$

where λ_i is a vector made up of the corresponding wave speed values, expressed by

$$\begin{pmatrix} \lambda_1 \\ \lambda_2 \\ \vdots \\ \lambda_{N_s+4} \\ \lambda_{N_s+5} \end{pmatrix} = \begin{pmatrix} u-c \\ u \\ \vdots \\ u \\ u+c \end{pmatrix}. \tag{44}$$

For a wave that is exiting the computational domain, the amplitude variation can be found from the interior information using the preceding forms for $\mathscr{L}_i$. However, waves that are entering the domain do not have the required information to compute wave amplitude variations. To facilitate this, Poinsot et al. [47] and Baum et al. [45] propose the use of a non-reacting LODI (local one-dimensional inviscid) system to estimate the amplitude variations at the boundaries. For temporally-integrated boundaries, the non-conservative form of the LODI system is written as

$$\frac{\partial \rho}{\partial t} + \frac{\rho \bar{C}_p}{c^2}\left(\mathscr{L}_1 + \mathscr{L}_{N_s+5}\right) + \mathscr{L}_{N_s+4} = 0 \tag{45a}$$

$$\frac{\partial T}{\partial t} + \mathscr{L}_1 + \mathscr{L}_{N_s+5} + \sum_{k=4}^{N_s+3} \mathscr{L}_k = 0 \tag{45b}$$

$$\frac{\partial u}{\partial t} + \frac{\bar{C}_p}{c}\left(\mathscr{L}_{N_s+5} - \mathscr{L}_1\right) = 0 \tag{45c}$$

$$\frac{\partial v}{\partial t} + \mathscr{L}_2 = 0 \tag{45d}$$

$$\frac{\partial w}{\partial t} + \mathscr{L}_3 = 0 \tag{45e}$$

$$\frac{\partial Y_1}{\partial t} - \frac{W_1}{\bar{W}}\left(\frac{\mathscr{L}_4}{T} - \frac{\mathscr{L}_{N_s+4}}{\rho}\right) = 0 \tag{45f}$$

$$\frac{\partial Y_j}{\partial t} - \frac{W_j}{\bar{W}T}\mathscr{L}_{j+3} = 0 \tag{45g}$$

where the series $j = 2, .., N_s$ still applies. These expressions can be applied to the $\mathscr{L}_i$ expressions in order to infer unknown wave amplitude information at the boundaries from known wave information. Extension of this wave analysis to the current boundary types is discussed in the following section.

3.2.3 Subsonic Inflow and Partially-Reflecting Outflow

- ***Subsonic Inflow***

In dealing with subsonic flows (where $u < c$), it is apparent that one of the numerical waves in Eqn. 44 has an opposing (negative) wave speed. At the inflow, $\mathscr{L}_1$ corresponds to an outgoing wave (with $\lambda_1 = (u - c) < 0$), while at the outflow it corresponds to an incoming wave. Since only outgoing waves can be computed from interior information (and all other waves are traveling in the direction opposite to $\mathscr{L}_1$), the inflow requires relationships to address the remaining $N_s + 4$ waves.

The first equation in $\mathscr{L}_i$ is used to compute the $\mathscr{L}_1$ value from the interior solution (for which spatial gradients in x are known):

$$\mathscr{L}_1 = \lambda_1 \left[\left(\tfrac{1}{2} \tfrac{(\gamma-1)T}{\gamma\rho} \right) \tfrac{\partial \rho}{\partial x} + \left(\tfrac{1}{2} \tfrac{\gamma-1}{\gamma} \right) \tfrac{\partial T}{\partial x} - \left(\tfrac{1}{2} \tfrac{c}{C_p} \right) \tfrac{\partial u}{\partial x} + \textstyle\sum_{k=1}^{N_s} \left(\tfrac{1}{2} \tfrac{(\gamma-1)\bar{W}T}{\gamma W_k} \right) \tfrac{\partial Y_k}{\partial x} \right] \tag{46}$$

To impose constant u-velocity at the inflow $\mathscr{L}_1 = \mathscr{L}_{N_s+5}$ must be applied as per LODI Eqn. 45c. To enforce constant y- and z-velocities at the inlet, the condition $\mathscr{L}_2 = \mathscr{L}_3 = 0$ must exist (as per Eqns. 45d and 45e). Similarly, a fixed reactant composition can be imposed for the set of $j = 2, .., N_s$ species mass fractions by setting $\mathscr{L}_j = 0$ in Eqn. 45g.

According to Eqn. 45f, setting the remaining mass fraction, Y_1, to a fixed value requires that $\mathscr{L}_4 = -(T/\rho)\mathscr{L}_{N_s+4}$. Although both $\mathscr{L}_4$ and $\mathscr{L}_{N_S+4}$ are unknown in this equation, a fixed inflow temperature can be imposed, resulting in the condition $\mathscr{L}_4 = -2\mathscr{L}_1$ (from setting $k = 4$ in Eqn. 45b). Applying this relationship to the previous one between $\mathscr{L}_4$ and $\mathscr{L}_{N_s+4}$ results in the form $\mathscr{L}_{N_s+4} = 2(\rho/T)\mathscr{L}_1$.

- ***Partially-Reflecting Subsonic Outflow***

The conditions for subsonic outflow are not quite as simple as those for subsonic inflow. As mentioned in the previous section, all waves, with the exception of the $\mathscr{L}_1$ wave, travel in the same direction. Waves that entered the domain at the inflow now exit the domain

at the outflow. This means that the wave amplitude variations for all $\mathscr{L}_{2,..,N_s+5}$ waves can be computed from the interior solution using their respective forms in the $\mathscr{L}_i$ equation set. Unfortunately, the $\mathscr{L}_1$ wave entering the domain requires special treatment.

Since the outflow is likely to experience an unsteady u-velocity, the application of $\mathscr{L}_1 = \mathscr{L}_{N_s+5}$ is no longer valid, as it was for the subsonic inflow. The simplest method would be to set a perfectly non-reflecting outflow, defined by $\mathscr{L}_1 = 0$. While this technique is numerically viable, it is physically irrelevant [45], according to

$$\frac{\partial p}{\partial t} + \rho \bar{C}_p \left(\mathscr{L}_1 + \mathscr{L}_{N_s+5} \right) = 0, \tag{47}$$

which is the LODI relationship for pressure. By imposing $\mathscr{L}_1 = 0$, the pressure at the outflow is controlled, solely, by outgoing wave information, meaning that there is no way to recover an average pressure for the system. As noted by Poinsot and Lele [47], the average pressure is dependent upon physical wave information that travels uptream from the infinity (i.e. far-field) location (p_∞).

A solution to this problem is proposed by Rudy and Strikwerda [48]. They note that a non-reflecting outflow boundary, such as the following one proposed by Hedstrom [49]

$$\frac{\partial \rho}{\partial t} - \rho c \frac{\partial u}{\partial t} = 0 \ , \tag{48}$$

can only supply outflow information based on the interior solution, and the steady-state solution will be heavily biased by the initial condition. Their solution to this problem is to impose an added condition of the form

$$\mathscr{L}_1 = \varepsilon \left(p - p_\infty \right) \ , \tag{49}$$

which mimics this physical process by allowing small acoustic waves to transmit pressure information into the domain through the outflow boundary. When applied to Hedstrom's

proposed non-reflecting outflow, the lone required boundary condition becomes

$$\underbrace{\overbrace{\frac{\partial \rho}{\partial t} - \rho c \frac{\partial u}{\partial t}}^{Hedstrom} + \varepsilon \left(p - p_{\infty} \right)}_{Rudy\,\&\,Strikwerda} = 0 \ . \tag{50}$$

The constant ε is used to control the rate at which the pressure in the system relaxes toward the imposed static pressure condition from the free-stream [47]. A formulation for the optimum value for ε has also been proposed by Rudy and Strikwerda:

$$\varepsilon = \frac{\left(1 - M^2\right) c}{2 \rho \bar{C}_p L}. \tag{51}$$

Here, M is the maximum Mach number occurring in the domain and L is a characteristic domain length, associated with the direction of the flow. Eqn. 51 takes advantage of the acoustic properties of the domain to determine a realistic rate at which the system could relax to p_{∞}.

For the flame-vortex interaction, characteristic boundaries are only considered at the inflow and the outflow. Therefore, the discussion provided here is directly applicable to the conditions selected for the problem. Difficulties associated with a multi-dimensional application of this technique need not be considered.

3.3 Computational Grid and Resolution

For simulation of non-uniform flows, DNS requires the use of a computational grid in which all scales of fluid motion are sufficiently resolved. In order to account for the smallest scales of turbulent motion, a DNS needs very fine grid spacing, which can become unjustifiably expensive for practical flow scenarios. The simulation of a reacting flow (e.g. combustion) further requires that the reaction zone be spatially resolved to facilitate narrow bands of reactivity, particular to trace species. Therefore, the minimum resolution is controlled by the physics of the flow and the spatial dimensions of the domain.

Flame-vortex interactions involve a single scale of fluid motion which is generally on

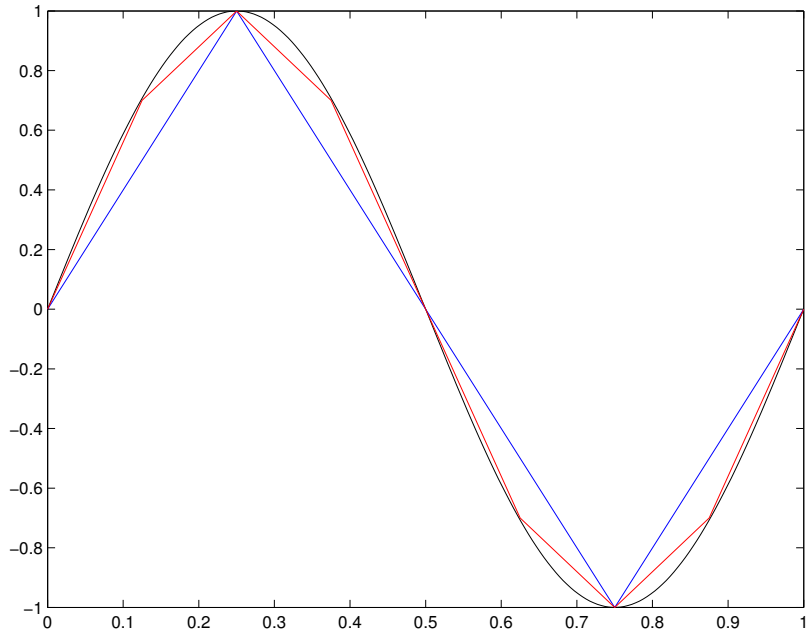

Figure 3: Resolution of a normalized $sin(0, 2\pi)$ function using four (4) and eight (8) points to represent the resolution of a non-linear reaction rate profile normal to the flame surface. Profiles show the true function (black), the 4-point resolution (blue) and the 8-point resolution (red).

the order of the flame thickness of larger. In the absence of multiple turbulence scales, the resolution is effectively controlled by the thickness of the flame, and it's associated reaction zone. This makes DNS a practical solution technique. Turbulent combustion simulations require adequate resolution of the flame zone in addition to turbulence models, or even greater resolution, that account for the small-scale motion. No such models or extended resolution are required in flame-vortex simulations as there is only a single, large-scale structure of fluid.

For radicals and trace species that are both formed and destroyed, chemical information must be supplied at a minimum of four points normal to the flame: cold flow, peak formation, peak destruction, and post-reaction. Such a formulation would result in an overly-simple profile that cannot accurately depict the non-linear nature of chemical source terms. While an infinite number of points is desirable, it is certainly not feasible. A more realistic and appropriate resolution of the reaction zone involves the use of 8 to 10 flame-normal points in which the four aforementioned points are represented, along with several

intermediate points. Fig. 3 illustrates this logic using a standard $sin(x)$ function (over a normalized $x = 0, 2\pi$) to represent the non-linear reaction rate profile.

For a 2-D problem, the x- and y-dimensions of the domain are generally known ahead of time. However, in cases where computational resources are a concern (such as DNS), it is often desirable to define maximum grid dimensions while achieving specific resolution of the physical problem. In these cases, the physical dimensions of the domain are defined by the grid. A combination of these two approaches has been adopted in this study.

Consider a laminar flame with an average reaction zone thickness of δ_{RZ}. In order to obtain a minimum of 8 points of resolution through the reaction zone, the spacing between cells must be $\delta_{RZ}/8$. In the case where desired grid dimensions are enforced, the size of the domain becomes

$$L_x = (N_x^p - 1)\,\frac{\delta_{RZ}}{8} \tag{52a}$$

$$L_y = \left(N_y^p - 1\right)\frac{\delta_{RZ}}{8} \tag{52b}$$

where N_x^p and N_y^p are the desired grid dimensions in x and y, resulting in a domain of size $L_x \times L_y$.

When a desired physical domain size is enforced (as is the case for most flame-vortex interactions), the grid is a function of the physical dimensions and the reaction zone characteristics. The corresponding values of N_x^p and N_y^p are easily determined by rearranging Eqn. 52. Since the vortex and flame parameters are problem-specific, there is no fixed technique for balancing L_i and N_i^p. For this study, computational expedience is generally sacrificed for physical accuracy. The typical rule-of-thumb is to define the streamwise length, L_x, as approximately 4 to 5 times d_c, and the transverse length, L_y, as approximately 2.5 to 3 times d_c, where d_c is the diameter of the vortex core.

As mentioned in the preceding section, the formulation is three-dimensional while the problem is inherently two-dimensional. However, numerical conditions (namely zero flux in the third dimension) can be applied to make the problem essentially 2-D. With such

conditions in place, any computation that is performed at adjacent z-locations is completely redundant. In other words, $\mathbf{Q}_{i,j,k+1} = \mathbf{Q}_{i,j,k}$ and $\mathbf{\Phi}_{i,j,k+1} = \mathbf{\Phi}_{i,j,k}$. Considering this fact, it is logical to design a grid that has $N_z^p = 1$. Information stored at a single cell center is sufficient for volumetric terms defined by the spatial formulation.

3.4 Flame and Flowfield Initialization

Initialization of the flame front and the flowfield is performed by a simple and fully repeatable procedure. After the computational grid is set up, a 1-D laminar premixed flame solution is obtained using Premix with the desired reactant stream and flow conditions. This solution is then superimposed onto the uniform DNS grid in the streamwise direction using a fourth-order-spline interpolation. Premix uses an adaptive mesh solver, resulting in a non-uniform distribution of gridpoints in the streamwise direction, therefore, re-distribution of the data to the desired grid is necessary to locate the flame appropriately. (For very coarse grids, linear interpolation is not particularly accurate, however, the DNS code recovers the solution quickly.) Following interpolation, this 1-D solution is then distributed over the rest of the domain resulting in a 2-D planar flame front.

Included in the superimposed flame solution are profiles for temperature, gas velocity, density, species mass fractions, and static pressure. The assumption of a constant-pressure system is valid for this problem, however, slight variations in pressure are experienced through the flame and must be accounted for. The inclusion of chemical source terms is not necessary, as the chemistry subroutine picks up on the initial concentrations and begins computation during the first timestep.

The ability to control the flame location is quite important in the flame-vortex initialization. Since the flame is stationary in the uniform flow, it must be placed in a position that will not compromise continuity of its surface during extreme stretching. Its location must also facilitate initialization of the vortex pair such that the two do not make premature contact with one another. Once this position is determined, a pair of decaying laminar vortices, based loosely on the incompressible Lamb vortex [50], are superimposed upstream of the flame. The 2-D Cartesian velocity components, u and v, at a local position (x,y) are

given by

$$u(x,y) = u_0(x,y) - \Delta y \ \frac{A \ \beta \ c_0}{r_c^2} \tag{53a}$$

$$v(x,y) = v_0(x,y) + \Delta x \ \frac{A \ \beta \ c_0}{r_c^2} \tag{53b}$$

$$ln(A) = -\frac{\Delta x^2 + \Delta y^2}{2r_c^2}. \tag{53c}$$

Here, u_0 and v_0 represent the original velocity components of the reactant stream, c_0 is the reference speed of sound, ρ_0 is the reference density, r_c is the core radius, β is a characteristic length, and $(\Delta x, \ \Delta y)$ represent the $x-$ and $y-$distances to the vortex center. The sign on A controls the rotational orientation of the vortex, as determined by the right hand rule. These components are accompanied by a pressure correction of the form

$$p(x,y) = p_0(x,y) - \rho_0 \ \frac{A \ \beta^2 \ c_0^2}{r_c^2}. \tag{54}$$

The purpose of this correction is to account for the hydrodynamic pressure gradient induced by the low-pressure vortex centers. Similar corrections are made for the density under the perfect gas assumption (Eqn. 10).

CHAPTER IV

PRELIMINARY VALIDATION

The objectives of this study can be divided into two categories: 1-D laminar flames (Objs. 1 and 2), and 2-D laminar flames (Objs. 3 and 4). This chapter covers validation studies of the aforementioned computational models using, strictly, 1-D laminar flames.

4.1 Chemical Mechanism Validation

In order to simulate reactive flows, a set of representative chemical reactions (commonly referred to as a *chemical mechanism*) must be considered to model the temporal evolution of reactive scalars. *Reduced chemical mechanisms* are generated to emphasize probable reactions and incorporate chemical species that are of greater relevance (or interest). In this sense, the selection of a reduced chemical mechanism for simulation is not arbitrary.

The use of a full chemical mechanism, such as the GRI-Mech [30], is feasible for simplified, steady-state computations such as those performed in Chemkin-II [33]. A full mechanism is the most-accurate means of reproducing the chemical processes that occur within a reactive flow, as it contains a broad spectrum of primary and intermediate reactions and species. However, implementation of such a mechanism in an unsteady DNS code is not practical as the cost of the chemical computations would be a tremendous burden.

While the cost of computation is an important factor, the accuracy of the physics is of greater importance to the current study. Often times, *single-step mechanisms* are employed, utilizing the assumption that reactants are converted to products in a single step ($Reactants \rightarrow Products$), according to the Arrhenius rate law (Eqn. 19) discussed in Sec. 2.1.1. However, the flame characteristics may experience substantial variations, based on the specification of independent variables (ψ and E_A). Such an assumption also de-emphasizes the importance of intermediate reactions and species which can drastically change the structure of the flame, particularly during unsteady processes.

Reduced chemical mechanisms are designed to address, both, physical accuracy and computational efficiency. A reduced chemical mechanism proposed by Sung et al. [51] has been selected to describe the chemical processes taking place. It consists of 16 chemical species,

$$\begin{aligned} Major: &\quad CH_4,\, O_2,\, N_2,\, CO_2,\, H_2O \\ Minor: &\quad H,\, H_2,\, OH,\, HO_2, H_2O_2,\, CH_2O,\, CH_3,\, CO,\, C_2H_2,\, C_2H_4,\, C_2H_6, \end{aligned}$$

that make up the following (12) reversible reactions:

$$\begin{aligned} &(a) \quad H + OH \rightleftharpoons H_2O \\ &(b) \quad O_2 + 2CO \rightleftharpoons 2CO_2 \\ &(c) \quad O_2 + \tfrac{1}{2}C_2H_2 \rightleftharpoons H + CO_2 \\ &(d) \quad HO_2 + CO \rightleftharpoons OH + CO_2 \\ &(e) \quad H + O_2 + CO \rightleftharpoons OH + CO_2 \\ &(f) \quad O_2 + 2CH_3 \rightleftharpoons H_2 + CH_4 + CO_2 \\ &(g) \quad H_2 + O_2 + CO \rightleftharpoons H + OH + CO_2 \\ &(h) \quad O_2 + CH_3 + CO \rightleftharpoons H + CO_2 + CH_2O \\ &(i) \quad O_2 + H_2O_2 + CO \rightleftharpoons OH + HO_2 + CO_2 \\ &(j) \quad O_2 + CO + C_2H_6 \rightleftharpoons CH_4 + CO_2 + CH_2O \\ &(k) \quad O_2 + 2CH_3 + CO \rightleftharpoons CH_4 + CO_2 + CH_2O \\ &(l) \quad O_2 + CH_3 + CO + C_2H_4 \rightleftharpoons CH_4 + CO_2 + CH_2O + \tfrac{1}{2}C_2H_2 \end{aligned} \tag{55}$$

The mechanism, reduced from GRI-Mech 1.2, represents all of the major species for methane oxidation and the applied, minor *syngas* species (H_2 and CO).

4.1.1 Freely-Propagating Laminar Flame

In order to study stretched flames in various reactant mixtures, they must share one or more characteristics when they are not stretched. As mentioned in Section 1.3.1, changes to the fuel content can produce laminar flames with a wide range of properties, some of which coincide. Two key properties of relevance to this study are the laminar flame speed, S_L,

and the flame heat release which is a function of the flame temperature, T. Separately, they represent the velocity and the intensity of the flame front in a uniform flow. Collectively, however, they represent the reactivity of a particular mixture in a qualitative sense.

Since the flames are to be parameterized by laminar characteristics, Premix [31] is used to test the validity of the reduced chemical mechanism as it relates to those particular properties. Fuel-lean mixtures have been generated for $CH_4/CO/Air$, and $CH_4/H_2/Air$, with pure methane fuel mixtures represented by $\chi_{CO,H_2} = 0$. The mixtures, themselves, are parameterized by the molar fraction of *syngas* in the fuel (e.g. $\chi_{fuel} = \chi_{CH_4} + \chi_{CO,H_2}$), and the corresponding equivalence ratio. A conserved scalar formulation,

$$z = (\chi_{CH_4} + \chi_{CO})\frac{MW_C}{MW_{mix}} + (2\chi_{CH_4} + \chi_{H_2})\frac{MW_{H_2}}{MW_{mix}} \ , \tag{56}$$

typical in non-premixed systems [35], is used to define a fuel mixture fraction which can be directly related to an equivalence ratio for a premixed system by

$$\phi = \frac{z/(1-z)}{(F/A)_{stoic}} \tag{57}$$

In Eqns. 56 and 57, z is the mixture fraction, χ_k is the mole fraction of the k^{th} species, MW_k is the molecular weight of the k^{th} species, and $(F/A)_{stoic}$ is the fuel-to-air mass ratio of the analogous stoichiometric mixture.

Reactant mixtures are formulated at standard temperature (298 K) and pressure (1 atm) over ranges of $\phi = [0.6, 0.8]$ and $\chi_{syn}/\chi_{CH_4} = [0.0, 0.8]$. These mixtures are then used to simulate steady, freely-propagating flames in Premix using GRI-Mech 3.0 and the 12-step mechanism.

Quantitative comparison of these simulations yields a range of agreement between the full and reduced mechanisms. Figure 4a shows S_L results for $CH_4/H_2/Air$ mixtures over the aforementioned range of equivalence and species ratios.

From general observation, it is apparent that the agreement between flame speed values is stronger for leaner mixtures with lower contents of H_2 fuel. This agreement is better

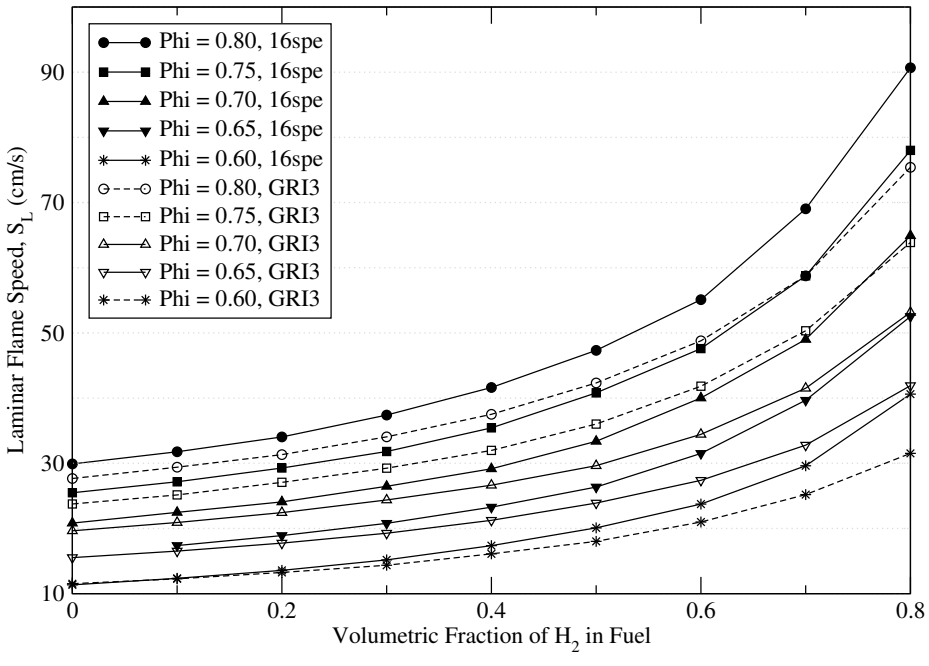

(a)

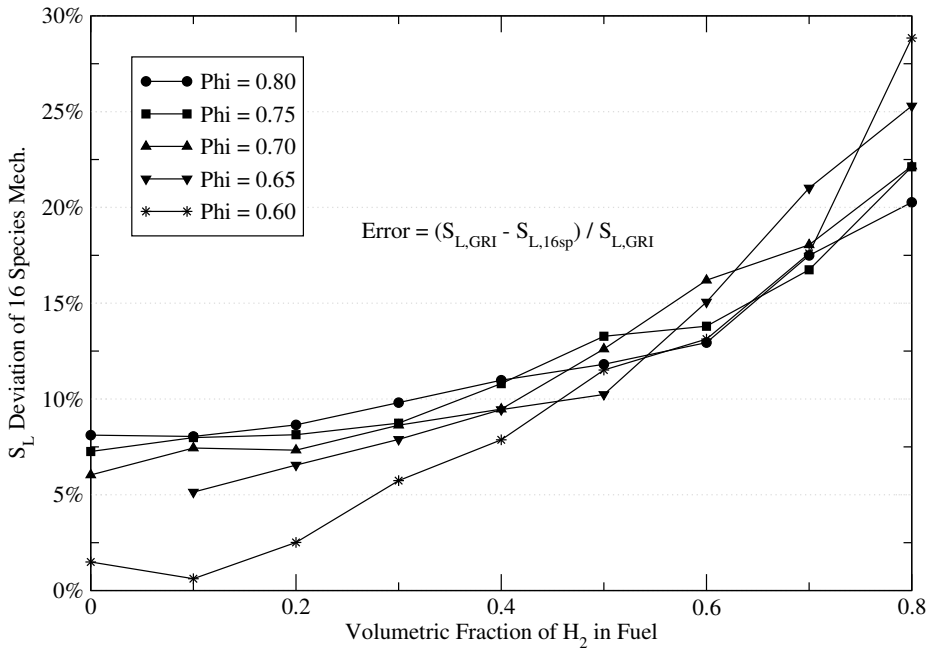

(b)

Figure 4: (a) Laminar flame speed, and (b) relative flame speed error between GRI-Mech 3.0 and the reduced, 12-step mechanism for CH_4/H_2 fuel. Good agreement is observed for H_2 fuel volumes up to 40%.

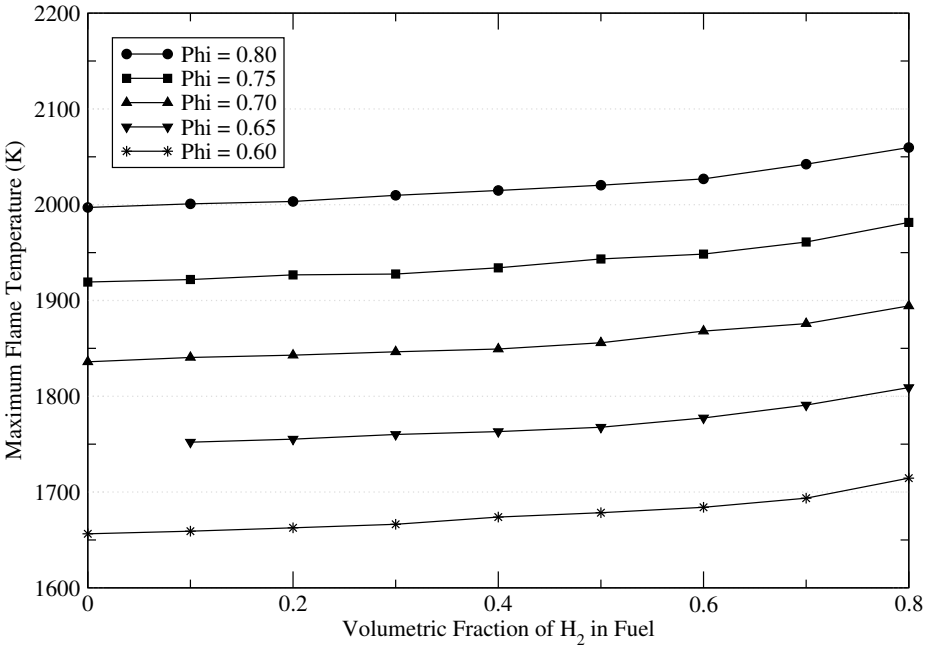

(a)

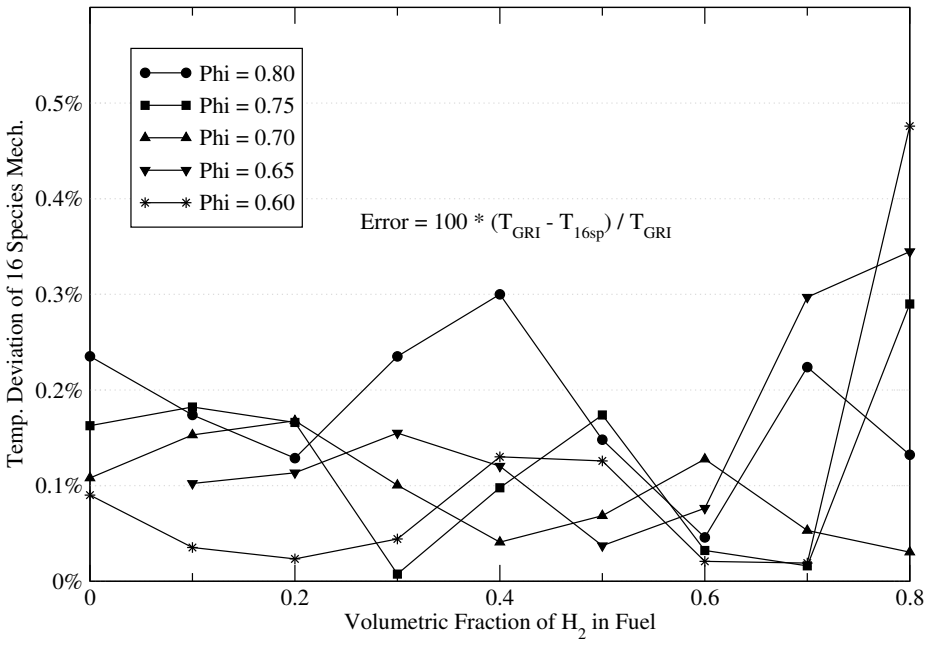

(b)

Figure 5: (a) Maximum flame temperature, and (b) relative flame temperature error between GRI-Mech 3.0 and the reduced, 12-step mechanism for CH_4/H_2 fuel. Agreement is excellent at all points, and observable errors are essentially negligible.

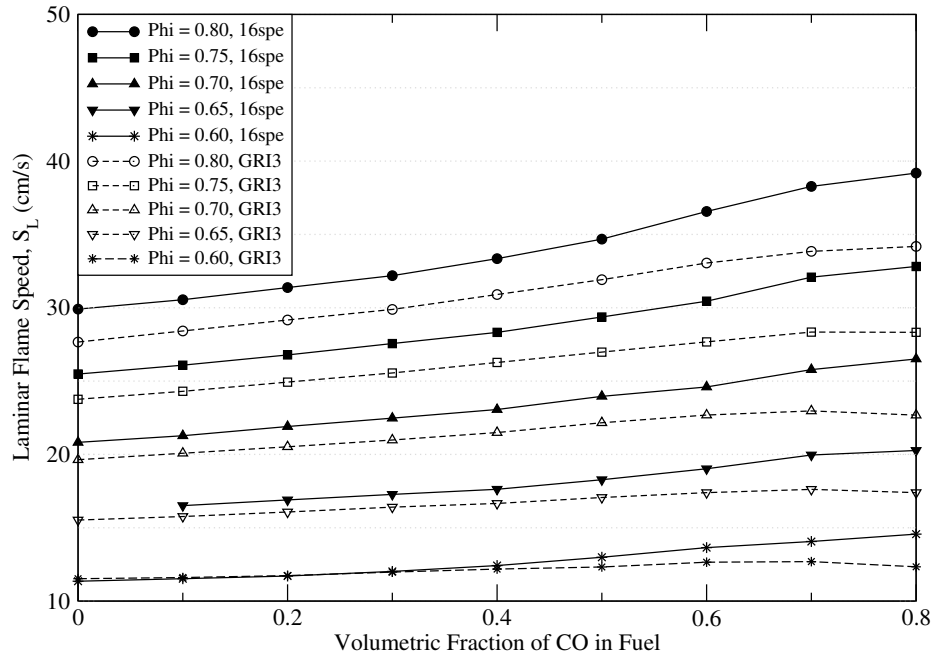

(a)

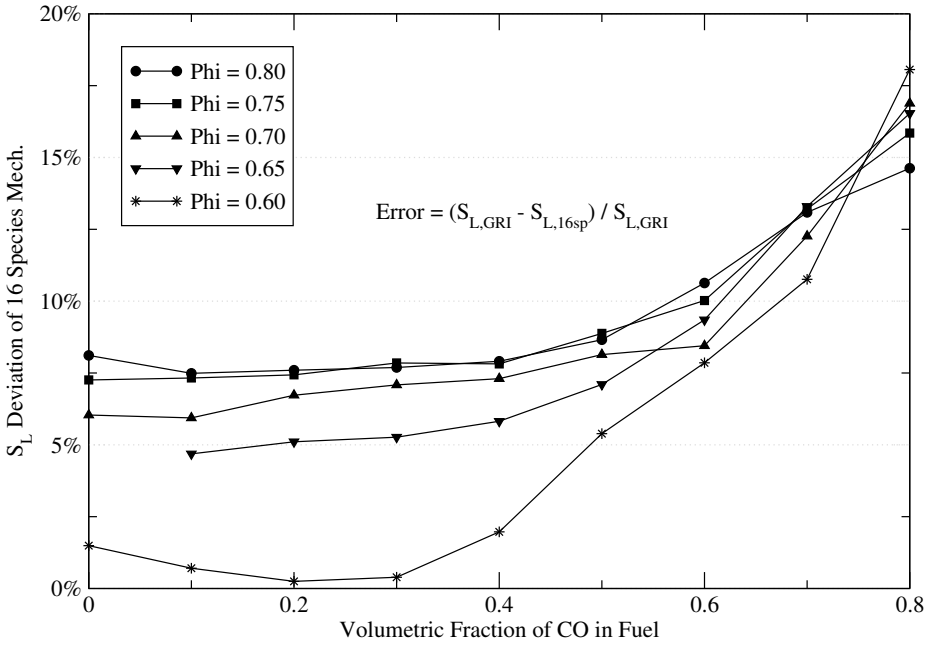

(b)

Figure 6: (a) Laminar flame speed, and (b) relative flame speed error between GRI-Mech 3.0 and the reduced, 12-step mechanism for CH_4/CO fuel. Good agreement is observed for CO fuel volumes up to 60%.

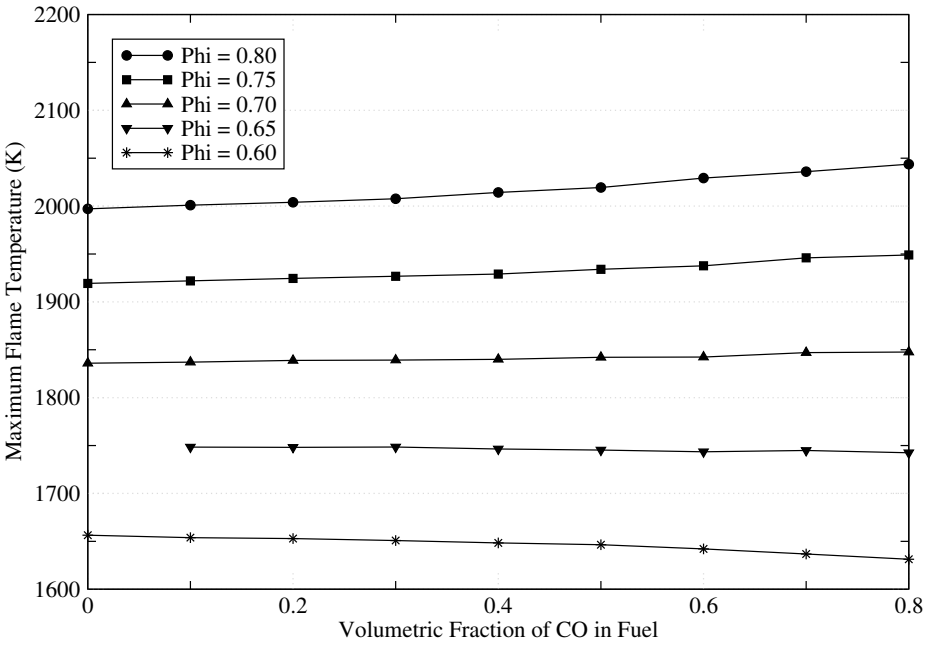

(a)

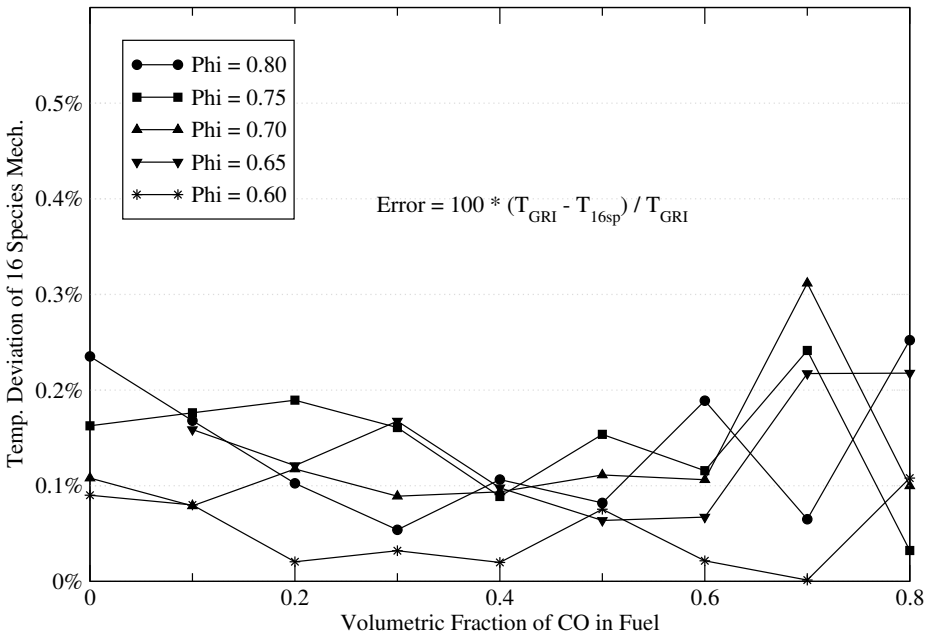

(b)

Figure 7: (a) Maximum flame temperature, and (b) relative flame temperature error between GRI-Mech 3.0 and the reduced, 12-step mechanism for CH_4/CO fuel. Again, the agreement is excellent at all points, with essentially negligible error.

demonstrated in Fig. 4b which addresses the error between the specific flame speed values, assuming that GRI-Mech produces the accepted value. For mixtures at $\phi \leq 0.7$, the error in flame speed is consistently below 10%, which has been prescribed as the cutoff for error acceptability in this study.

Although the flame speed values produce a broad range of agreement, the opposite is true of the corresponding flame temperatures. Fig. 5a demonstrates the excellent agreement in flame temperature data observed between the two mechanisms. The maximum computed error between the two mechanisms is below 0.5% at all points, as revealed in Fig. 5b with no distinguished pattern. This further qualifies the use of flame speed error as the defining factor for setting acceptibility limits.

Similar trends are observed for the $CH_4/CO/Air$ mixtures. Once again, the laminar flame speed data in Fig. 6a shows that the reduced mechanism tends to agree with GRI-Mech for lower equivalence ratios and lower fractions of secondary fuel (in this case, CO). However, for comparable mixing ratios ($\chi_{CO}/\chi_{CH_4} = \chi_{H_2}/\chi_{CH_4}$), the flame speed error is generally lower for the CH_4/CO fuel mixtures. As shown by Fig. 6b, the majority of the error lies within the acceptable limits up to CO fuel volumes of 60%. This is especially true for lean mixtures having $\phi \leq 0.7$, which tend to agree more.

Flame temperature trends are consistent with those observed for the CH_4/H_2 fuel (Fig. 7a). Once again, the relative flame temperature error between the full and reduced mechanisms is minor. The maximum computed error in Fig. 7b is around 0.3%, with the majority of the values lying below 0.2%. As in the CH_4/H_2 fuel cases, the fuel mixing limit is defined by the 10% S_L-error cutoff, which occurs at 40/60 CH_4/CO, as opposed to 60/40 CH_4/H_2.

4.1.2 Selection of Laminar Flame Cases

In characterizing these unstretched laminar premixed flames, flame speed and heat release are the key parameters of interest. These two properties have been easily obtained using Premix. However, for the remaining work, it is not feasible to consider all of the laminar flame cases that have been investigated up to this point. Instead, cases representing the three fuel mixtures (CH_4, CH_4/CO, and CH_4/H_2) must be generated from the data

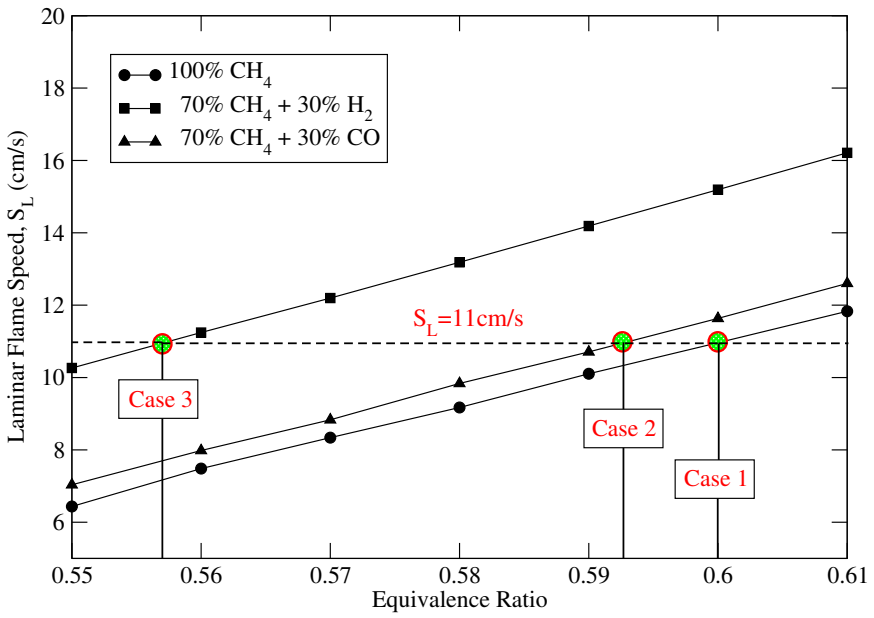

Figure 8: Laminar flame speed, S_L, as a function of equivalence ratio, ϕ. Three laminar laminar flame cases selected for simulation are marked on the figure. $S_L \approx 11\,cm/s$ for all cases. Respective equivalence ratios are 0.60 (Case 1), 0.593 (Case 2), and 0.557 (Case 3).

obtained in Premix.

Figure 8 shows flame speed data as a function of the equivalence ratio for three different fuel mixtures: 100% CH_4, 70/30% CH_4/CO, and 70/30% CH_4/H_2 by volume. The two-component (70/30) fuel mixtures are selected based on the previously-determined range of acceptability. For equivalence ratios ranging from 0.55 to 0.61, it is obvious that each mixture behaves differently according to stoichiometry (more so for the hydrogen-methane mixtures). For this reason, the cases are selected based on similar chemical properties rather than similar mixture properties.

The first case (Case 1) is a pure methane-air flame (ϕ=0.60) with a laminar flame speed of approximately 11 cm/s. Extending this fixed S_L value to the remaining two curves yields two additional cases: $CH_4/CO/Air$ at ϕ=0.593 (Case 2) and $CH_4/H_2/Air$ at ϕ=0.557 (Case 3). Each of these three cases is assigned a heat release parameter, η, of the form

$$\eta = \frac{T_P - T_R}{T_R} \tag{58}$$

where T_R and T_P are the reactant and product temperatures, respectively. These values are found to be 4.54, 4.47, and 4.37 for Cases 1, 2, and 3. The difference between the three is, at most, 3.7%, indicating that each of these three flames experience very similar heat release, as well as flame speed.

Another parameter that is of great importance in this study is the flame thickness. Since the three cases share a common flame speed and heat release, it is logical to conclude that their flame thicknesses are comparable. The formula $\delta_F = 7.4\alpha/S_L$ has been employed by Mueller et al. [1], Roberts et al. [26], and several other authors to address the thickness of hydrocarbon-air flames. Here, δ_F represents the thermal thickness of the flame, and α is the thermal diffusivity of the reactant mixture. It is clear that, between the three cases, δ_F is simply a function of α, which can be easily determined by the form

$$\alpha = \frac{\kappa}{\rho C_p} \tag{59}$$

where ρ is the fluid density, κ is the thermal conductivity, and C_p is the constant-pressure specific heat. The latter two are obtained using polynomial curvefit data from the thermal [52] and transport [38] databases in Chemkin-II.

The specific thermal diffusivity values are found to be 0.2261, 0.2255, and 0.2296 cm^2/s inside the cold reactant streams for Cases 1-3. With matching flame speeds, these thermal diffusivity values produce flame thicknesses that are within 1-2% of one another. On the basis of flame speed, heat release, and flame thickness, it is safe to conclude that the three selected laminar flames (representing CH_4, CH_4/CO, and CH_4/H_2 fuel mixtures) are effectively the same.

4.1.3 Strained Laminar Flames

In flame-vortex interactions, the flame is subjected to a non-uniform flow, in which the surface experiences straining. Therefore, the chemical mechanism must demonstrate the ability to adequately predict flame characteristics in non-uniform flows. To perform this validation, the reduced chemical mechanism is implemented in OPPDIF [32] and compared

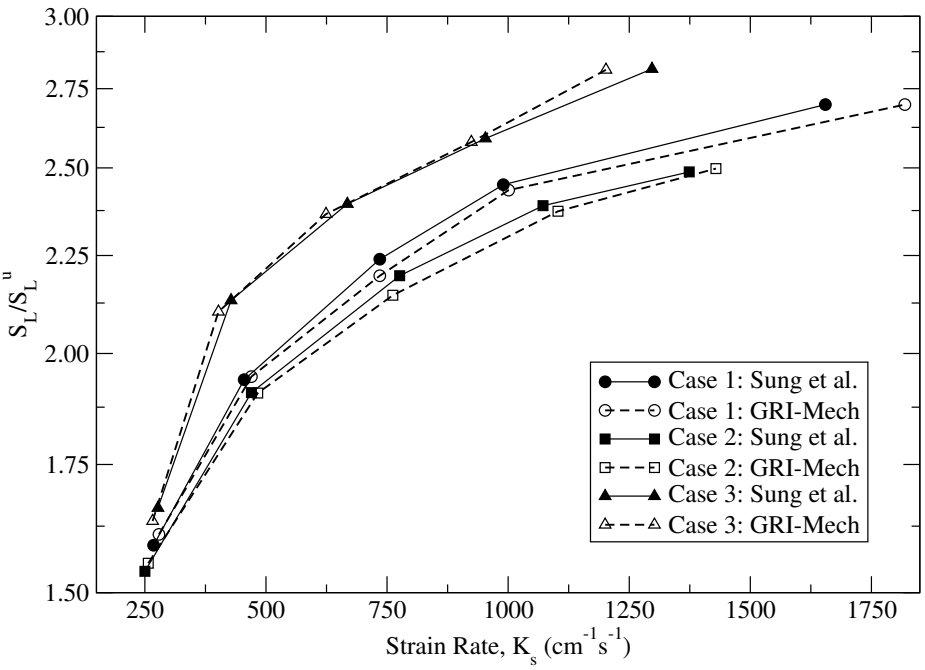

Figure 9: Comparison of stretched flame speeds (S_L) as a function of strain rate (K_s) for the three laminar flame cases. Agreement between GRI-Mech 3.0 and the reduced Sung et al. mechanism generally yields good agreement for all cases. Best agreement is for the Case 3 ($CH_4/H_2/Air$) flames. Strain rates are varied by nozzle velocities between 20 and 100 cm/s over a 1 cm nozzle separation.

with the GRI-Mech. OPPDIF is designed to compute steady-state, diffusion flames in a 2-D axisymmetric flowfield between two opposing nozzles (one issuing fuel, the other issuing oxidizer). Through the use of similarity transformations, Kee et al. [53] have reduced the 2-D axisymmetric problem to a 1-D problem.

The concept behind OPPDIF is quite simple. Fuel and oxidizer streams are directed toward one another creating a stagnation plane somewhere in-between the two. In most cases, fuel molecules diffuse through the stagnation plane and create a single diffusion flame on the oxidizer side. In order to simulate premixed flames, the separate fuel and oxidizer streams are replaced by two premixed streams, thus creating a pair of strained laminar flames (as originally formulated by Kee et al.).

Recognizing the axisymmetry of the flow, mass conservation is given in cylindrical co-ordinates as

$$\frac{\partial}{\partial x}(\rho u) + \frac{1}{r}\frac{\partial}{\partial r}(\rho v r) \ . \tag{60}$$

According to von Karman [54], the radial velocity, v/r, is only a function of the x-location, thus prompting Lutz et al. [32] to define a continuity function of the form

$$G(x) = -\frac{\rho v}{r} \ . \tag{61}$$

In the 1-D sense, the rate of shear strain, K_s, at a location, x, is the axial gradient of $G(x)$. This is simply represented by

$$K_s(x) = \frac{\partial}{\partial x}\left(\frac{G(x)}{\rho}\right) \tag{62}$$

Figure 9 shows non-dimensional stretched flame speeds, S_L/S_L^u, as a function of shear strain rates for several opposed-flow solutions. Nozzle velocities ranging from 20 to 100 cm/s are applied over a nozzle separation of 1 cm to produce premixed flames with various strain rates (in which higher nozzle velocities result in higher K_s). The strain rates are determined using a second-order central difference scheme (over uniform-grid locations) to compute the axial gradient of G/ρ:

$$K_{s,i} = \frac{(G/\rho)_{i+1} - (G/\rho)_{i-1}}{2\,(x_i - x_{i-1})} \ . \tag{63}$$

The stretched flame speed, S_L, is taken to be the gas velocity, u, at a location just ahead of the flame (prior to gas expansion). This corresponds to the location at which the strain rate measurements are made. Over the represented range of strain rates, the reduced Sung et al. mechanism and GRI-Mech 3.0 show good agreement. The curves for Case 1 (CH_4/Air) and Case 2 ($CH_4/CO/Air$) flames are located very close to one another, while the Case 3 ($CH_4/H_2/Air$) curve stands apart. Stretched flame speeds are greatest

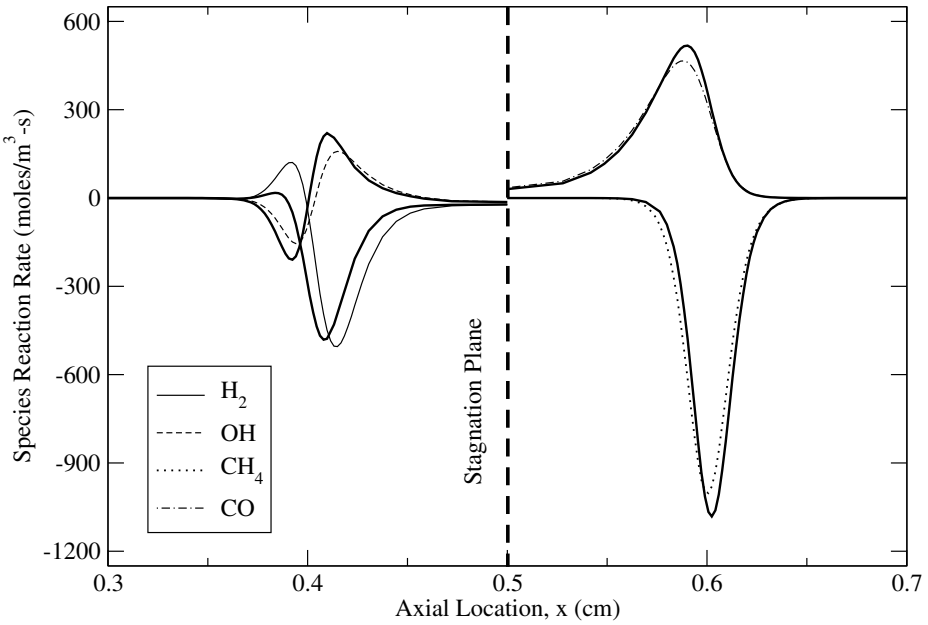

Figure 10: Reaction rate trends for several species in the strained Case 3 flame. The nozzle velocity is 60 cm/s resulting in a flame speed of approximately 26.3 cm/s and a strain rate of 624 $(cm \cdot s)^{-1}$. Thin, patterned lines represent the GRI-Mech 3.0 solutions and the adjacent heavy lines represent the reduced mechanism solutions.

for the Case 3 flames and lowest for the Case 2 flames. This is analogous to results reported in previous studies (Sec. 1.3.1) for which H/C-hydrogen mixtures are shown to produce greater stretched and unstretched flame speeds.

As observed in the Premix solutions, the flame temperatures produced by the two mechanisms are, for all practical purposes, identical. The vast difference in species and reactions represented makes a quantitative comparison of chemical data inappropriate. However, qualitative comparison reveals that the reaction rate trends for relevant species are the same, and often vary by no more than 10-20%. An example of this is given for the Case 3 flame in Figure 10.

4.2 DNS of Laminar Premixed Flames

Once the chemical mechanism is selected and validated, it is implemented in the DNS code that will ultimately be used for the flame-vortex simulations. The code, which has been extensively covered in Chapter 2, is scaled down to resemble a 1-D laminar flame simulation,

comparable to that of Premix. The integration schemes used in Premix and the DNS code are not identical, however, the physical models are essentially the same. This means that a direct comparison of Premix solutions and the DNS solutions should yield very good agreement.

The DNS is performed in two phases for each laminar flame case discussed in Sec. 4.1.2. The first phase is a precise (but expensive) direct integration of the chemical source terms (denoted DNS/DI), while the second phase uses the efficient ISAT storage-retrieval algorithm (denoted DNS/ISAT) to determine the chemical source terms. In doing so, the accuracy of the DNS code and the ISAT algorithm can be addressed simultaneously.

Previous analyses have shown that comparisons between instantaneous DNS results and Premix results reveal good agreement between variables such as density, pressure, and temperature. However, upon inspection, it was found that species reaction rates, and their corresponding concentrations, often varied substantially. Therefore, validation of the laminar flame DNS hinges on the 1-to-1 comparison of individual reaction rates and concentrations. To resolve the discrepancy between Premix, DNS/DI, and DNS/ISAT solutions, all chemical source terms and concentrations are normalized according to

$$RR_k = \frac{\dot{w}_k}{|\dot{w}_k|_{max}} \tag{64a}$$

$$C_k = \frac{\rho Y_k}{(\rho Y_k)_{max}} \tag{64b}$$

where RR_k and C_k are the normalized reaction rate and normalized concentration of the k^{th} species, respectively. All reaction rates and concentrations are normalized by the maximum absolute value that is observed between the three different solutions. This ensures consistency among relative magnitudes and provides an accurate quantitative comparison.

4.2.1 1-D DNS Validation Cases

As previously mentioned, the DNS code is often capable of reproducing primitive variables, such as temperature and density, even when chemical source terms are inconsistent with Premix. For the three validation cases, the former is a recurring feature. Figures, 11a

and 11b demonstrate the excellent agreement between the temperature and density profiles generated by Premix, DNS/DI, and DNS/ISAT.

While instantaneous agreement of primitive variables is essential to the validation, it is irrelevant with regard to long-term unsteady simulations. For this reason, the chemical source terms and species concentrations must show acceptable instantaneous agreement in order to ensure the long-term validity of the DNS code.

- ***Case 1 Results:***

The first case selected for validation is the control case flame. For the purpose of visual clarity, symbols representing the Premix solution are shown for every third point. The major species reaction rate profiles in Fig. 12a show excellent agreement between the three different solutions. The DNS/DI solution reproduces the Premix solution with impeccable accuracy. DNS/ISAT solutions for the product species (CO_2 and H_2O) show slight deviations from Premix that are visible only when compared to the DNS/DI solutions.

Reaction rate profiles for the select minor species (Fig. 12b) show stronger deviations than those of the major species. As before, this is only true for the DNS/ISAT solution. The DNS/DI solution is, once again, in excellent agreement with Premix. Strong fluctuations in the H_2 and OH profiles are observed at the tail end of the primary reaction zone. These fluctuations are characteristic of ISAT solutions and are, at most, 20% of the maximum reaction rate magnitude. Despite their notable magnitude, the impact of these recurring fluctuations is nearly insignificant.

Normalized concentration profiles for the major species are shown in Fig. 13a. Much like their respective reaction rates, the three solutions show excellent agreement among all four major species. The slight disagreement between DNS/DI and DNS/ISAT reaction rates has no visible impact on the accuracy of the concentrations. Both DNS solutions match the Premix solution with remarkable accuracy.

The minor species concentrations (Fig. 13b) demonstrate agreement comparable to that of the major species concentrations. The substantial reaction rate fluctuations for H_2 and OH have no apparent effect on their respective concentrations. Another consistent feature

(a) Temperature

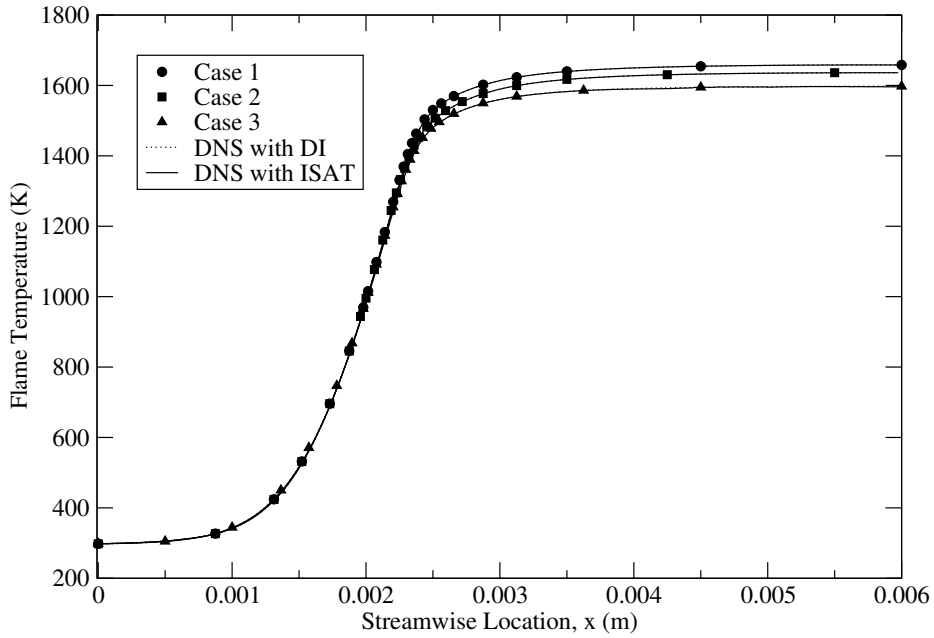

(b) Density

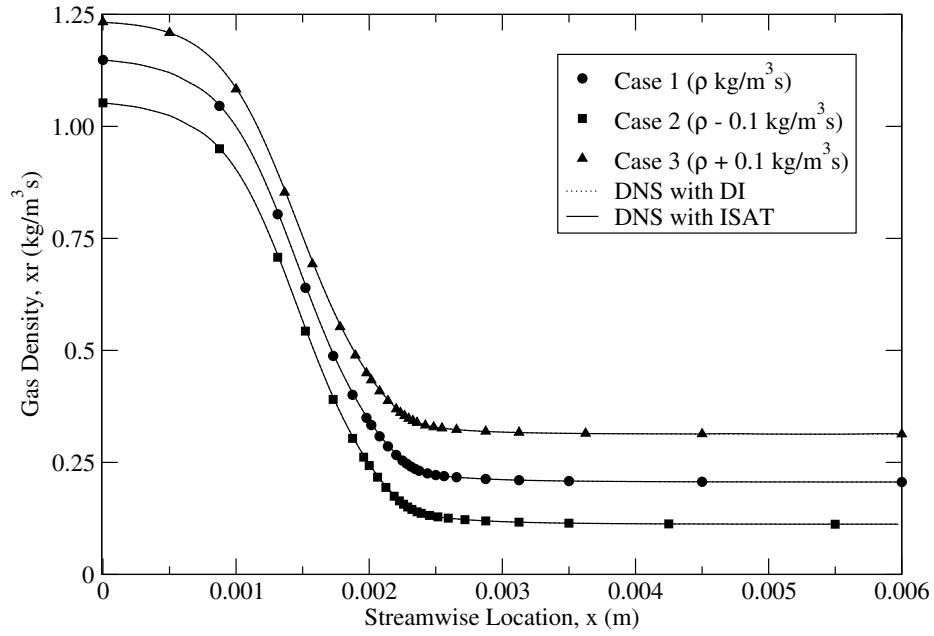

Figure 11: (a) Temperature and (b) density profiles for the three flame cases. Density values for Case 2 are offset by -0.1 kg/m^3s and values for Case 3 are offset by +0.1 kg/m^3s to distinguish between cases. For both temperature and density, excellent agreement is observed at all locations between the Premix, DNS/DI, and DNS/ISAT solutions.

(a) RR_k for major species: O_2, H_2O, CH_4, and CO_2

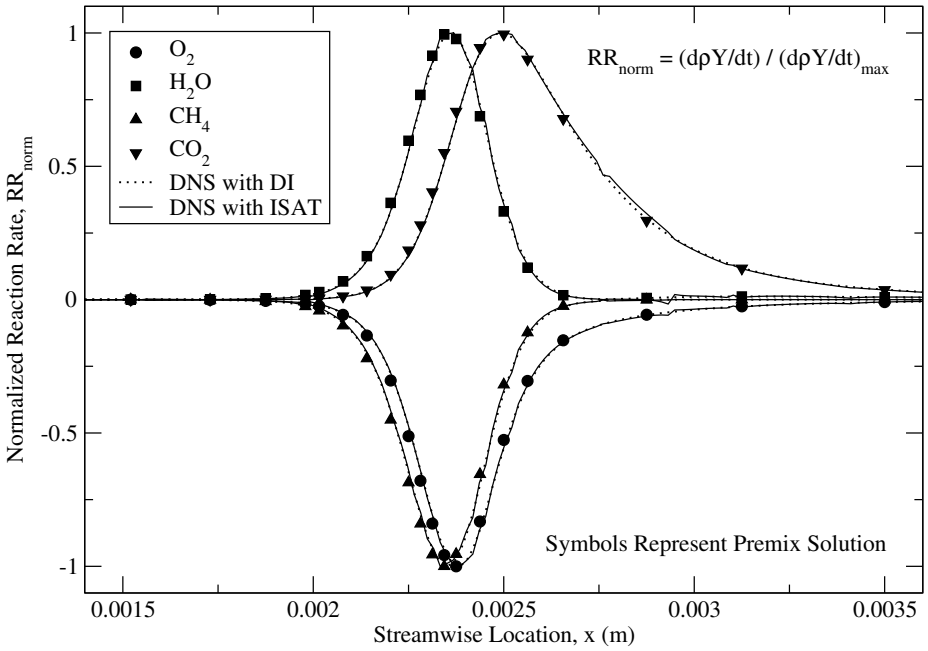

(b) RR_k for minor species: H_2, OH, and CO

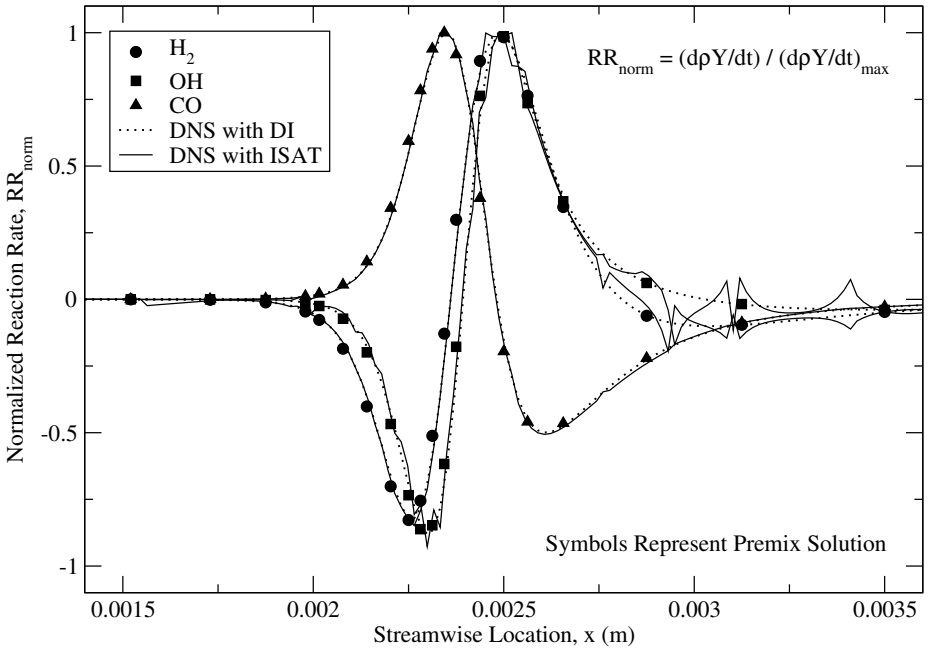

Figure 12: Case 1 normalized reaction rates for the (a) major species and (b) minor species. Agreement between the three solutions is excellent for all major species. Substantial fluctuations are observed in the DNS/ISAT solution for minor species H_2 and OH.

(a) C_k for major species: O_2, H_2O, CH_4, and CO_2

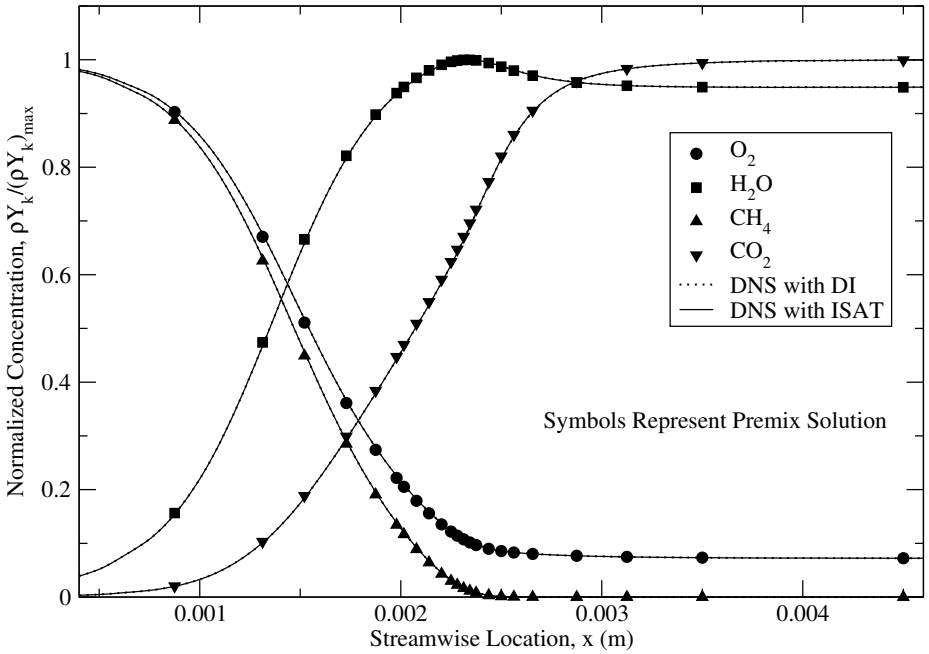

(b) C_k for minor species: H_2, OH, and CO

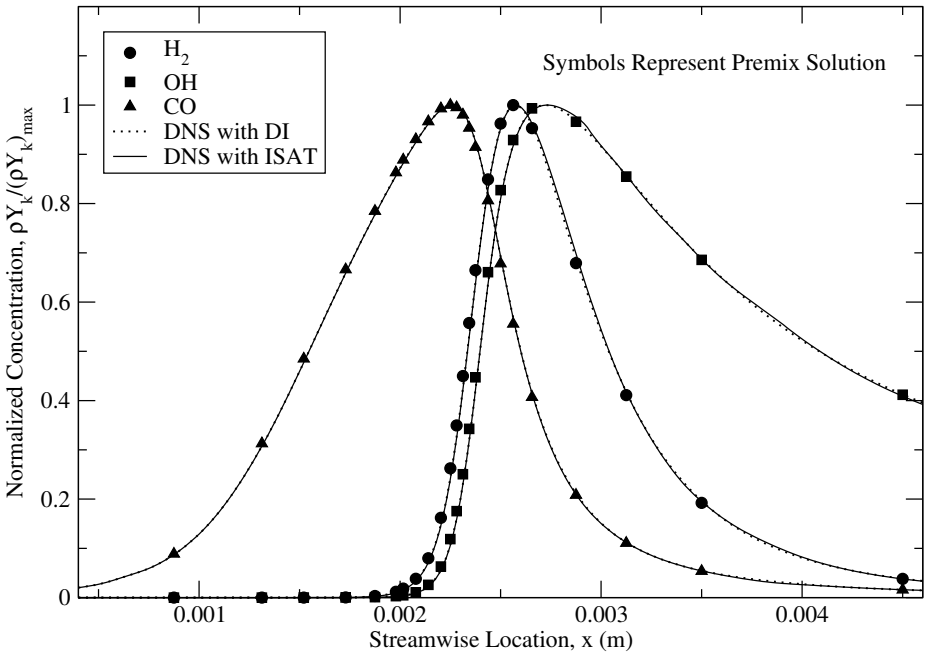

Figure 13: Case 1 normalized concentrations for the (a) major species and (b) minor species. Agreement between the three solutions is excellent for both major and minor species. Despite large fluctuations in RR_{H_2} and RR_{OH}, the concentration profiles are smooth.

(a) RR_k for major species: O_2, H_2O, CH_4, and CO_2

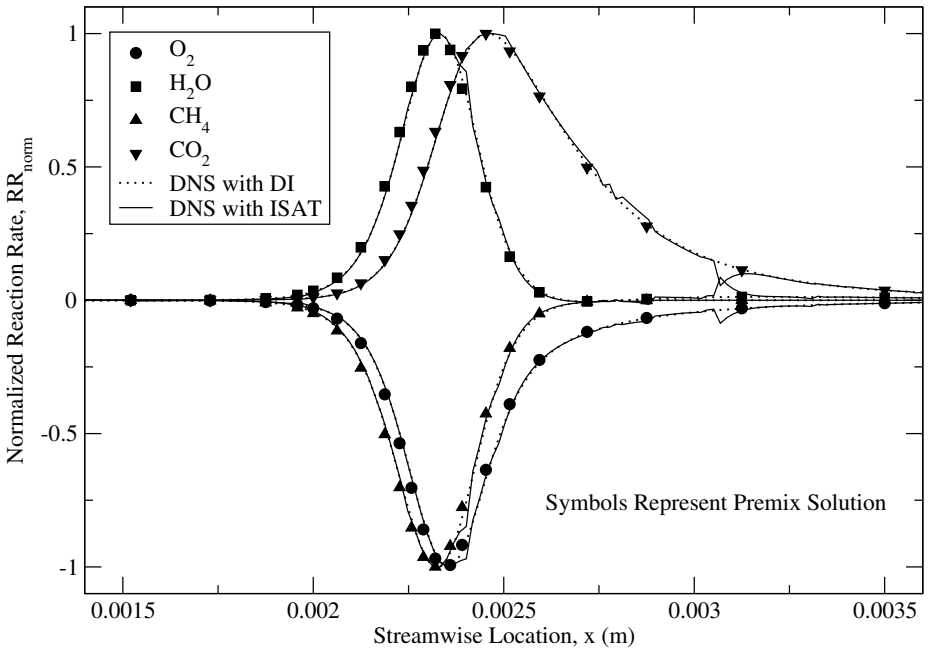

(b) RR_k for minor species: H_2, OH, and CO

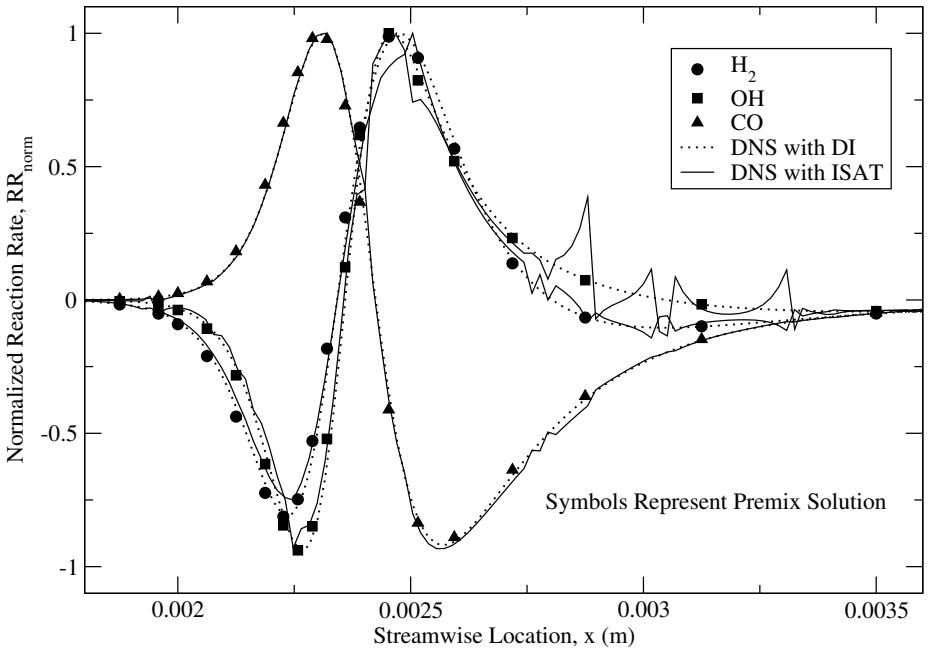

Figure 14: Case 2 normalized reaction rates for (a) major and (b) minor species. Slight fluctuations are observed in the DNS/ISAT solution for all major species but RR_{CH_4}. Visibly large fluctuations are observed in the DNS/ISAT solution of minor species reaction rates.

(a) C_k for major species: O_2, H_2O, CH_4, and CO_2

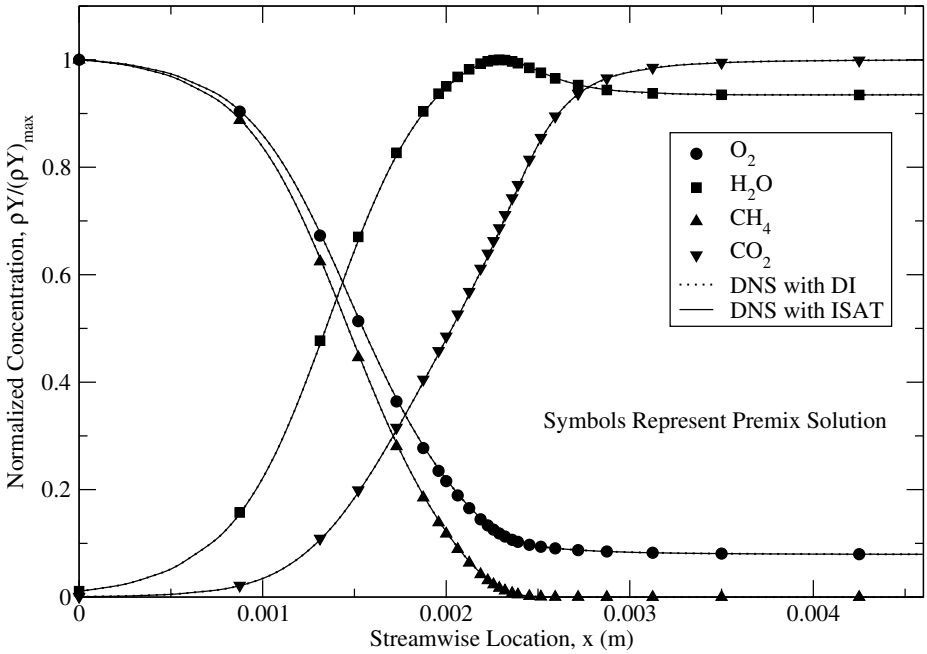

(b) C_k for minor species: H_2, OH, and CO

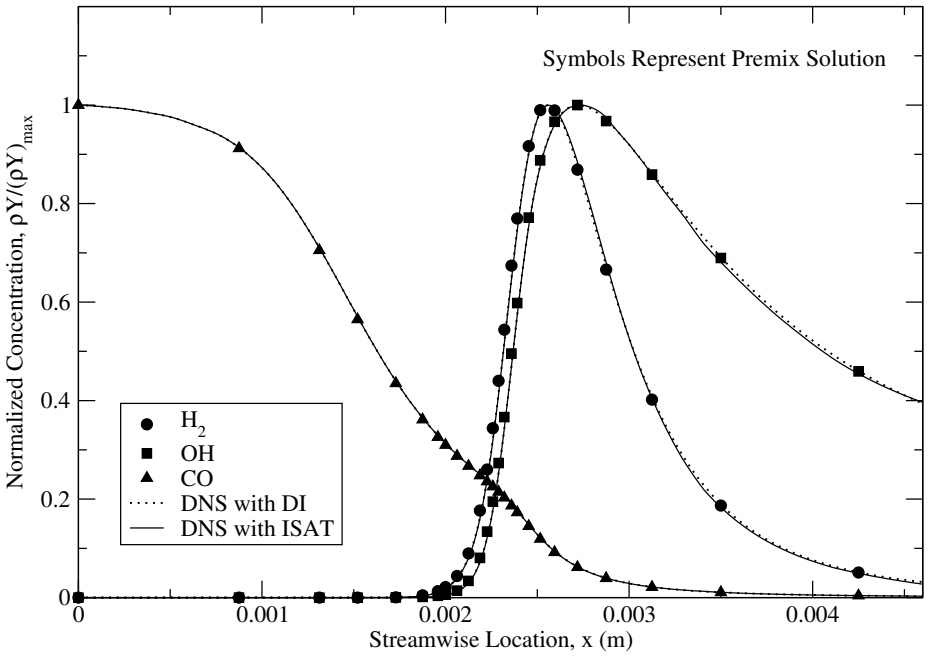

Figure 15: Case 2 normalized concentrations for (a) major and (b) minor species. Reaction rate fluctuations in the DNS/ISAT solution are shown to have a negligible impact on the major species concentrations. Very slight disagreement exists between Premix and DNS/ISAT for the concentration of OH.

(a) RR_k for major species: O_2, H_2O, CH_4, and CO_2

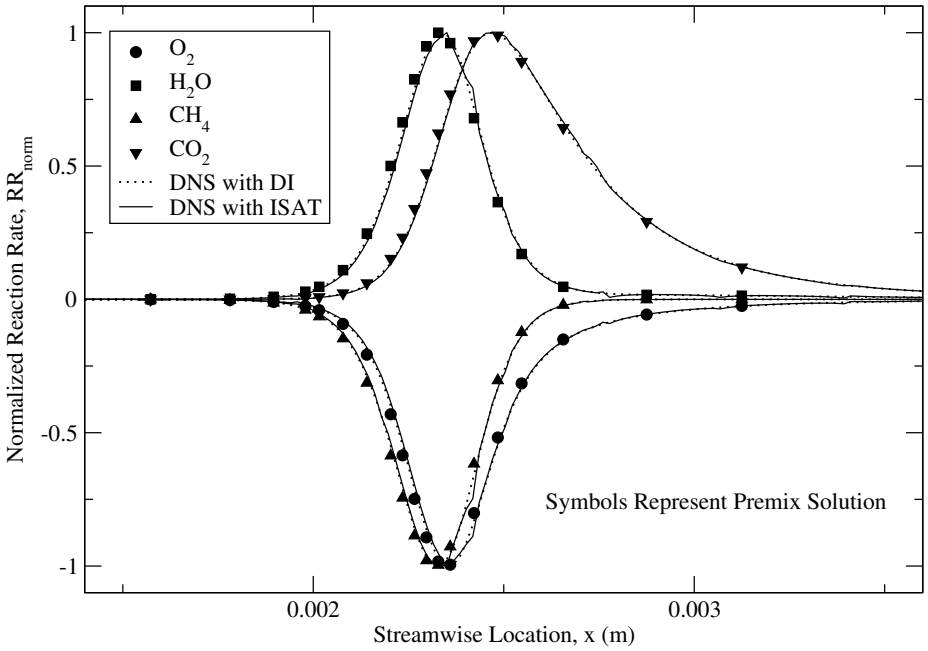

(b) RR_k for minor species: H_2, OH, and CO

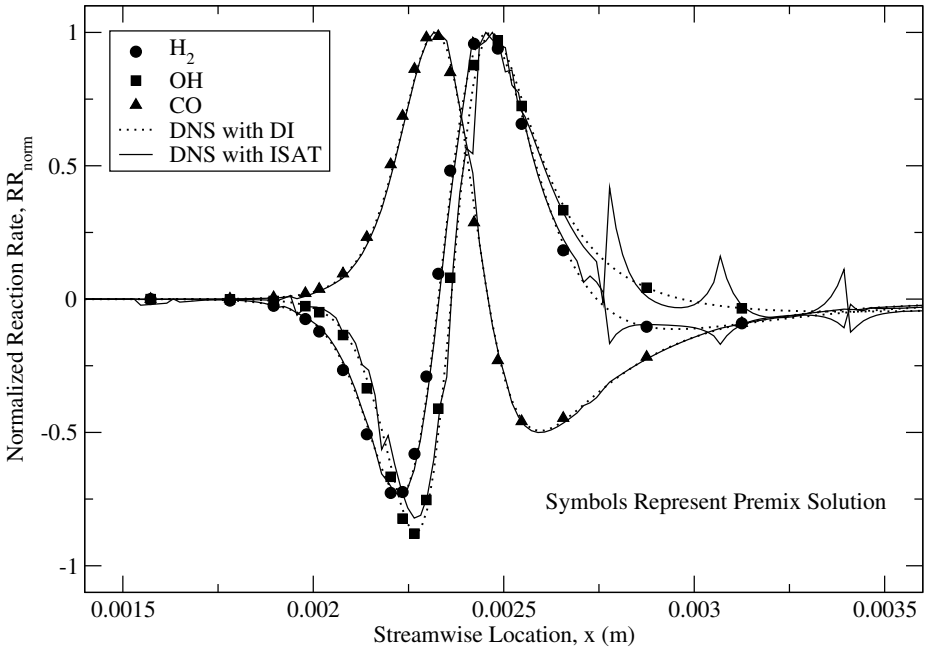

Figure 16: Case 3 normalized concentrations for (a) major and (b) minor species. Major species reaction rates show relatively good agreement, with minor fluctuations in the DNS/ISAT solution. Minor species reaction rates, again, show very large fluctuations throughout the DNS/ISAT solution.

(a) C_k for major species: O_2, H_2O, CH_4, and CO_2

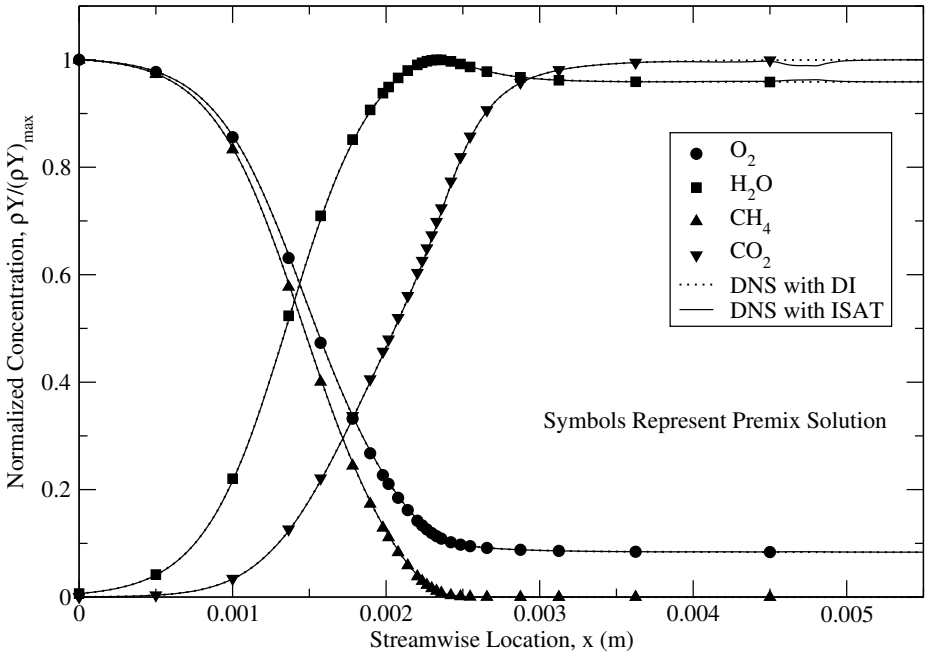

(b) C_k for minor species: H_2, OH, and CO

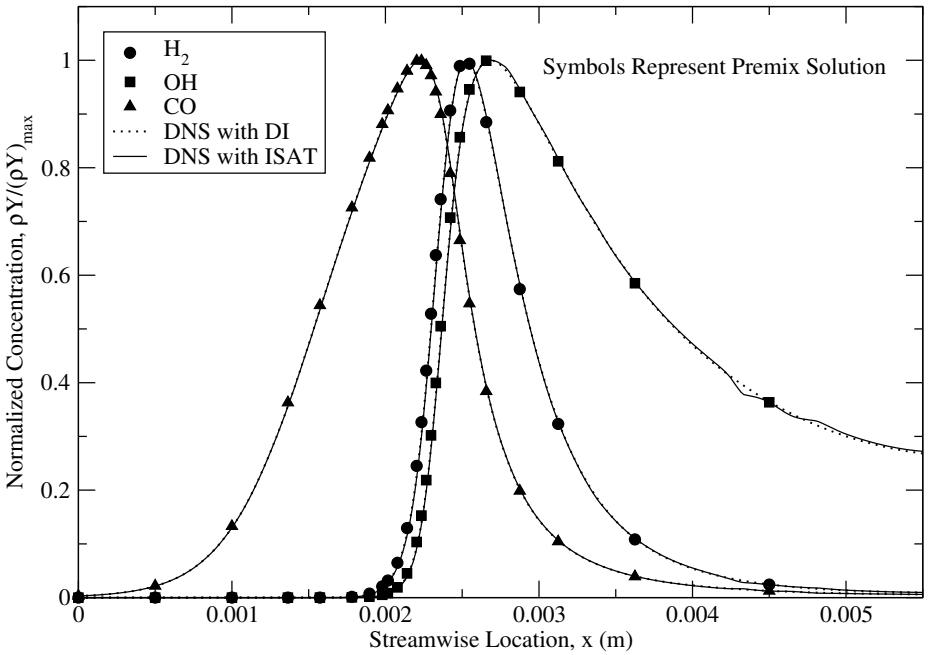

Figure 17: Case 3 normalized concentrations for (a) major and (b) minor species. Agreement between the three solutions is generally good for the major species. Some moderate fluctuations in the DNS/ISAT solution are observed well behind the flame. Minor species are predicted very well for all three solutions.

of the fluctuations is that they occur in species that contribute relatively low concentrations. Simply put, a 20% chemical source variation, coupled with relatively low mass contributions, has a negligible effect on the mass of the system, and the mass fractions in particular. While this is only one hypothesis, it is consistent with all cases, as will be shown later.

The solution to this problem would be a step-by-step error analysis at each stage of the ISAT algorithm, which goes well beyond the scope of this study. For all practical purposes, 20% RR_k variations that produce only slight or negligible C_k variations are completely acceptable.

- ***Case 2 Results:***

The second case provides a slightly greater challenge for the chemical mechanism. The introduction of CO into the reactant stream slightly changes the initial reaction zone anticipated by the reduced mechanism for methane oxidation. Reactions that involve CO are generally slower and take place further downstream. However, the consideration of CO as a fuel changes the dynamics of the problem.

For the major species reaction rates in Fig. 14a, slight fluctuations are observed in the DNS/ISAT solution for all but the primary fuel rate, RR_{CH_4}. The strongest fluctuations are found to be localized around $x = 3.1mm$ for all species, thus demonstrating the interdependence of the chemical source terms on one another. Additional fluctuations are observed for RR_{CO_2} closer to the primary reaction zone. The fluctuations are on the order of those for Case 1, and are much less substantial than the ones occurring further downstream.

Despite showing good overall agreement in major species reaction rates, the solution for DNS/ISAT reveals much larger fluctuations in the minor species rates (Fig. 14b). While the CO reaction rate shows agreement similar to the major species, the RR_{H_2} and RR_{OH} profiles are very erratic near peak production, peak consumption, and in the decaying reactivity zone. Unlike Case 1, the fluctuations are not localized, and peaks as great as 30-35% of the maximum magnitudes are observed. As before, the fluctuations are restricted to the DNS/ISAT solution. The DNS/DI solution continues to show flawless agreement with Premix for all major and minor species reaction rates.

Remarkably, the major species concentrations in Fig. 15a reveal no visible effects of the reaction rate fluctuations. The profiles for DNS/DI, DNS/ISAT, and Premix solutions are essentially identical to one another, even for the distinct, localized rate variation observed in Fig. 14a. Despite the minor species trends in Case 1, agreement between the concentrations for Case 2 is much less likely due to the strong, frequent chemical source fluctuations. However, Fig. 15b reveals that the agreement for all three solutions is excellent. This extends further validity to the hypothesis regarding variations among low concentrations and their overall impact on the system.

- ***Case 3 Results:***

Much like the case of CO addition, Case 3 slightly changes the dynamics of the reaction zone. However, the addition of H_2 to the reactant stream is much less of a challenge, as it tends to react quickly, and in the early stages of the flame.

Unlike Case 2, the major species reaction rates (Fig. 16a) demonstrate excellent agreement for all three solutions. Very small, and apparently localized, deviations are observed for all species around $x = 2.4mm$, but are likely to be of no consequence (judging by the previous results). Reaction rate profiles for the minor species are shown to be quite typical, according to Fig. 16b. The DNS/DI solution exhibits complete agreement with Premix, while the DNS/ISAT solution slightly underpredicts the peak OH consumption and shows consistent fluctuations in the decaying reactivity zone. Peak fluctuations are on the same order as those observed in Case 2.

Strangely, the excellent agreement observed between major species reaction rates does not exactly translate to the concentrations, as shown in Fig. 17a. Through the primary reaction zone, the agreement is excellent. However, in the post-reaction zone, the product species (CO_2 and H_2O) show some inconsistency. Around 4.6 to $4.8mm$, CO_2 shows a slight under-prediction while H_2O shows a slight over-prediction. While unexpected, this slight deviation is still logical, as the two concentrations stored by ISAT balance one another out.

The concentrations of all three minor species show excellent agreement throughout the length of the reaction zone, and even into the post-reaction zone. Only slight deviations,

analogous to those of C_{CO_2} and C_{H_2O}, are visible in the OH concentration of the DNS/ISAT solution. As in the two preceding cases, species concentrations are predicted with substantial accuracy, even in the presence of large chemical source fluctuations.

4.2.2 Working with ISAT

For DNS of laminar flames, implementation of the ISAT algorithm results in computational costs that are, on average, 6.5 times lower than that of a comparable direct integration. However, the achievement of such speedups does not come easily. In CFD applications, ISAT is designed to provide a middle ground for computational efficiency, accuracy, and data storage. The balance between efficiency and storage is based strongly on the level of accuracy used for storing and retrieving the scalar information, which, for this case, consists of the species mass fractions (Y_k, k=1,...,16), the temperature (T), and the computational timestep (Δt). To date, effective levels of accuracy have been achieved primarily through ad hoc methods. Therefore, the discussion provided here is limited to application and personal experience. (Extensive theory and mathematics related to ISAT are provided in publications by Pope [55] and Embouazza et al. [56].)

Despite proven effectiveness, several issues surrounding the implementation and benefit of ISAT still exist. Computational savings vary by problem and, to date, no method has been presented to address consistent cost reduction. There is also concern over the accuracy of the algorthm's predictions, and where the most appropriate intersection between efficiency and precision exists. As observed throughout the current DNS results, ISAT tends to return fluctuating values for minor species chemical source terms, primarily in the low-concentration, post-reaction zone. While these fluctuations are shown to have negligible effects on their respective concentrations, this is not always the case. Strict management of the algorithm and its associated input values is often required to ensure that the magnitude of such fluctuations remains low, thus preventing detrimental effects on the subsequent concentrations.

Although it is regarded as a black box subroutine, the algorithm requires specification of error tolerances and normalization values that effectively define an "ellipsoid of accuracy"

[55]. The specification of these values is most effective when all of the scalar values are normalized to approximately the same degree. For example, the maximum mass fractions of some major species may be two orders of magnitude greater than those of trace species. If the normalizations are not comparable, then the accuracy of retrieved values may be compromised or, in some cases, passed up for a more expensive direct integration step. At the same time, a poor selection of the error tolerance can result in excessive data storage, leading to issues with memory and disk space.

Extensive testing and comparative analysis have yielded an optimized technique that suits the problem at hand quite well. Using a 1-D flame solution from Premix, normalization values for the reactive scalars are calculated as 102% of the maximum species mass fractions and temperature. This provides a range of values that are likely to be experienced throughout the flame, but will effectively remain fractional.

The remaining input for the timestep has proven to be the most important of the set. The algorithm attempts to mimic temporal evolution of scalars, thus requiring accurate information regarding the integration timestep. Judging by the stiffness of the ODE set, a poorly-specified Δt can produce a broad range of reaction rates leading to excessive storage, an overly-large space of acceptable values, and ultimately inaccurate predictions. The rate of storage-and-retrieval will be quite high, however, the accuracy of the simulation suffers greatly. At the same time, if there is no flexibility in the predicted timestep, the stored values become exessively accurate, and the range of acceptable values shrinks. This creates the converse scenario in which values cannot be retrieved and direct integration prevails.

Isolated observation of the timestep input has revealed that the optimal normalization value lies between 2 and 10 times the computational value. In the current flame simulations, the computational timestep, $\approx 0.5 \times 10^{-8}$, has been normalized by values ranging from 0.55×10^{-8} to 0.5×10^{-6} (effectively $1\Delta t$ to $100\Delta t$). At the high end, the simulation is approximately 9 times faster than the comparable direct integration, but it experiences peak reaction rate variations of 15-20% in major species and 50-60% in minor species. At the low end, the predicted scalars are nearly identical to the direct integration, however, the simulation is only 1.2 times faster. At $10\Delta t$ normalization, the interpreted reaction rates

are consistently within 1% of the analogous direct integration values, and the simulation is, on average, 6-7 times faster than a direct integration.

The technique used in the current simulations consistently produces the aforementioned speedups for short-term computations in which stationary laminar flames are computed to an approximate steady state. For most cases, the retrieval frequency is non-linear, and is based heavily on the dynamics of the problem. For a laminar flame taken to steady state, the temporal retrieval profile starts out at zero and is followed by a short period of low retrieval and frequent direct integration. Shortly thereafter, the profile experiences a sharp increase to around 85-90% retrieval, followed by a very gradual ascent to the peak value, usually between 95 and 99%. This range is deemed acceptable, as only a perfectly steady-state solution is capable of reaching 100% retrieval.

The computational speedup, $\mathscr{S}$, can be loosely approximated by the equation

$$\mathscr{S} = \frac{cost_{DI}}{cost_{ISAT}} = \frac{t_{flow} + t_{chem}}{t_{flow} + (1 - \mathscr{R})\, t_{chem}} \ , \tag{65}$$

where t_{flow} is the time fraction dedicated to flow computation, t_{chem} is the time fraction dedicated to chemistry computation during direct integration, and $\mathscr{R}$ is the average retrieval percentage of ISAT. Typically, the ratio of t_{flow} to t_{chem} is a known characteristic of the DNS code. However, if this ratio is not known, it can be determined by obtaining $\mathscr{S}$ from separate DNS/DI and DNS/ISAT simulations.

Equation 65 can be rewritten in the form

$$\frac{t_{flow}}{t_{chem}} = \frac{1 - \mathscr{S}(1 - \mathscr{R})}{\mathscr{S} - 1} \tag{66}$$

to determine the characteristic time fractions for flow and chemistry. As an example, the current DNS code has a speedup of 6.5 at an average ISAT retrieval of 95%. Using Eqn. 66, this results in the following flow-to-chemistry ratio:

$$\frac{t_{flow}}{t_{chem}} = \frac{1 - 6.5(1 - 0.95)}{6.5 - 1} \approx 0.1227 \ . \tag{67}$$

From simple mathematical reduction, the fraction of time dedicated to flow computation is approximately 11%, making the fraction dedicated to chemistry 89%. This further illustrates the substantial cost of chemistry computation and the importance of efficiency algorithms like ISAT.

4.2.3 Working with Multicomponent Transport

The basic principles of the multicomponent transport implementation have been covered in Chapter 2. In that chapter, an alternative (and less-accurate) technique for the specification of transport properties was also discussed. The use of fixed, dimensionless parameters is very common practice in numerical simulations as it provides a relatively simple and cost-effective way to address variables related to heat and mass diffusion. However, the dependence of such variables on temperature, pressure, and mixture composition presents concerns regarding physical accuracy. To date, accuracy has not been sufficiently addressed.

In order to perform a valid 1-to-1 comparison between Premix and the DNS code, the two must use the same physical models. The computation of thermodynamic and transport properties must, therefore, be performed in the same fashion. For this reason, the DNS code has been directly linked to the transport subroutine library in Chemkin-II. In doing so, the same multicomponent transport formulations are employed for both codes, and dynamic transport properties can be computed in the DNS.

As mentioned in this chapter, earlier versions of the DNS code have the capability to reproduce primitive variables in a short-term simulation, even when the chemical source terms are poorly-predicted. In time, however, the inconsistency between the initialized flame and the computed source terms causes the flame to migrate towards a new steady-state solution, consistent with the fixed-transport conditions. This is best illustrated by Fig. 18, which shows flow variable (T and ρ) and reaction rate (scaled $\dot{w}_{H_2}$ and $\dot{w}_{CO}$) profiles for a short-term computation of the Case 1 flame using fixed-transport and dynamic,

multicomponent transport.

In Fig. 18a, the temperature and density profiles of the two solutions are shown to be in excellent agreement. However, the reaction rate profiles in Fig. 18b reveal that the reaction zone thickness for fast-reacting (H_2) and slow-reacting (CO) species are very poorly predicted. Additionally, the reaction rate magnitudes are not consistent between the two solutions. This immediately demonstrates that, in a steady-state simulation, the fixed-transport flame cannot possibly sustain its initial structure as the reaction zone is already broadened in the streamwise direction.

In Sec. 4.2.1, the dynamic, multicomponent transport has already been shown to correct this problem. The DNS code is fully capable of reproducing a steady-state flame solution from Premix, and maintaining that solution over time. However, most solutions are generally accompanied by an additional cost, and multicomponent transport is no different. The multicomponent formulation requries the passing of information between an extensive library of subroutines. When coupled with the added mathematical operations (including expensive matrix inversions), the net cost is approximately 15 to 20% greater than the original fixed-transport simulation. While it is possible to link the transport computations to ISAT, it has not been attempted in this study, and the additional cost of the multicomponent computation must be shouldered.

Despite its notable expense, this technique is shown to have a very good impact on the flexibility of the code, and the accuracy of the flame simulation. Although the tradeoff is problem-specific, the accurate simulation of unsteady flames (such as the flame-vortex interaction) must begin with the accurate simulation of steady flames.

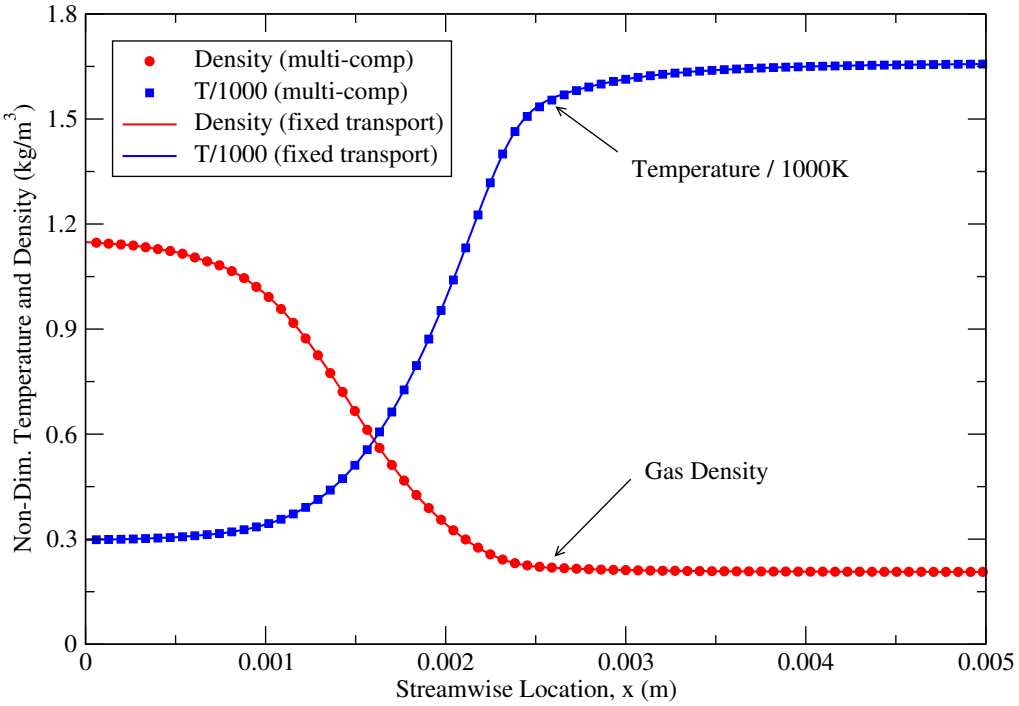

(a)

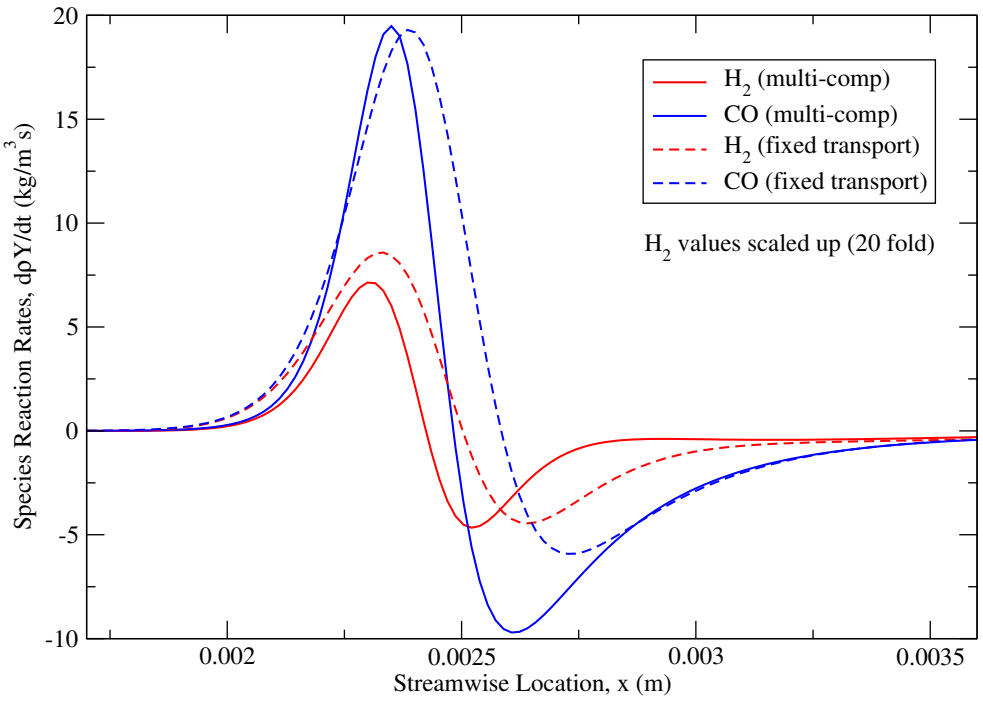

(b)

Figure 18: Demonstration of fixed transport versus multicomponent transport for short-term simulation of the Case 1 flame. (a) Non-dimensional temperature ($T/1000K$) and density show very good agreement, while (b) the CO and scaled H_2 ($20 \times \dot{w}_{H_2}$) reaction rates show substantial disagreement.

CHAPTER V

RESULTS AND DISCUSSION

This chapter examines the 2-D flame-vortex interactions upon which this study is based. Validation of the DNS code is performed using pure CH_4/Air flames over a specific set of vortex conditions. These conditions are then extended to the $CH_4/CO/Air$ and $CH_4/H_2/Air$ flames to address the effects of multicomponent fuel mixtures on stretched flame fronts.

5.1 DNS of Flame-Vortex Interaction

The flame-vortex DNS validation is performed by three separate simulations. The Case 1 (pure methane) flame is simulated using three vortex configurations, adapted from Mueller et al. [1]. As discussed in Sec. 1.3.2, that particular study by Mueller et al. dealt with vorticity generation and attenuation in experimental flame-vortex interactions, using lean propane-air mixtures ($\phi = 0.585$, $\delta_f = 1.6\ mm$, $S_L = 9.7\ cm/s$). While discrepancies exist between the experiment and the simulation (e.g. fuel type, adiabatic flame simulation, etc.) the goal is to obtain a good qualitative comparison between the two.

The conditions of the experimental study and the current simulations are given in Table 1. In each of the three experimental cases, the incident vortex was issued with a different strength, representing *weak* ($U_\theta/S_L = 1.4$), *intermediate* ($U_\theta/S_L = 3.6$), and *strong* ($U_\theta/S_L = 10.1$) vortices. To facilitate this, the sizes of the vortices were also varied between $d_c/\delta_f = 3.0$ and 4.6, where d_c is the vortex core diameter and δ_f is the flame thermal thickness. The authors noted that vortices of this size are representative of eddies that are large enough to wrinkle a turbulent flame [1]. For simplicity, a single vortex size is chosen for the simulations. The average vortex size $d_c/\delta_f = 3.8$ is used for the simulation of weak, intermediate, and strong vortices, with U_θ/S_L conditions of 3.6, 6.8, and 10.1, respectively.

Maximum vorticty values of the incident vortices are listed in Tab. 1. The local vorticity values are computed from the curl of the velocity vector, according to

Table 1: Vortex conditions for the flame-vortex validation study. Conditions are listed for the referenced experimental study (Mueller et al. [1]) and the current simulations. Experimental flame is propane-air ($\phi = 0.585,\ \delta_f = 1.6\ mm,\ S_L = 9.7\ cm/s$) and simulated flame is methane-air ($\phi = 0.6,\ \delta_f = 1.5\ mm,\ S_L = 11\ cm/s$).

Vortex Type	Exper. d_c/δ_F	Exper. U_θ/S_L	Simul. d_c/δ_F	Simul. U_θ/S_L	Simul. peak $\lvert\omega_z^0\rvert$
weak	4.6	1.4	3.8	3.6	1055 s^{-1}
intermediate	3.8	3.6	3.8	6.8	2024 s^{-1}
strong	3.0	10.1	3.8	10.1	2987 s^{-1}

$$\vec{\omega} = \nabla \times \vec{u} \tag{68a}$$

$$\omega_z = \frac{\partial v}{\partial x} - \frac{\partial u}{\partial y} \tag{68b}$$

where the gradients in the two-dimensional vorticity equation (68b) are computed using a fourth-order central differencing scheme [41]. For uniform grids, the differencing formulations for these gradients are given by

$$\frac{\partial v}{\partial x} = \frac{(v_{i-2,j,k} - v_{i+2,j,k}) + 8\,(v_{i+1,j,k} - v_{i-1,j,k})}{12\,(x_{i,j,k} - x_{i-1,j,k})} \tag{69a}$$

$$\frac{\partial u}{\partial y} = \frac{(u_{i,j-2,k} - u_{i,j+2,k}) + 8\,(u_{i,j+1,k} - u_{i,j-1,k})}{12\,(y_{i,j,k} - y_{i,j-1,k})}\ . \tag{69b}$$

5.1.1 Weak-Vortex Simulation

The selection of this particular vortex as the *weak* case is the result of initial observations. As shown in Fig. 19, the incident vortex begins to break down due to gas expansion in the negatively curved region of the flame (heat focuses inward). In this study, one of the key features is *vorticity attenuation*, which refers to the reduction of peak vorticity magnitude over time. At 16 ms (Fig. 19d), over 60% of the incident vortex has been attenuated, and by 22 ms (Fig. 19e), the incident vortex is completely attenuated, leaving behind an elongated region of slow-moving reactants.

(a) $t = 0.0\ ms$, $\omega_z^{max} = \omega_z^0$

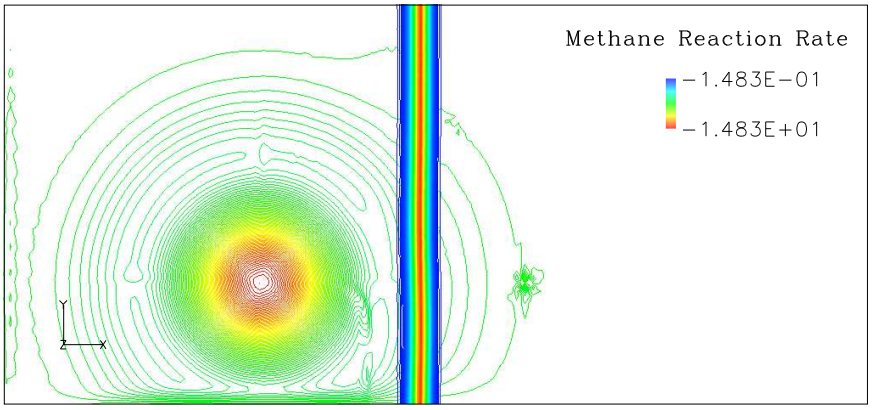

(b) $t = 5.34\ ms$, $\omega_z^{max} = 0.81 \times \omega_z^0$

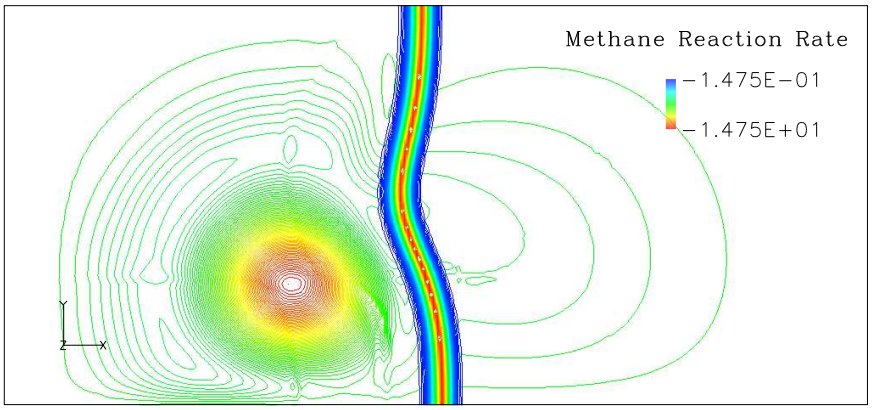

(c) $t = 10.67\ ms$, $\omega_z^{max} = 0.64 \times \omega_z^0$

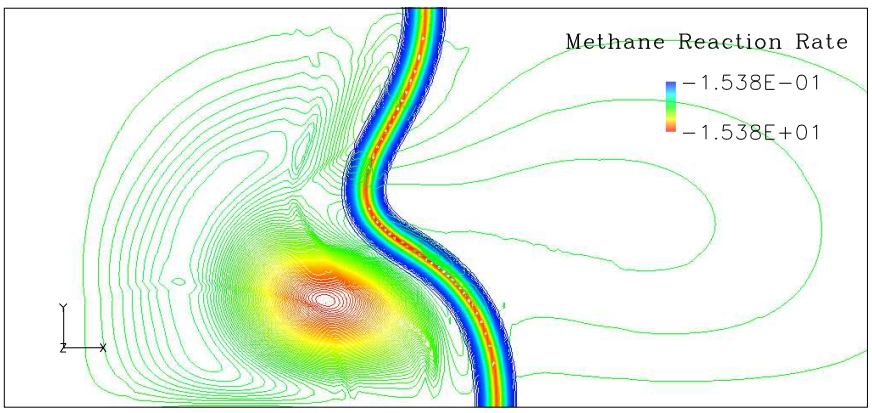

Figure 19: Flow visualization of the interaction between the Case 1 flame and a **weak** vortex. Snapshot times for frames (a)-(f) are displayed above the respective figures, along with the current vortex strength. The flame surface is represented by CH_4 reaction rate contours. Important observations include complete attenuation of the incident vortex, small pocket formation, and flame-generated vorticity (FGV).

(d) $t = 16.00\ ms$, $\omega_z^{max} = 0.37 \times \omega_z^0$

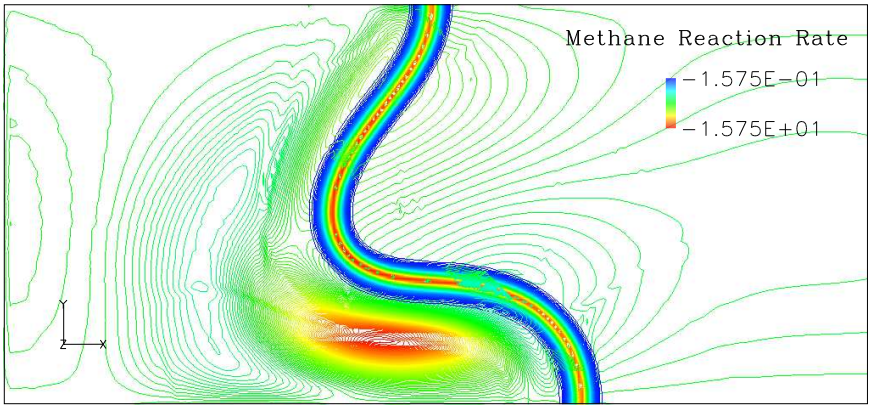

(e) $t = 21.32\ ms$, $\omega_z^{max} = -0.15 \times \omega_z^0$ (FGV)

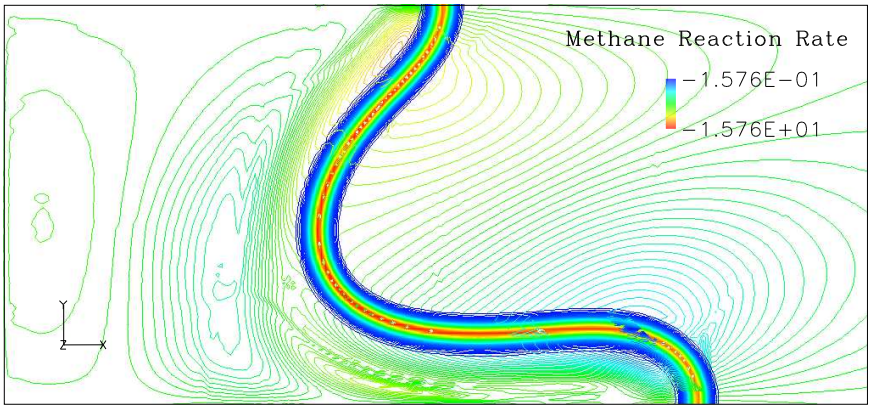

(f) $t = 25.89\ ms$, $\omega_z^{max} = -0.19 \times \omega_z^0$ (FGV)

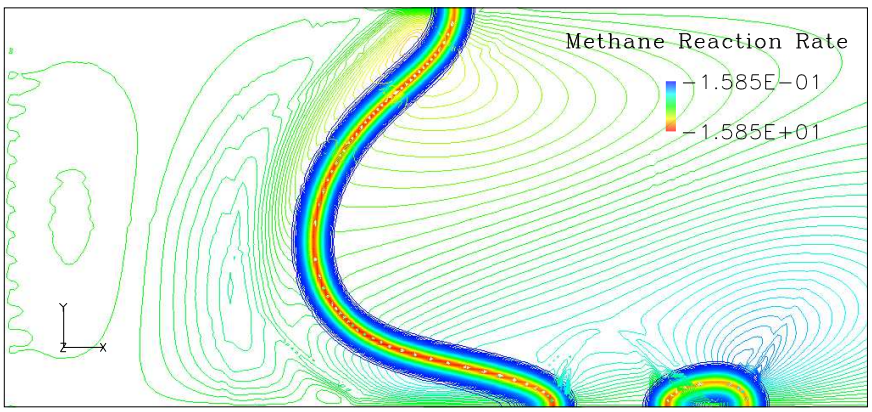

Fig. 19 *(Continued)*

As the incident vortex is consumed, there is also evidence of flame-generated vorticity (FGV) in the vicinity of its former location. This FGV opposes the rotation of the incident vortex and is on the order of 15-20% of the initial vorticity. Shortly after the vortex is attenuated, the stretched flame begins to consume the remaining reactant mixture in its path, and eventually collapses on itself around 25 ms. In Fig. 19f, the flame is shown to pinch off, and a small pocket of reactants breaks away from the primary flame surface, later to be consumed.

The methane reaction rate contours in Fig. 19 are consistent with experiments and theory of curved, diffusionally unstable flames. The positively-curved segments of the flame experience fuel reaction rates ($\dot{w}_{CH_4}$) that exceed the unstretched value, while the negatively-curved segments are typically at or below the unstretched value. This demonstrates the effect of preferential diffusion (from Sec. 1.2.3) for cases in which mass diffusion exceeds thermal diffusion ($Le < 1$). According to the observed trends, positively-curved surfaces become increasingly stoichiometric, (more reactive) and negatively-curved surfaces become increasingly lean (less reactive). This agrees with observations made by Mizomoto et al. [13] and Law et al. [14].

5.1.2 Intermediate-Vortex Simulation

Considering the preceding results for the weak vortex, it is clear that a stronger vortex is required to stretch the flame surface and not be destroyed. However, due to the nature of the physical model, it is difficult to predict exactly how strong the vortex must be in order to achieve this. The intermediate-strength vortex simulation adopts an average strength from Mueller et al.'s intermediate and strong vortices.

With an increased rotational velocity, U_θ, the intermediate vortex convects much faster than the weak vortex, and requires less physical and simulation time. While the weak vortex is essentially attenuated prior to pocket formation (at $t \approx 25\ ms$), Fig. 20 indicates that the intermediate vortex is strong enough to generate a "bubble" in the flame surface and survive through the pocket formation ($t \approx 18\ ms$).

Unlike the weak vortex, the intermediate vortex is capable of resisting substantial gas

(a) $t = 0.0\ ms$, $\omega_z^{max} = \omega_z^0$

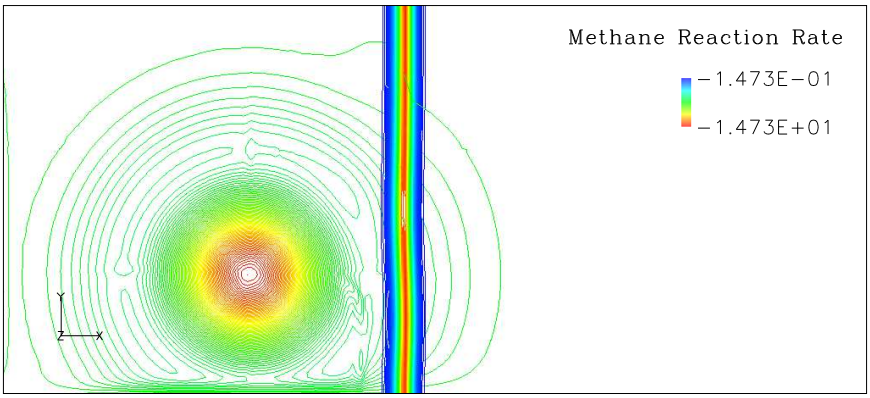

(b) $t = 3.74\ ms$, $\omega_z^{max} = 0.87 \times \omega_z^0$

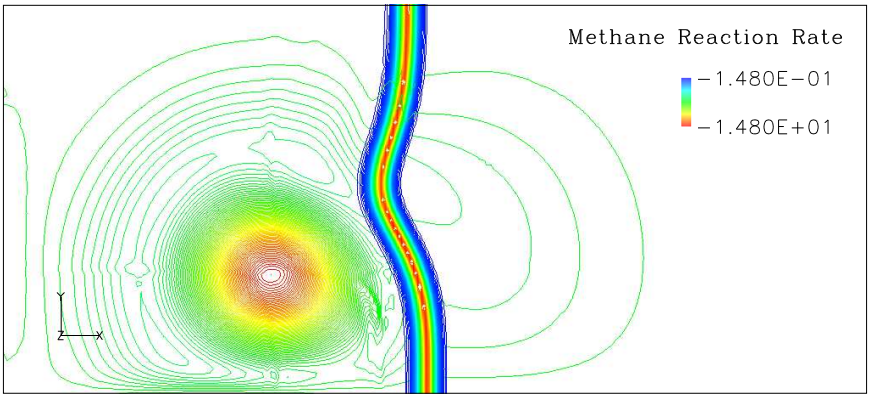

(c) $t = 7.47\ ms$, $\omega_z^{max} = 0.74 \times \omega_z^0$

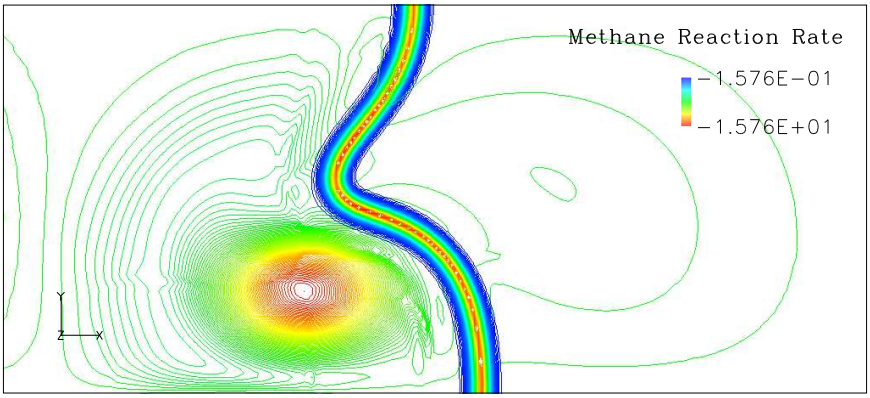

Figure 20: Flow visualization of the interaction between the Case 1 flame and an **intermediate** vortex. The time of each snapshot, and the maximum vortex strength are displayed above each figure. Again, the flame surface is represented by CH_4 reaction rate contours. Important observations include 85% attenuation of the incident vortex, formation of a larger pocket around the vortex, and minor (FGV).

(d) $t = 11.19\ ms$, $\omega_z^{max} = 0.57 \times \omega_z^0$

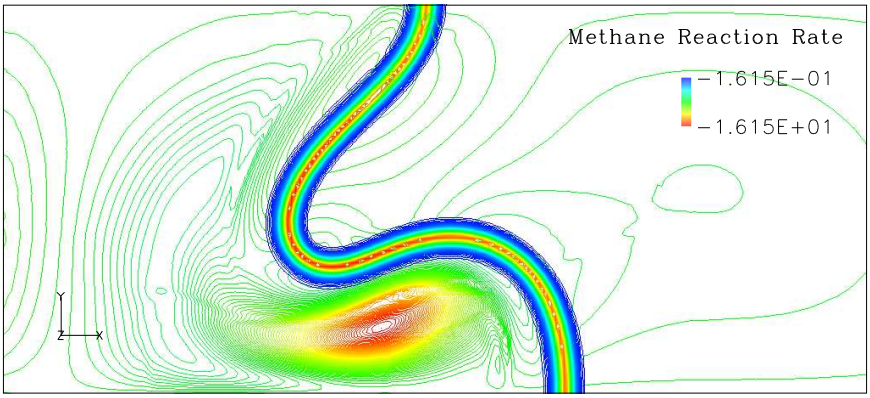

(e) $t = 14.92\ ms$, $\omega_z^{max} = 0.31 \times \omega_z^0$

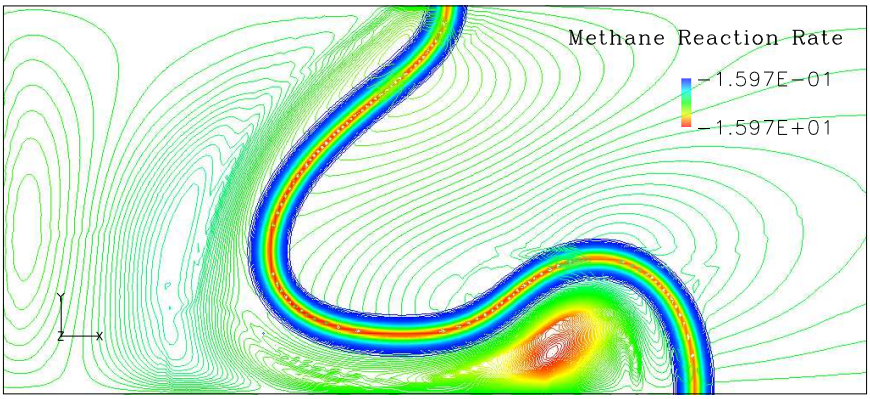

(f) $t = 18.64\ ms$, $\omega_z^{max} = 0.16 \times \omega_z^0$

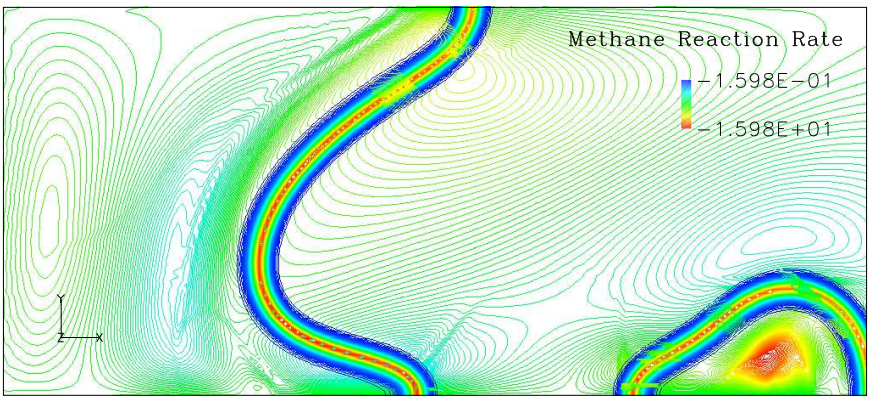

Fig. 20 *(Continued)*

expansion, which results in the formation of a larger pocket. Just prior to pinching off, at around 15 ms (Fig. 20e), the incident vortex is approximately 70% attenuated. However, in this case, the rotational flow contributes to the pinch-off by forcing heat transfer into the reactants and accelerating motion of the flame surface towards itself. In the final frame of Fig. 20, the flame has pinched off and the incident vortex remains at around 16% of its original strength.

The CH_4 reaction rate trends along the flame surface are similar to those of the weak vortex case. Burning rates among positive and negative curvature demonstrate the same relative behavior as before. The large, negatively-curved segment of the flame consumes methane at approximately 93-95% of the unstretched rate, while the positively-curved segment experiences methane comsumption as great as 110% of the unstretched value. As shown in Fig. 20d, the strongest burning rates occur around $t = 11.2\ ms$ where the positive curvature is very strong. Similarly, the weakest burning occurs around $t = 14.9\ ms$ where negative curvature is large (Fig. 20e).

While a degree of FGV exists, its presence is not apparent. The magnitude of FGV in the weak vortex case was subtantial due to the lower initial vortex strength. However, for the intermediate vortex, the FGV magnitude is on the order of 3-5% the incident value, and does not have any discernible effect on the flame structure.

5.1.3 Strong-Vortex Simulation

The strong-vortex simulation is quite similar to the intermediate-vortex simulation. The vortex and flame behavior are qualitatively the same. Again, the physical time required for the flame-vortex interaction to evolve is reduced due to the greater convective velocity of the vortex. Where the intermediate case pinches off around 18 ms, the strong-vortex case pinches off around 14 ms.

As shown in the previous case, stronger vortices are able to resist attenuation related to gas expansion and baroclinic effects. This is more apparent in the strong-vortex case. The "bubble" formed in the intermediate case (Fig. 20e) is smooth and gradual due to elongation of the vortex. In the strong case (Fig. 21e), the "bubble" is much more pronounced and the

(a) $t = 0.0\ ms$, $\omega_z^{max} = \omega_z^0$

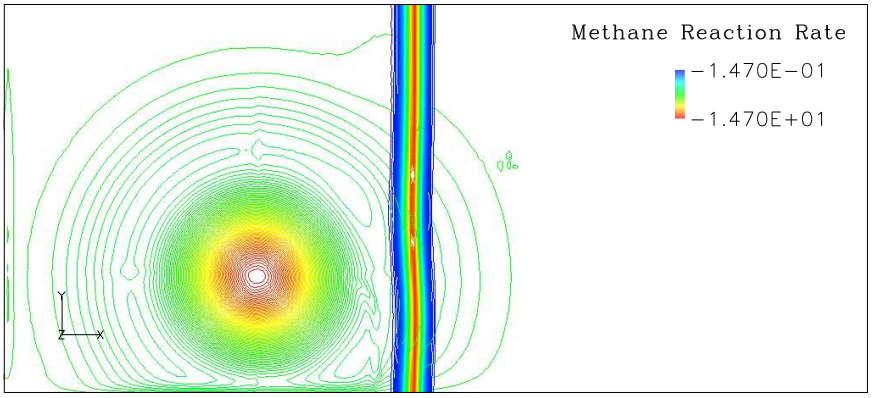

(b) $t = 3.20\ ms$, $\omega_z^{max} = 0.89 \times \omega_z^0$

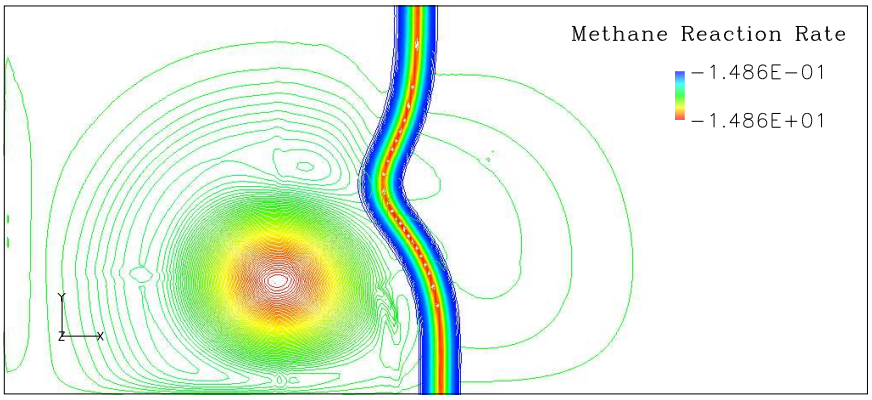

(c) $t = 5.87\ ms$, $\omega_z^{max} = 0.79 \times \omega_z^0$

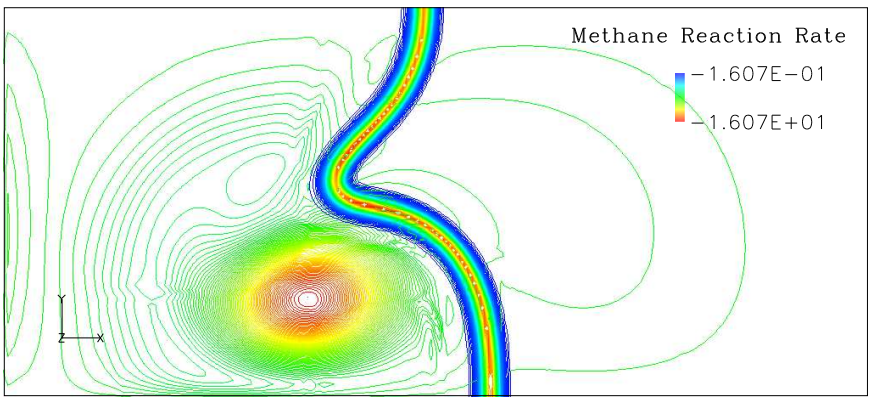

Figure 21: Flow visualization of the interaction between the Case 1 flame and a **strong** vortex. The time of each snapshot, and the maximum vortex strength are, again, displayed above each figure. The flame surface is represented by CH_4 reaction rate contours. Only 59% attenuation of the incident vortex is observed leading to the formation of a very large pocket around the vortex. No significant FGV is observed.

(d) $t = 8.53\ ms$, $\omega_z^{max} = 0.70 \times \omega_z^0$

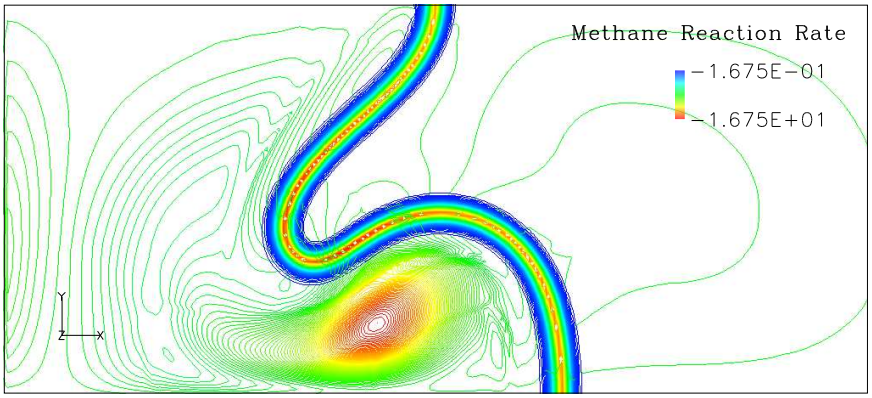

(e) $t = 11.19\ ms$, $\omega_z^{max} = 0.59 \times \omega_z^0$

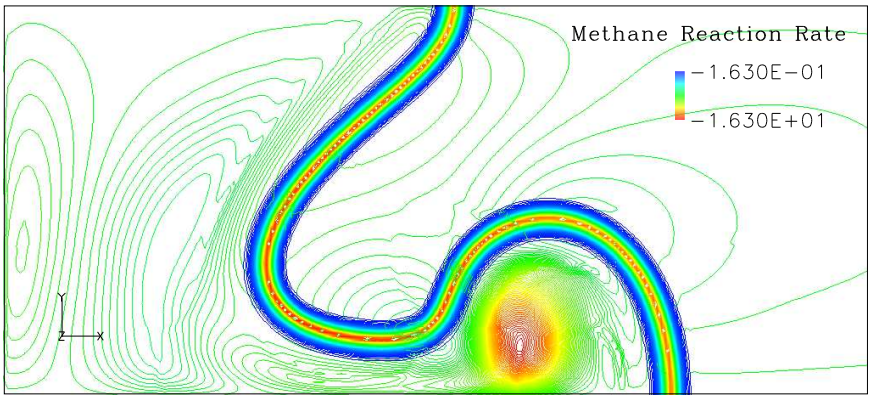

(f) $t = 14.38\ ms$, $\omega_z^{max} = 0.41 \times \omega_z^0$

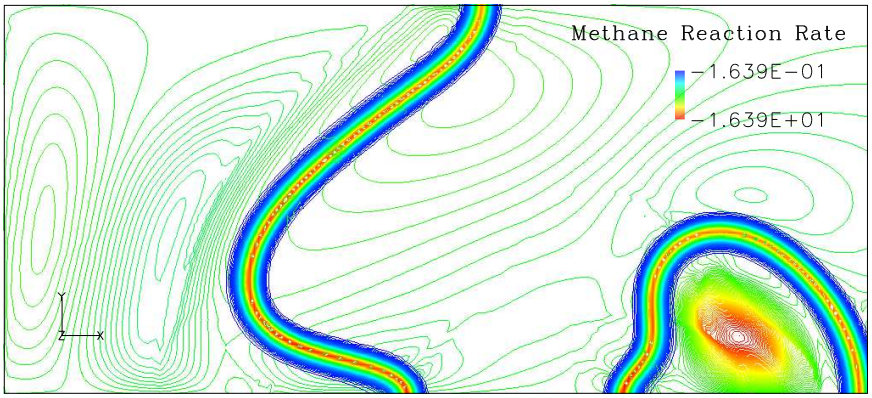

Fig. 21 *(Continued)*

incident vortex is not nearly as elongated. Prior to pinching off, the strong vortex maintains approximately 55-60% of its initial strength, whereas the intermediate vortex maintains only 25-30%. After pinching off, the vortex carries the pocket with approximately 41% of its initial strength. FGV is not apparent in this case, primarily due to the strength of the surviving incident vortex.

The strong vortex also produces greater curvature of the flame surface. This results in a broader range of burning rates along the flame surface. At $t = 8.5\ ms$ (Fig. 21d), the large, positive curvature results in CH_4 consumption rates that are 15% greater than the unstretched value. Along the negatively-curved segment of the flame, in Fig. 21e, methane is consumed at around 95% of the unstretched rate. The constant availability of reactant CH_4 diminishes the effects of preferential diffusion in the region of negative curvature, while enhancing the effects among positive curvature.

5.1.4 Simulation vs. Experiment

The three simulations performed in this validation study show qualitative characteristics that are similar to those observed in the experimental studies performed by Mueller et al. [1]. The methane-air flame used in the simulations is slightly more robust than the propane-air flame used for the experiments (i.e.higher S_L, lower δ_F). Similarly, the dynamics of stretched propane-air and methane-air flames are notably different. Based on these two facts, it is reasonable to expect that the simulations and experiments will not be identical to one another.

The results of the experimental and numerical studies are given in Table 2. A vorticity attenuation parameter, Ω, has been defined by

$$\Omega = 1 - \frac{\omega_z^p}{\omega_z^0}\ , \tag{70}$$

where ω_z^0 is the initial value, and ω_z^p is the value taken shortly after the flame has pinched off (between the (e) and (f) frames in Figs. 19-21). Beyond this point, the dynamics of the problem change as the primary flame surface returns to its planar structure and the

Table 2: Experimental [1] and simulated results for the flame-vortex validation. Vortex parameters corresponding to weak, intermediate, and strong vortices are given in Table 1. ($*$ *denotes observed flame quenching*)

Vortex Type	Experiment Ω	Simulation Ω
weak	2.0	1.17
intermediate	0.8	0.83
strong	0.0*	0.54

pocket consumes itself. A value of $\Omega = 1$ indicates that the incident vortex is completely attenuated, $\Omega = 0$ indicates negligible attenuation, and $\Omega > 1$ indicates that significant counter-rotating vorticity (FGV) is generated.

As evident from Tab. 2, the simulation and experimental data on vorticity attenuation is not identical. However, the key observations are the same over the respective sequences of vortex strengths.

For the weak-vortex simulation, the incident vortex is completely destroyed as it attempts to cross the flame. In stretching the flame surface, significant FGV is produced by the baroclinic torque (as was observed during the weak-vortex experiments). Elongation of the vortex core due to gas expansion is observed in both cases, and regarded as the primary cause of attenuation.

The intermediate-vortex simulation also experiences a great deal of peak vorticity attenuation. As in its experimental counterpart, the incident vortex is strong enough and fast enough to resist excessive gas expansion, allowing it to survive interaction with the flame. Although the majority of the incident vorticity magnitude is dissipated, enough strength remains to carry the pocket of reactants and produce a slight amount of FGV.

The largest - and possibly the most-logical - discrepancy exists among the strong-vortex interactions. In the experimental case, quenching of the flame is observed at the leading edge of the vortex toroid. This allows the vortices to pass through the flame while experiencing negigible elongation and peak vorticity attenuation. Although quenching is not entirely feasible under the conditions of the simulation, the strong-vortex case experiences

a lower degree of attenuation. No significant FGV is observed in either case, and where the experimental vortex was completely unaffected, the simulated vortex did, in fact, maintain a majority of its incident strength prior to flame pinch-off.

Citing specific differences between each case, a 1-to-1 comparison of the three vortex configurations is inconclusive. However, the trends that are observed for each sequence are conclusive. The primary observation is that an increase in initial vortex strength results in lower attenuation. While such an observation may appear to be quite simple, and simultaneously inane, that is exactly the point. Weak vortices do not survive flame passage, but produce new, counter-rotating vorticity. Intermediate and strong vortices are robust enough to resist the major destructive forces, and inhibit the production of flame-generated vorticity. Their relationship is fundamental.

The logical explanation of stronger vortices surviving longer would appear to be sufficient. At the same time, many other factors can come into play. For instance, the residence time of the vortex will have a direct impact on the viscous dissipation in the vorticity transport equation 5. Furthermore, stronger vortices convect faster, have lower residence times, dissipate less energy (over a comparable distance), and maintain a stronger core, thus resisting gas expansion.

5.2 Analysis of Flame Stretch

Thus far, the theoretical discussion of flame stretch has focused on the existence of two contributing factors: strain and curvature. When considered independently, the two may demonstrate different behavior over a common segment of the flame. Therefore, in this study, they are examined as entirely separate entities.

The strain and curvature components of stretch (K_s and K_c, respectively) are represented mathematically by

$$K_s = \nabla_t \cdot \vec{u} \tag{71a}$$

$$K_c = S_d \left(\nabla \cdot \vec{n}\right) \ . \tag{71b}$$

These forms are useful when analyzing continuous functions. However, in a discretized flowfield, information is only available at prescribed locations. Therefore, information at the flame location must be extrapolated from adjacent cells, similar to the cell-face fluxes in the finite-volume scheme. For the current 2-D analysis, the components in Eqn. 71 are more useful when rewritten in the following index form:

$$K_s = (\delta_{ij} - n_i n_j) \frac{\partial u_i}{\partial x_j} \tag{72a}$$

$$K_c = S_d \frac{\partial n_i}{\partial x_i} \ . \tag{72b}$$

Considering that the DNS solution is not defined by a set of continuous functions, the local velocity gradients must be computed with the aid of a numerical scheme. To achieve this, a fourth-order central differencing scheme, identical to that used for the vorticity computation (Eqn. 69), is employed at all discrete locations in the field.

In Eqn. 72, both stretch components are shown to be functions of the flame surface-normal vector, $\vec{n} \equiv (n_i,\ n_j)$. In order to derive the surface-normal, a characteristic isosurface must be chosen to represent the flame. One common technique for specifying the flame surface is to compute a local *progress variable*, c_f, that is continuous throughout the flame. In cases where most (if not all) of the fuel is consumed, the progress variable can be specified at all discrete points by

$$c_f = 1 - \frac{Y_f^{loc}}{Y_f^{unb}} \ . \tag{73}$$

Here, the flame is defined by a single isosurface, c_f, which represents a particular level of fuel consumption. The value Y_f^{unb} is the unburned fuel mass fraction inside the cold reactant stream, and Y_f^{loc} is the local value of the fuel mass fraction inside the flame zone. In comparing flames with different compositions, c_f is a more useful parameter than Y_f^{loc}, as it is not mixture-dependent.

The progress variable defines exactly what its name implies: progress of a specific variable. In this case, it is the progress of the fuel mass consumption. When the local value, Y_f^{loc}, is at 20% of the unburned value, the progress variable is 0.8 (i.e. 80% progress). Such a technique is quite effective, as the locations of fuel isosurfaces are typically consistent through the flame. This is true for most cases, with the exception of those where extreme variations in fuel reaction rates are observed along the flame (e.g. near-quenching, extremely high curvature, etc.).

The precise value of c_f rarely exists at any discrete point in the field, and is typically located somewhere between grid points. To clearly define the characteristic isosurface, an algorithm sweeps the entire domain and locates pairs of gridpoints where the progress variable transitions from c_f^- to c_f^+. Based on the relative magnitudes of c_f^- and c_f^+, an interpolation is performed, and a new flame-surface point, corresponding to c_f, is recorded. All subsequent computations (such as $\partial u_i/\partial x_j$ and S_d) are performed at the new set of points defining the flame surface.

After the characteristic flame isosurface has been defined, the flame surface-normal computation is fairly straightforward. Since the surface-normal is a unit vector, it can be broken down into more-useful orthogonal components. In generalized index form, the 2-D unit normal is represented by

$$\vec{n} = \frac{\nabla c_f}{|\nabla c_f|} = (n_i,\ n_j) = \left(\frac{\partial c_f}{\partial x_i} \sqrt{\left(\frac{\partial c_f}{\partial x_k}\right)^2}\ ,\ \frac{\partial c_f}{\partial x_j} \sqrt{\left(\frac{\partial c_f}{\partial x_k}\right)^2} \right) \ \ldots \ k = i, j \qquad (74)$$

The only remaining term in the flame stretch equations is the displacement speed, S_d. As mentioned in Chapter 1, the definition and formulation of a displacement speed are often difficult tasks, and are rarely universal. More so than not, the value of S_d is an artifact of the other three dependent variables (K, K_s, and K_c/S_d). However, some numerical formulations have been proposed to handle the computation of S_d. For the current flame stretch analysis, the strain rate and surface curvature are examined separately, and independent of the displacement speed. However, a comparative analysis of two separate S_d formulations is provided later in this chapter.

Table 3: Parameters of the six flame-vortex cases used to study the effects of *syngas*. All incident vortices are the same size, relative to their flame thicknesses, and both weak and strong rotation are represented.

Case ID	Fuel Type (by % Volume)	Vortex Size d_c/δ_F	Vortex Strength U_θ/S_L
1W	100% CH_4	3.8	3.6
1S	"	3.8	10.1
2W	70/30% CH_4/CO	3.8	3.6
2S	"	3.8	10.1
3W	70/30% CH_4/H_2	3.8	3.6
3S	"	3.8	10.1

5.3 Effects of Syngas on Stretched Flames

The simulation of stretched flames in multicomponent-fuel mixtures is performed using the strong and weak vortex configurations employed in the preceding flame-vortex validation. The mixtures selected for the 1-D DNS validation (Sec. 4.2) are used here to produce three different laminar flames with matching flame speed, heat release, and flame thickness. This produces a total of six simulations upon which qualitative and quantitative comparisons are performed.

The simulations for the Case 1 flame (pure CH_4) have already been performed for the strong and weak vortex configurations. From this point forward, these cases are referred to as Case 1S (strong vortex) and Case 1W (weak vortex), respectively. This naming convention is adopted for the additional four simulations involving the addition of CO (Cases 2S and 2W), and H_2 (Cases 3S and 3W). The parameters of the six simulations are given in Tab. 3.

All of the simulations are performed under the same initialized conditions. The flame and vortex parameters have been matched to facilitate the investigation of these fuel mixtures in a dynamic setting. This being the case, each simulation is observed and compared at specific instants in time. The observation of qualitative characteristics is important to the study as a whole. However, much of this has been accomplished during the validation study. Therefore, greater emphasis is placed on the changes to quantitative characteristics such as

strain and curvature.

5.3.1 Interactions with Weak Vortices

Qualitative characteristics of the interaction between the Case 1 flame and the weak vortex (Case 1W) have been provided in the validation stage. The observations made for that particular case are consistent throughout the simulations involving syngas (2W and 3W). In each case, the vortices are completely attenuated ahead of the flame, with moderate levels of FGV, and the eventual pinch-off of the flame. The images in Fig. 19 are highly representative of the general flame behavior for all weak-vortex interactions.

While the behavior is qualitatively similar, the effects of syngas on flame stretch are more apparent during quantitative analysis. The strain rate component of flame stretch is primarily dictated by the dynamics of the flow ahead of the flame. Since each flame experiences the same flow conditions at initiation, the strain rates will generally be altered by changes to the orientation of the flame front (i.e. curvature).

To analyze the characteristics of flame stretch, a progress variable must be chosen. In this case, the value $c_f = 0.9$ has been selected, corresponding to the 10% CH_4 mass fraction contour. This isosurface is consistently located in the vicinity of peak methane reaction magnitude, regardless of the fuel composition. Since the Case 2 and Case 3 flames contain modest fractions of CO and H_2, the flame location is still dictated, primarily, by the methane reaction zone. Progress variables as low as 0.7, and as high as 0.95 reveal flame surface area variations of less than 1%.

The most basic, yet reliable, method to determine if *syngas* affects flame stretch is to observe the changes in flame surface area over time. Surface area variations are a definitive characteristic of stretched flames, and they are relatively easy to compute. In 2-D, the flame is assumed to be of unit depth, therefore, the surface area is defined by the arc length of the flame isosurface, s_f. To address these changes in flame area, a surface growth factor, A_F, is defined:

$$A_F = \frac{s_f^t - s_f^u}{s_f^u} \ . \tag{75}$$

Table 4: Flame surface area growth factors for the weak-vortex interactions, taken at several instances prior to pocket formation.

Sample No.	Time (milliseconds)	Case 1W A_F	Case 2W A_F	Case 3W A_F
1	13.5	0.3067	0.3086	0.4342
2	16.2	0.4812	0.4818	0.7058
3	18.9	0.6711	0.6720	0.9978
4	21.6	0.8557	0.8561	1.2986
5	24.3	1.0134	1.0126	1.5539

Here, s_f^u represents the unstretched (arc) length of the flame surface, and s_f^t is the length at time t. A value of $A_f = 0$ corresponds to the unstretched, planar flame (for which $s_f^t = s_f^u$). Similarly, $A_F = 1$ corresponds to a doubling of the flame surface ($s_f^t = 2s_f^u$), and so on.

Table 4 shows the evolution of the flame surface growth factors for the weak vortex interactions. Upon observation of this data, two distinct trends are quite evident. The first is the obvious similarity between cases 1W and 2W. At each point in time, their difference in flame surface growth is less than 1%, meaning that their respective surface areas are essentially the same at all points.

The second observed trend is the substantial rate of surface area increase for the Case 3 flame. Over comparable time intervals, the hydrogen-enriched flame is apparently much more susceptible to stretching. At time $t \approx 13.5\ ms$, the interactions are approximately 50% completed (i.e. half-way to flame pinch-off). At this relatively early instant in time, the flame growth for Case 3W is approximately 42% greater than that of the control case, 1W. Near the end of the interactions, this value increases to approximately 55%

Since the growth factors in Tab. 4 increase linearly with time, a global flame stretch value, K_{glob}, can be determined for each case. Recalling that the flame stretch ($K \equiv dA/Adt$) is a spatially-dependent and dynamic variable, it is not logical to use a global stretch value for instantaneous analyses. However, in the flame-vortex interactions, where similar physical phenomenon (such as quenching or pocket formation) are observed, it is a useful characteristic value. Applying the equation

$$K_{glob} = \frac{1}{s_f^t} \frac{s_f^t - s_f^u}{\Delta t} \tag{76}$$

just prior to pinch-off, produces global stretch values of 20.99, 20.69, and 25.00 s^{-1} for Cases 1W, 2W, and 3W, respectively.

Figure 22 shows strain rate profiles taken along the $c = 0.9$ flame isosurface. Since the flame surface areas (i.e. arc lengths) are not always equal, they have been normalized according to

$$x_n = \frac{x(s)}{s_f^t} \ . \tag{77}$$

This results in a better direct comparison between cases. Here, $x(s)$ is the local position along the flame surface, and x_n is the corresponding normalized position, relative to s_f^t. This defines all of the flame surfaces over a [0,1] range, where $x_n = 0.5$ corresponds to the symmetry plane located at the centerline of the vortex toroid.

As shown in Tab. 4, the agreement between Cases 1W and 2W is unmistakable. This is further demonstrated in Figs. 22a and 22b. At time $t \approx 16.2\ ms$, the strain rate profiles for all three cases demonstrate fairly similar behavior. However, the CH_4 and CH_4/CO flames tend to show very similar magnitudes, whereas the CH_4/H_2 strain rates are generally lower in magnitude for both positive and negative straining.

The strain rates at time $t \approx 24.3\ ms$ show clear distinction between Cases 1W and 3W, while Case 2W remains consistent with the control case. This indicates that, for weak-vortex interactions, the flowfield ahead of the flame is not substantially altered by the presence of CO. Coupling this observation with the observation of comparable K_{glob} values, it is logical to assume that the surface curvature between the 1W and 2W will be nearly identical. At the same time, it is logical to assume that the surface curvature for 3W will be (at a minimum) distinguishable from the control case.

The surface curvature profiles for weak-vortex interactions are given in Figs. 23a and 23b. The results confirm the proposed assumptions. Curvature between the CH_4 and

CH_4/CO flames is nearly identical, both in the midst of the interaction (16.2 ms), and near the end (24.3 ms).

For the CH_4 and CH_4/H_2 flames, at time $t \approx 16.2$ ms, the peak values for positive and negative curvature differ by approximately 150/m and 100/m, respectively. Another important observation is that the relative lengths of the positively- and negatively-curved flame segments are not the same. The fraction of positive curvature along the CH_4/H_2 flame is much greater, while the fraction of negative curvature, near the leading edge of the vortex toroid, is slightly less.

At $t \approx 24.3$ ms (Fig. 23b), the flames are about to pinch off, and there are sharp tips at the former leading edge of the (attenuated) vortices. Much like a bunsen flame, the negative curvature at these flame tips is very sharp. The magnitude of negative curvature is more than double that of the positive curvature for each of the cases. Negative curvature is slightly stronger for Cases 1W and 2W at the centerline. This indicates that, for Case 3W, the flame is either more-responsive to radial fluid motion (e.g. wider radius of curvature) [9], or less-susceptible to kinematic restoration [57].

In Case 3W, the sharp dip and rise in positive curvature is an indication that this particular flame is approaching the pinch-off stage much faster. The elongated region of positive curvature, shown in Fig. 23a, contributes to increased fuel consumption behind the vortices, and ultimately leads to merging of the flame surface (i.e. pinch-off). For Cases 1W and 2W, similar behavior is observed, but much less pronounced.

Preferential diffusion plays a key role in defining the respective characteristics of these three cases. The diffusional characteristics of CO are much like those of air ($MW_{CO} \approx MW_{Air}$), meaning that fuel mixtures with relatively low volumes of CO will behave as though they are slightly leaner. However, unlike an equal fraction of air, the CO is oxidized (e.g. reactions 55b, 55d, and 55e), thus contributing to the vigor of flame. Therefore, it is reasonable for the Case 2 flame to behave like the Case 1 flame, as preferential diffusion of CH_4 still defines the dynamics of the flame front [13].

Case 3W reveals substantially larger growth of the flame front, indicating that the diffusion of H_2 through the primary CH_4 reaction zone promotes flame stretching. In the

(a) Flame Strain: Weak Vortex ($t \approx 16.2\ ms$)

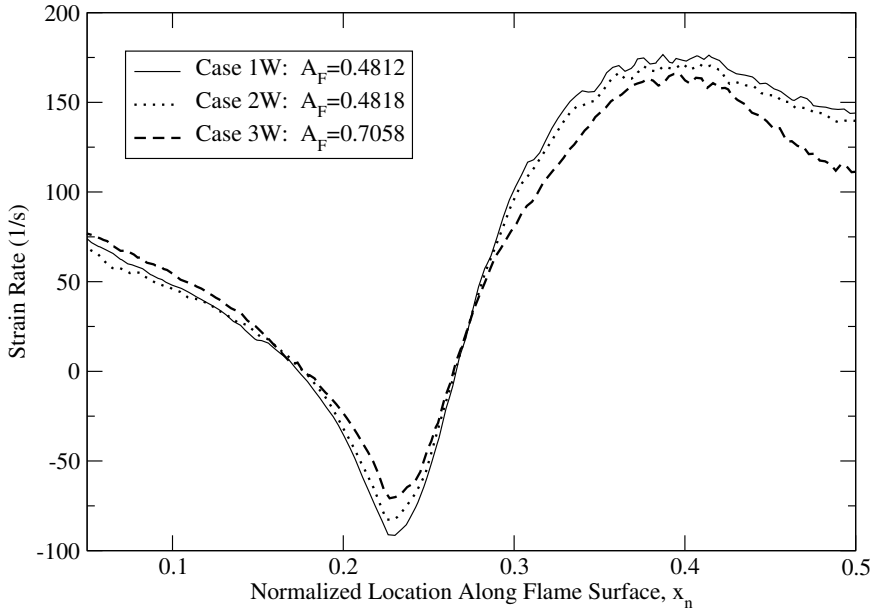

(b) Flame Strain: Weak Vortex ($t \approx 24.3\ ms$)

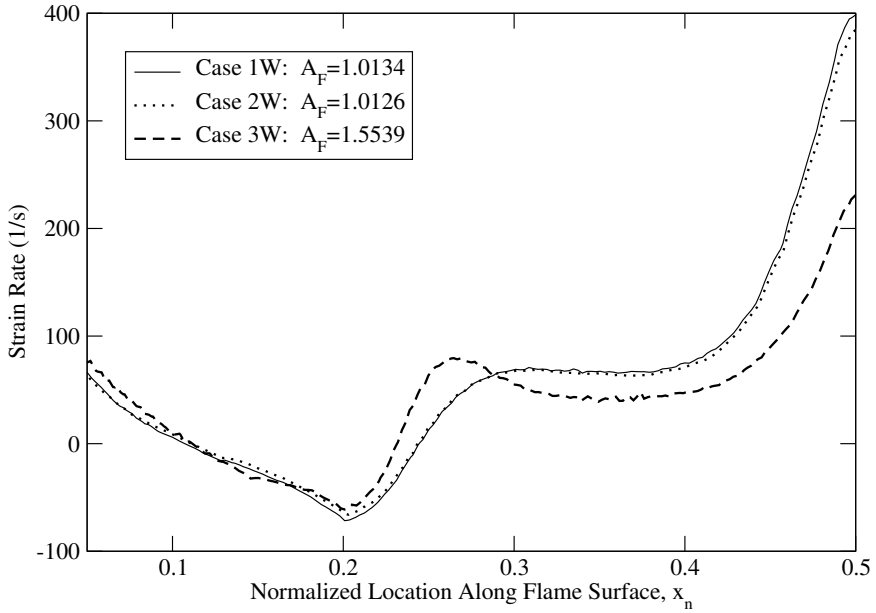

Figure 22: Strain rate profiles for the three flames during weak-vortex interaction. Values are taken along the normalized flame surfaces ($c = 0.9$) at (a) 16.2 ms and (b) 24.3 ms. The trends for CH_4 and CH_4/CO flames are essentially the same, while the CH_4/H_2 flame demonstrates quantitatively different behavior.

(a) Flame Curvature: Weak Vortex ($t \approx 16.2\ ms$)

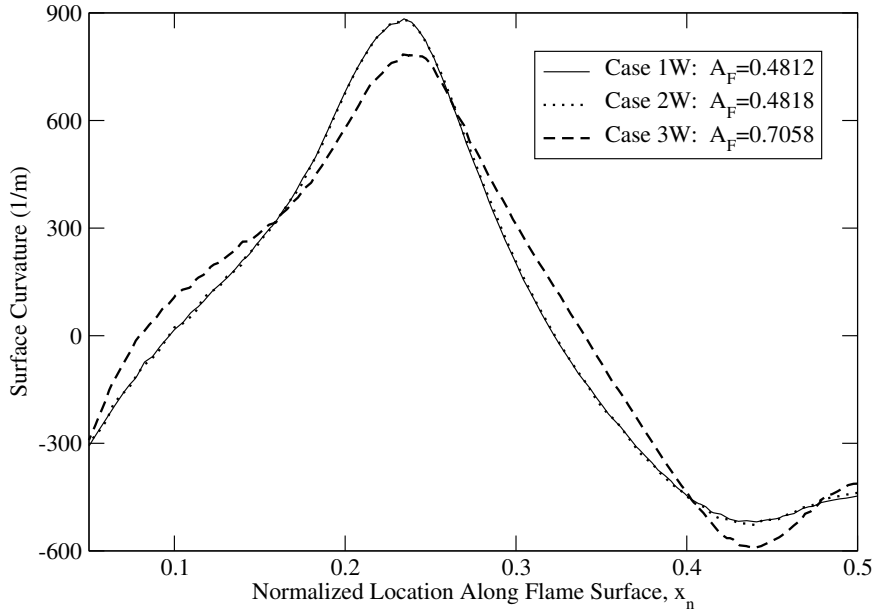

(b) Flame Curvature: Weak Vortex ($t \approx 24.3\ ms$)

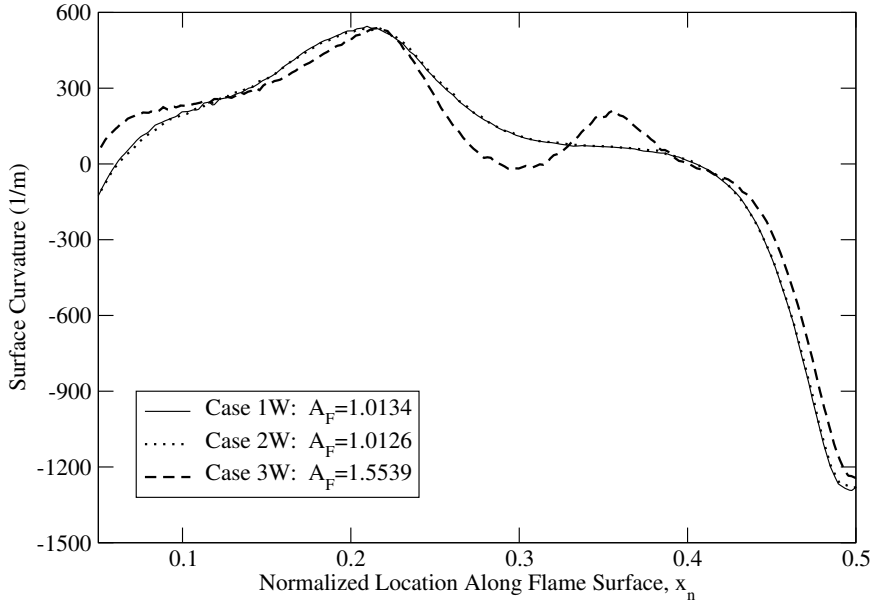

Figure 23: Surface curvature profiles for the three flames during weak-vortex interaction. Values are taken along the normalized flame surfaces ($c = 0.9$) at (a) 16.2 ms and (b) 24.3 ms. At 16.2 ms, the behavior is the same for all cases, but the magnitudes for Case 3W are different. At 24.3 ms the behavior and magnitudes are different for Case 3W. Curvature for Cases 1W and 2W is essentially equal.

Table 5: Flame surface area growth factors for the strong-vortex interactions, taken at several instances prior to pocket formation.

Sample No.	Time (milliseconds)	Case 1S A_F	Case 2S A_F	Case 3S A_F
1	2.7	0.0395	0.0357	0.0379
2	5.4	0.2168	0.2276	0.3064
3	8.1	0.6847	0.7030	1.0424
4	10.8	1.2966	1.3067	1.7899
5	12.4	1.6191	1.6243	2.2444

vicinity of negative curvature, rapid diffusion of H_2 effectively leans the reactant mixture making the flame more susceptible to stretching. Along positively-curved segments, fuel is diffusing into the convex reaction zone, producing a stronger flame and leading to further extensive (positive) stretching.

5.3.2 Interactions with Strong Vortices

Much like the weak-vortex interactions, the qualitative flame characteristics for the strong-vortex interactions involving *syngas* (Cases 2S and 3S) are analogous to those of the strong-vortex validation (Case 1S). While the weak-vortex interactions produced a bunsen-like flame tip at the vortex leading edge, the strong-vortex interactions produce a large, mushroom-like "bubble" of reactants that carries the flame as it is convected forward. The incident vortices are strong enough to sustain rotation well after the flame has pinched off, and there is no substantial FGV present.

As before, the flame surface growth factors are computed for Cases 1S-3S. These results are shown in Tab. 5. Despite the increased vortex strength, the CH_4 and CH_4/CO cases (1S and 2S) still accumulate approximately the same surface area over time. However, for these cases, the fractions of flame growth are approximately 60% greater than in the previous weak-vortex interactions. For the Case 3S flame-vortex interaction, the flame surface area is increased to approximately 2 1/4 times its original, unstretched value. While this surface growth is much larger than the corresponding 1S and 2S cases, the relative magnitude is only 33% greater, whereas, in the weak-vortex interaction it was 50% greater.

Cases 1S and 2S pinch off at approximately the same point in time, while Case 3S pinches off nearly 1 millisecond sooner. The corresponding global stretch values computed from Eqn. 76 are found to be 50.42, 49.75, and 55.65 s^{-1}, respectively. Although these values are taken at the point when Case 3S pinches off, the remaining surface growth for 1S and 2S is not significant, and these values are indicative of the characteristic stretch rates.

Strain rate profiles for the three cases are shown at $t \approx 8.1\ ms$ and $t \approx 12.4\ ms$ in Figs. 24a and 24b, respectively. As should be expected, the surviving vorticity generally results in substantially greater straining of the flame surface for each case. At the first instant in time, the peak strain rate magnitudes are more than double those of the weak-vortex interactions. However, just before Case 3S pinches off ($t \approx 12.4\ ms$), the strain rates at the toroid centerline are not as high as those for the bunsen-like tip in Cases 1W-3W. At the leading edge of the strong vortex pair, the negative curvature of the flame front is much more gradual due to the presence of the large fluid structures. For gradual curvature, divergence of the flow passing through the flame is less severe, hence the lower strain rates.

At $t \approx 8.1\ ms$, Fig. 24a reveals that the 1S and 2S strain rates are quite similar on a qualitative and quantitative basis. The peak, positive strain rates along the 3S flame are nearly equal in magnitude to the control case. However, in the low- and negative-strain regions, the behavior and magnitudes between Cases 1S and 3S are quite different. The maximum negative strain rate is approximately 100 s^{-1} lower for the 3S interaction, indicating that curvature of the flame front may not be as pronounced along the $x_n = [0.2,\ 0.3]$ segment of the flame. While the transition between positive and negative straining is smooth for the 1S and 2S cases, there is a slight variation in the 3S strain rates, likely caused by a combination of excessive curvature and opposing fluid motion from the vortex.

Near the instant in which Case 3S pinches off, fluid motion along the flame surface is rather erratic. At this point in time, the maximum strain rate magnitudes are observed along the CH_4/H_2 flame. Fig 24b shows that, on two separate occasions, all three of the cases transition between positive and negative straining. Referring back to the flow visualization of Case 1S (e.g. Figs. 21d and 21e), these transitions occur near the curvature inflection points, and are generated by the vortex, which has forced the flame and hot

products back toward the reactant stream.

The corresponding surface curvature profiles, provided in Figs. 25a and 25b, confirm the preceding observations. At $t \approx 8.1\ ms$, the existence of lower strain rates in Case 3S corresponds to a broadened, and less severe, region of positive curvature. The maximum positive curvature is nearly twice as large for Cases 1S and 2S, whereas the maximum negative curvature is approximately equal for all cases. These characteristics are analogous to those observed in Fig. 24a, which shows unequal negative straining and nearly equal positive straining.

At $t \approx 12.4\ ms$, Fig. 25b reveals that, well behind the vortices, the flame surface curvature is approximately equal for all three cases. However, values closer to the fluid structures indicate that the presence of H_2 still has a significant impact on the structure of the flame front. Substantial positive and negative curvature are induced by a combination of vortical effects. As the vortices carry the flame forward, hot products are forced into the rear of the vortex toroid, and cold reactants are forced into the flame front at the leading edge.

For all three casees, the curvature magnitudes are consistent with the strain rate magnitudes observed in Fig. 24b. The transition from positive to negative curvature occurs over a shorter range of x_n for Case 3S. This is due to the substantial surface stretching that takes place behind the vortices. In Cases 1S and 2S a greater fraction of the flame surface is directly involved in the flame-vortex interaction.

Pinch-off of the 3S flame occurs along the segment where the curvature drops to zero. Behind the vortices, a short section of the flame ($x_n \approx [0.23,\ 0.27]$) is nearly parallel to the flow, causing it to burn toward the centerline, and consume all of the reactants in its path with nearly no opposition from the flow. Pinch-off of the 1S and 2S flames occurs in the same fashion at a later time.

For the strong-vortex interactions, preferential diffusion effects are still applicable. However, in these cases, the fluid motion has a much greater effect on the flame due to the survival of the vortices. For weak-vortex interactions, the early vorticity attenuation amplifies the effects of the chemical processes. Consider the positively-curved flame segments

(a) Flame Strain: Strong Vortex ($t \approx 8.1\ ms$)

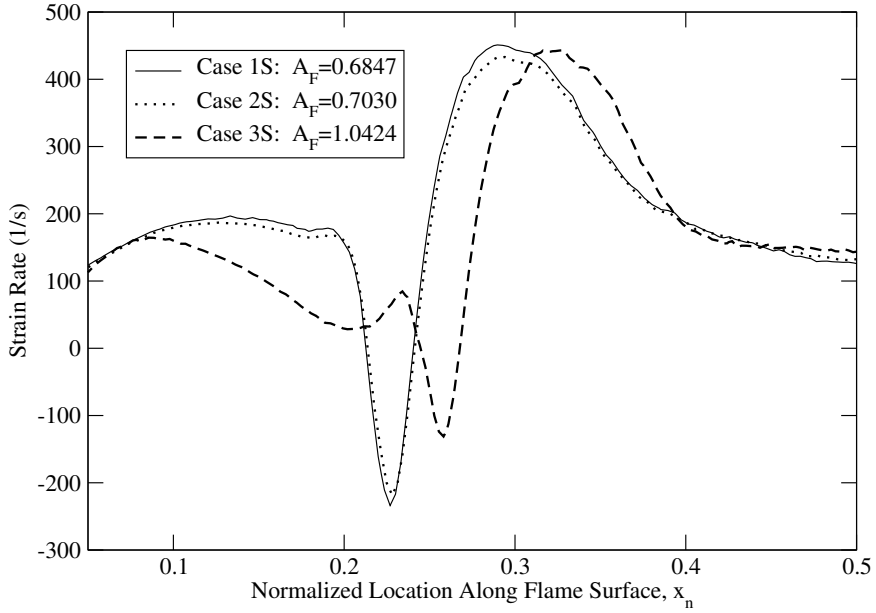

(b) Flame Strain: Strong Vortex ($t \approx 12.4\ ms$)

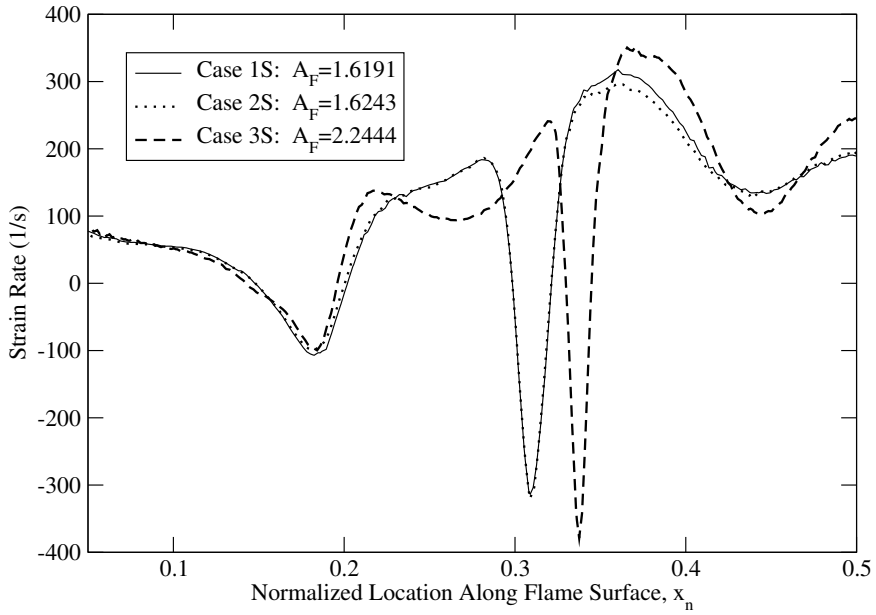

Figure 24: Strain rate profiles for the three flames during strong-vortex interaction. Values are taken along the normalized flame surfaces ($c = 0.9$) at (a) 8.1 ms and (b) 12.4 ms. The trends for CH_4 and CH_4/CO flames are essentially the same, once again, while the CH_4/H_2 flame demonstrates both qualitative and quantitative differences.

(a) Flame Curvature: Strong Vortex ($t \approx 8.1\ ms$)

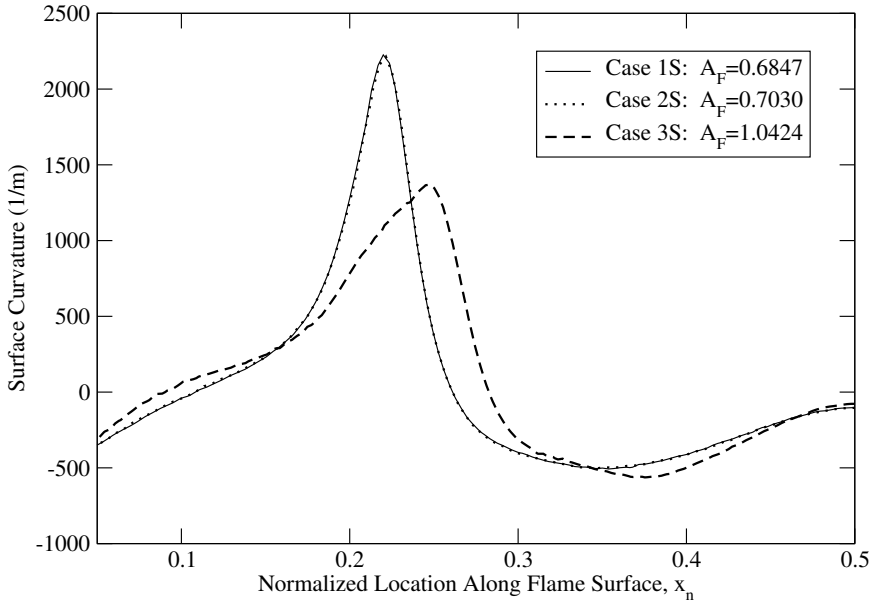

(b) Flame Curvature: Strong Vortex ($t \approx 12.4\ ms$)

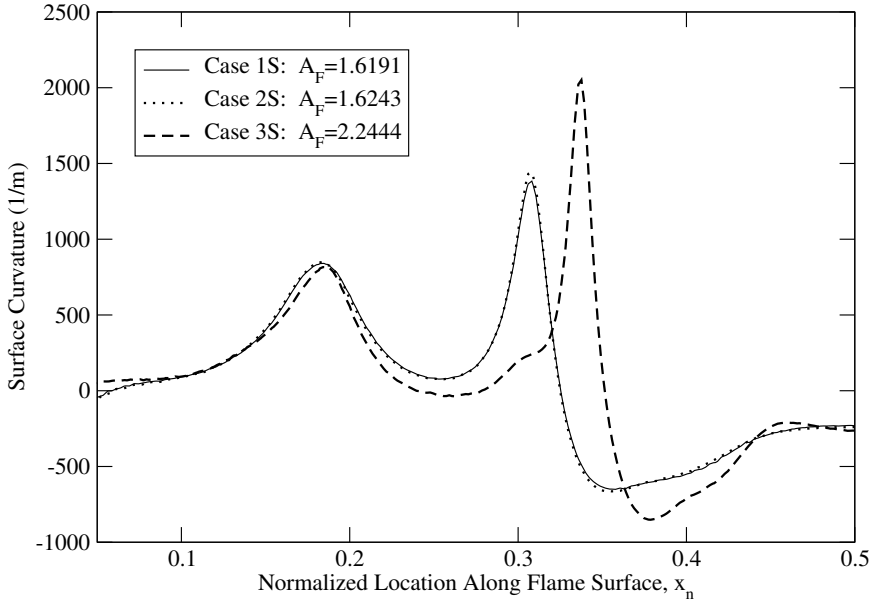

Figure 25: Surface curvature profiles for the three flames during strong-vortex interaction. Values are taken along the normalized flame surfaces ($c = 0.9$) at (a) 8.1 ms and (b) 12.4 ms. At 8.1 ms, positive curvature of the 1W and 2W flame surfaces is much larger than that of the 3W flame. At 12.4 ms the peak curvature values are found along the 3W flame. The transition from positive to negative curvature is more compact in Case 3W.

during strong and weak vortex interactions. In the strong case, the vortex is not attenuated, and the flame surface continues to grow (stretch) due to the motion of the hot products in the flame-direction (i.e. direction of flame propagation) and diffusion-enhanced burning (inward diffusion of fuel molecules). In the weak case, the vortex is attenuated, but the positively-curved segment still continues to grow due to enhanced burning.

5.4 Displacement Speed Comparison

Citing discrepancies between experimental and numerical formulations of the flame displacement speed, S_d, an independent, surface-averaged technique has been formulated. The concept of a surface-averaged displacement speed is similar to experimental formulations, such as those by Sinibaldi et al. [11, 25], in which specific elements of the flame surface, dA, have a known stretch value (K), strain rate ($\nabla_t \cdot \vec{u}$), and curvature ($\nabla \cdot \vec{n}$). The displacement speed is easily recovered from the equation for flame stretch, Eqn. 4.

However, in experimentation and simulation it is very diffcult to track particular segments of the flame over time, considering that stretch rates vary along the flame surface. It is for this reason that the surface-averaged displacement speed is formulated. As addressed throughout this chapter, the strain rates and curvature are known along the flame surface for instantaneous DNS solutions. This means that only two of the four dependent variables are known, while the other two, K and S_d, remain unknown. Since analytically-derived S_d values are difficult to define (and often questionable), the new technique examines regions of the flame having either positive or negative curvature, and defines a local displacement speed based on surface-averaged stretch rates.

The difference between CH_4 and CH_4/CO flames is essentially negligible, therefore, surface-averaged comparisons are made between CH_4 and CH_4/H_2 flames with comparable fractions (x_n) of negative curvature. Table 6 gives the conditions of four instantaneous stretched flame solutions (two for weak-vortex and two for strong-vortex interactions). These flames have approximately the same surface growth factors, A_F, but more importantly, they have approximately the same fraction of surface area experiencing negative curvature. This is shown in Figs. 26a and 26b, along with the respective strain rates.

(a) Weak-Vortex Interaction

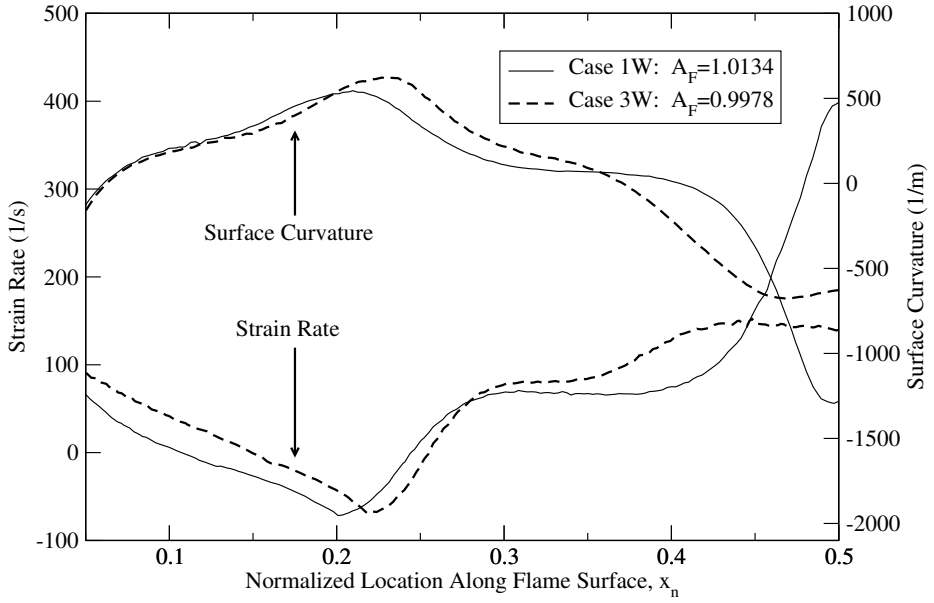

(b) Strong-Vortex Interaction

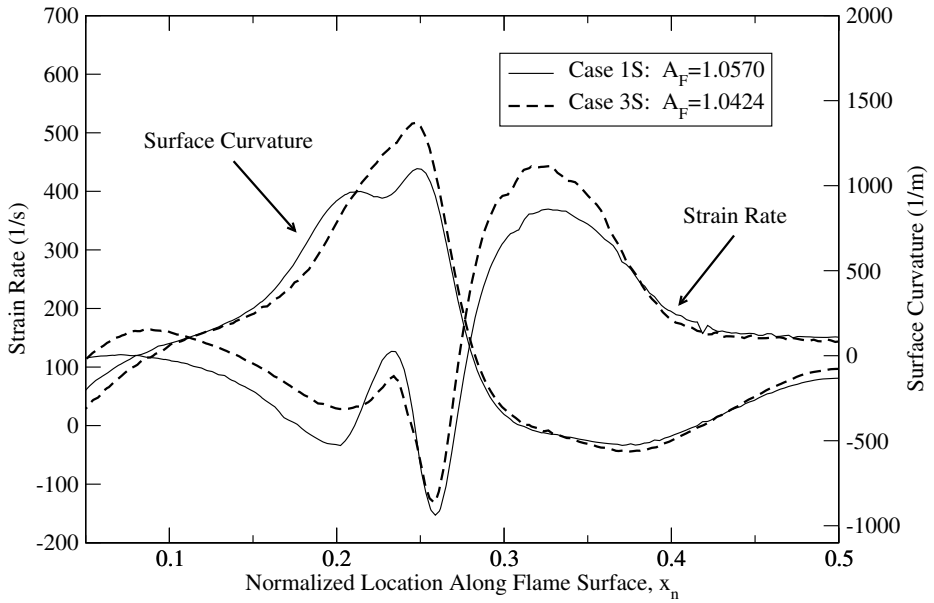

Figure 26: Strain rate and surface curvature profiles for weak-vortex (Cases 1W and 3W) and strong-vortex (Cases 1S and 3S) interactions having similar negatively-curved surface areas. The negatively-curved portions are of interest to the formulation of surface-averaged stretch rates and comparison of local displacement speeds between CH_4 and CH_4/H_2 flames.

Table 6: Conditions of four instantaneous cases used to compare stretched CH_4 and CH_4/H_2 flames having the same surface area (A_F). Cases 1W and 3W represent the comparison between weak-vortex interactions, while 1S and 3S represent strong-vortex interactions.

Interaction	Time (ms)	A_F
1W	24.3	1.0134
3W	18.9	0.9978
1S	9.6	1.0570
3S	8.1	1.0424

Treating the negatively-curved portion of the flame as surface element dA, the average stretch rate is determined by the fundamental form, $K \equiv dA/Adt$, where A is the current area of the surface element, and dt is the time period over which the rate is determined ($\pm 20,000\Delta t$). It has been shown in this chapter that the increase of surface growth factors is approximately linear once significant stretching has commenced. Therefore, the average stretch rate over some dt can be safely interpolated to any inclusive instant in time.

The 2-D form of the surface-averaged stretch rate is represented by

$$\bar{K} = \frac{1}{s_{neg}^{t}} \frac{s_{neg}^{t_2} - s_{neg}^{t_1}}{t_2 - t_1} \tag{78}$$

where s_{neg} denotes the arc length along the negatively-curved surface, and superscripts t, t_1, and t_2 represent three points during the interaction: the current instant, 20,000 timesteps prior ($t-2[10^4]\Delta t$), and 20,000 timesteps after ($t+2[10^4]\Delta t$), respectively. At the four points of interest in Tab. 6, the surface-averaged stretch rates are found to be -19.18 (1W), -9.54 (3W), 16.46 (1S), and 32.73 s^{-1} (3S). These rates are determined from the instantaneous values listed in Tab. 7.

From these average stretch rates, several important observations can be made. During the weak-vortex interactions, *compressive* (i.e. negative) stretching is taking place along the negatively-curved regions of both flames. Additionally, the rate of *compressive* stretching in the CH_4 flame is more than double that of the CH_4/H_2 flame. For the strong-vortex interactions, the exact opposite is true. *Extensive* (i.e. positive) stretching is taking place

Table 7: Parameters used to determine surface-averaged stretch rates for the four instantaneous cases in Tab. 6. Here, dA is represented by $(s_{neg}^{t_2} - s_{neg}^{t_1})$ and dt is represented by $(t_2 - t_1)$, where $t_1 = t - 2(10^4)\Delta t$ and $t_2 = t + 2(10^4)\Delta t$. The surface area (A) at time t, corresponding to negative curvature, is represented by s_{neg}^{t}.

Interaction ID	s_{neg}^{t} (cm)	t_1 (ms)	$s_{neg}^{t_1}$ (cm)	t_2 (ms)	$s_{neg}^{t_2}$ (cm)	$\bar{K}$ s^{-1}
1W	3.0201	23.44	0.6051	24.52	0.5425	-19.18
3W	2.9966	18.43	0.7910	19.50	0.7604	-9.54
1S	3.1001	9.06	1.3184	10.13	1.3730	16.46
3S	3.0637	7.59	1.2686	8.67	1.3769	32.73

along both of the negatively-curved regions, and the rate of *extensive* stretching in the CH_4 flame is approximately half that of the CH_4/H_2 flame.

Poinsot's [9] equation for flame stretch can be rearranged and solved for the local displacement speed, making use of the newly-determined, surface-averaged stretch rate, $\bar{K}$. Its 2-D form is written as

$$S_d = \frac{\bar{K} - \nabla_t \cdot \vec{u}}{\nabla \cdot \vec{n}} \tag{79}$$

where the strain rate $(\nabla_t \cdot \vec{u})$ and curvature $(\nabla \cdot \vec{n})$ are locally-known values. When applied to negatively-curved surfaces of the instantaneous solutions for Cases 1W, 3W, 1S, and 3S, this formula produces the trends shown in Fig. 27.

In the weak-vortex interactions, the displacement speeds of the CH_4/H_2 flame are consistently lower than those along the CH_4 flame. This is in agreement with the preceding results that indicate a greater susceptibility to surface area growth and reduced compressive stretching in the presence of H_2. These observations are analogous to a reduced forward displacement of the flame.

From Fig. 26b, it is clear that most of the flame stretch discrepancy in the strong-vortex interactions occurs between the strain rates. At these particular instants, the length and magnitudes of negative curvature are approximately the same, whereas the strain rates for the CH_4/H_2 flame are greater throughout 40% of the surface. This, combined with the

vastly different surface-averaged stretch rates, produces two S_d trends that follow the same pattern, but alternate in magnitude.

This technique is fairly simple to implement, and gives a good qualitative assessment of the displacement speed variations along comparably-stretched flames. However, there are some fundamental flaws that must be considered. The most basic flaw is the fact that the local stretch rates are not consistent along the flame surface, but vary with respect to local curvature and straining. Another fundamental flaw is the definition of S_d in the limit of zero surface curvature. Where the flame surface approaches a transition between positive and negative curvature, the value of $\nabla \cdot \vec{n}$ approaches zero in the denominator of Eqn. 79, causing unphysical displacement speed values (e.g. in Fig. 27, maximum S_d values approach $90 \times S_L$).

As discussed in Chapter 1, Gran et al. [2] implemented a theoretical model for the flame displacement speed based on diffusional properties. This model, derived from the species transport equation, is composed of a flame-tangent diffusion term, a flame-normal diffusion term, and a reactive term. When these terms are combined, S_d is mathematically represented by

$$S_d = -\underbrace{\frac{\nabla_t \left(\rho D_k \nabla_t Y_k\right)}{\rho |\nabla Y_k|}}_{flame-tangent} - \underbrace{\frac{\nabla_n \left(\rho D_k \nabla_n Y_k\right)}{\rho |\nabla Y_k|}}_{flame-normal} - \underbrace{\frac{\dot{w}_k}{\rho |\nabla Y_k|}}_{reactive} \tag{80}$$

where ∇_t and ∇_n represent tangential and normal gradient operators, respectively. The results of this formulation are shown in Fig. 28 for the four cases already examined.

This model has been criticized for its tendency to produce negative flame speeds which are argued to be unrealistic as they are not observed in experiements [11]. However, the instances of negative S_d are much less frequent than positive S_d, and the peak values vary by an order of magnitude. Negative values occur primarily in the region adjacent to the transition between positive and negative curvature, where the flow is highly-tangent to the flame surface.

Large S_d magnitudes are observed in both the surface-averaged and theoretical formulations, however, behavior is not consistent between the two. In the surface-averaged formulation, the weak-vortex interactions see declining displacement speeds as maximum curvature is approached. According to the theoretical formulation, the opposite is true, as displacement speeds rise substantially in the vicinity of maximum curvature. For strong-vortex interactions, the same basic trends are observed. The surface-averaged values of S_d are lowest near maximum curvature, while the theoretical values are highest near maximum curvature.

While both techniques are based on physical principles of the strained/curved flame surface, the latter appears to be more realistic, and locally feasible. The trends for the theoretical formulation are based on local information, rather than an averaged quantity. Therefore, qualitative comparisons can be made, even if inconsistencies in the displacement speed magnitudes exist. Since each value is independent of the others, any inconsistency is universal.

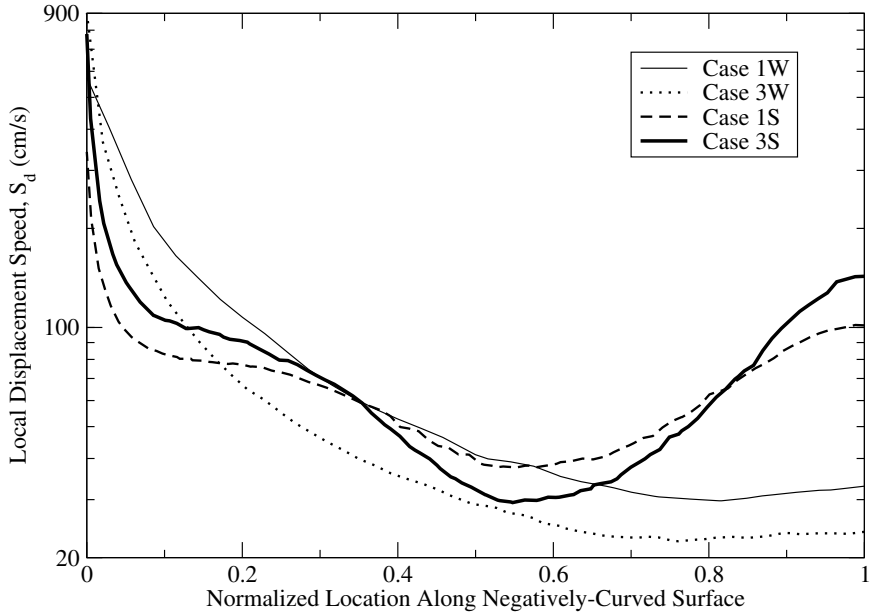

Figure 27: Surface-averaged displacement speed trends along negatively-curved CH_4 and CH_4/H_2 flame surfaces in weak-vortex and strong-vortex interactions. Here, S_d is computed from the surface-averaged stretch rate formulation.

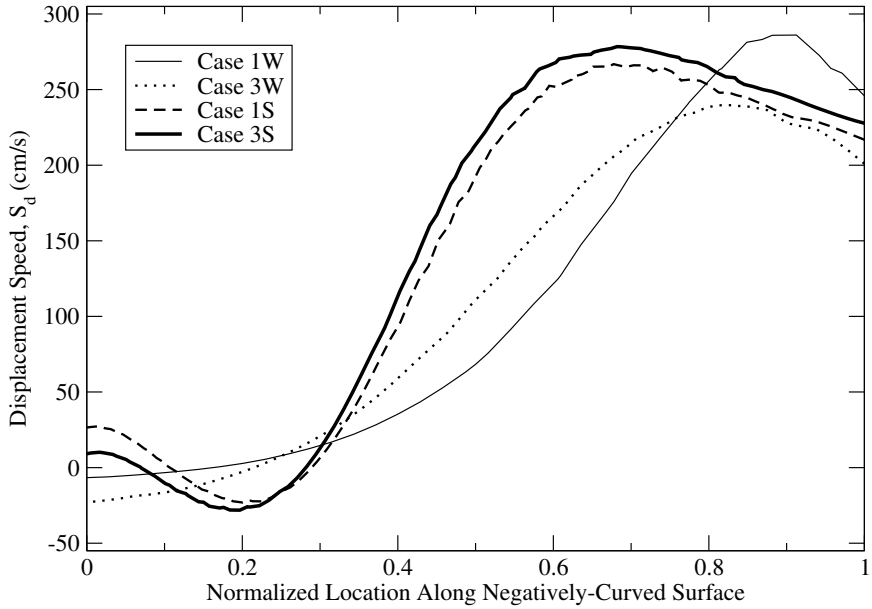

Figure 28: Theoretical displacement speed trends along negatively-curved CH_4 and CH_4/H_2 flame surfaces in weak-vortex and strong-vortex interactions. Here, S_d is computed using the theoretical formulation proposed by Gran et al. [2].

CHAPTER VI

CONCLUSIONS

The study of flame-vortex interactions in natural and synthetic gas mixtures has been successfully performed. The results and observations provided here have demonstrated a wide variety of flame behavior for various fuel mixtures and vortex configurations. Laminar, premixed methane-air flames were shown to be substantially enhanced by the presence of small H_2 fuel fractions. On the other hand, these same flames experienced marginal variations in the presence of both small and large CO fuel fractions.

- ***Effects of Carbon Monoxide***

Between extensive testing of laminar, 1-D flames and multiple flame-vortex simulations, the addition of *syngas-based* CO was shown to have negligible effects. Its presence in the 1-D flame simulations resulted in laminar flame speeds and flame temperatures that were comparable to methane-air flames at the same equivalence ratio. In the flame-vortex interactions, the addition of 30% CO to the reactant stream produced little (if any) change to the flame structure.

The less-diffuse nature of carbon monoxide did not appear to inhibit, nor promote the consumption of the primary fuel (methane). Despite substantial straining and curvature of the flame front, the primary reaction zone was consistently defined by the consumption of CH_4. As mentioned in the Chap. 5, the CH_4/CO mixtures behaved like pure CH_4 mixtures due to the observed duality of CO. On one hand, CO is very likely to inhibit molecular diffusion of the fuel mixture. This is especially true for lean fuel-air mixtures (since $MW_{CO} \approx MW_{Air}$). On the other hand, the presence of CO in the reactant mixture promotes carbon monoxide oxidation, a process which typically takes place at a much slower rate and/or later in the flame.

The promotion of CO oxidation reduces the presence of oxygen molecules (O_2), and the resulting mixture moves closer to stoichiometric methane-air. Upon inspection of the CH_4 and CH_4/CO flames, it was found that the maximum rate of CO production was 35% lower, and the maximum rate of CO oxidation was 22% higher in the CH_4/CO flame. Additionally, the onset temperature for CO oxidation was 55 K lower for the CH_4/CO flame. These factors individually contribute to the theory of promoted CO oxidation, and its impact on the effective stoichiometry of the methane-air mixture.

To determine the validity of this theory, a full analysis of the individual forward and reverse reaction rates would be required for all applicable reaction steps at several locations through the 1-D flame. Such an analysis may prove to be fruitless, considering that non-zero reactant concentrations of CO will inevitably result in the promotion of CO oxidation reactions anyhow. Ultimately, the fact that this theory (or some alternative underlying cause) is dedicated to a lack of definitive conclusions disourages any further analysis here.

- ***Effects of Hydrogen***

The addition of *syngas-based* H_2 has shown dramatic changes to the dynamics of laminar stretched methane-air flames. The temporal characteristics of hydrogen-enhanced flames revealed a clear distinction from pure CH_4 flames, primarily in their susceptibility to stretching. As the two flames advanced in time, the CH_4/H_2 flame provided less resistance to the incoming fluid, resulting in a broadened flame surface with gradual transitions between negative and positive curvature.

Throughout the discussion, many of the observations of CH_4/H_2 flames were attributed to the rapid diffusion of H_2 through the primary reaction zone. This promoted fluid motion in the streamwise direction, but it also increased reactivity behind the flame, thus opposing propagation of the flame into the oncoming reactant stream. Figure 29 illustrates these phenomena quite well.

The figure shows the existence of a dual reaction zone in which the majority of H_2 consumption takes place behind the primary CH_4 reaction zone. This same phenomenon

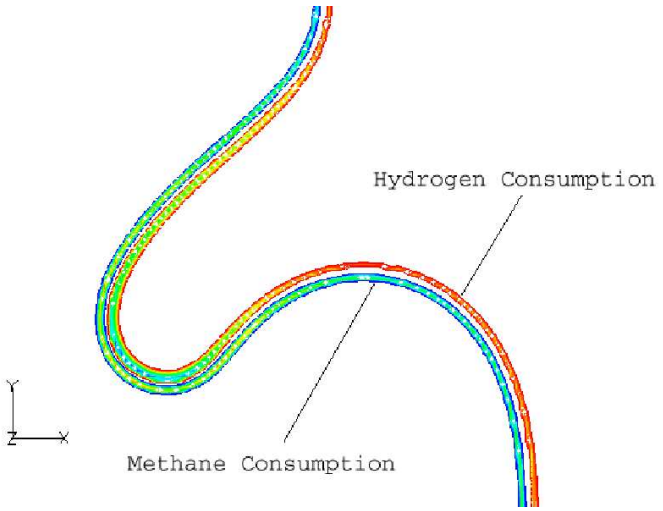

Figure 29: Peak reaction rate contours of CH_4 and H_2 consumption during interaction between a strong vortex and the CH_4/H_2 flame. The figure demonstrates the presence of a "dual" reaction zone in which a majority of the fuel-based hydrogen diffuses through the methane reaction layer and is consumed at the rear of the flame. Colors are inverted to show distinction.

is evident in Fig. 30, which shows 1-D OPPDIF solutions for the $CH_4/H_2/Air$ flame (using GRI-Mech 3.0) under strong and weak stretching. The presence of dual CH_4 and H_2 consumptions zones is consistent in stretched flames with positive, negative, and zero curvature. While similar observations can be made for CH_4/Air flames, the H_2 consumption, in those cases, is on the order of its production.

Along negatively-curved segments of the flame, this dual reaction zone effectively leaned the incoming fuel mixture, resulting in lower $\dot{w}_{CH_4}$, and an increased tendency to stretch. As mentioned earlier, the opposite was true for positively-curved sections of the flame. The focused diffusion of fuel molecules into the flame enhanced both H_2 and CH_4 reactions, allowing the flame to expand and propagate into the oncoming reactants. This was further aided by the circulation of hot products toward the positively-curved flame surface.

It has been shown by Schefer et al. [23] that the use of comparable H_2 fuel fractions in lean methane-air mixtures substantially extends lean flammability limits. It is logical to conclude that the dual reaction zone is at least partially responsible for this.

In the cases examined here, the CH_4 reaction rates have shown clear variations along the stretched flame surfaces, with and without the addition of *syngas*. Under intense stretching,

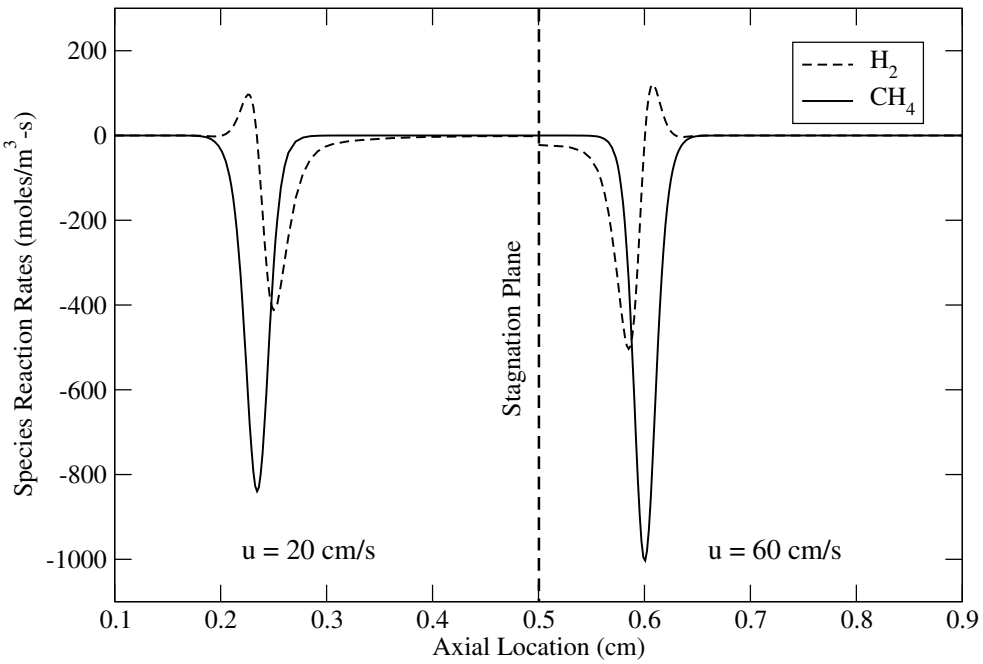

Figure 30: OPPDIF solutions for strong and weakly-stretched $CH_4/H_2/Air$ flames showing separate peaks for methane and hydrogen consumption. As in the flame-vortex simulation, the peak hydrogen consumption exists behind the primary methane consumption zone.

this can cause initially-lean mixtures to become excessively deficient in fuel, and eventually lead to the quenching of fuel reactions ($\dot{w}_{CH_4} \rightarrow 0$). In the zones where CH_4 reactions were diminished, it has been shown that the H_2 reactions are capable of maintaining the structure of the reaction zone.

The promotion of flame stretching by hydrogen addition has many extensions to turbulent combustion. One of the primary influences is on the turbulent burning velocity, S_T, of the flame. Flohr and Pitsch [58] note that the turbulent flame speed is a function of the surface area, which is, in turn, a function of the turbulence intensity. This has been theoretically demonstrated by Zimont [59], and experimentally verified in previously-mentioned studies by Kido et al. [18, 19]. The latter have also shown that the addition of small amounts of H_2 to hydrocarbon fuels substantially increases the values of S_T, and extends the range of attainable turbulence intensities (u'/S_L).

Zimont's proposed equation for turbulent flame speed appears as

$$S_T = u_t^c \overline{\left(\frac{\delta A}{\delta A^0} \right)}, \tag{81}$$

where u_t^c is a characteristic velocity associated with the turbulence intensity, δA is the surface area of a local flame surface element, δA^0 is the projection of that surface element onto a plane normal to the direction of flame propagation, and the overbar indicates averaging over the flame surface. This relates the turbulent flame speed to the average fraction of flame surface growth beyond the planar, unstretched value.

In Zimont's formulation, the increase in turbulent flame speed is attributed purely to the increase in flame surface area caused by turbulent wrinkling. In the current study, it has been shown that stretching and surface area growth of methane-air flames are much greater in the presence of H_2. This indicates that flame surface growth caused by turbulent wrinkling will be much greater in hydrogen-enriched flames than in their pure H/C-fuel counterparts. As reported by Kido et al., the consequences of this hydrogen addition are greater turbulent flame speeds, and extended quenching limits. From the results presented here, it is believed that the observed augmentation of flame surface area by hydrogen addition is the cause of these two phenomenon.

CHAPTER VII

RECOMMENDED WORK

While the scope of this study was limited to the physics of a few multicomponent fuel mixtures and stretched flames, its potential for future research is far-reaching. Many of the previous studies revealed different facets of combustion and fluid dynamics for which flame-vortex interactions are a useful method of study. They also demonstrated the possible benefits of implementing various amounts of *syngas* in different H/C-air mixtures.

In this particular case, the flame-vortex interactions could be subjected to increasingly-lean reactant mixtures to determine stretch rates and quenching limits of multicomponent fuels. There is substantial evidence supporting the extension of H/C-air quenching limits through the addition of small H_2 fractions, therefore, a parametric study of multicomponent fuel mixtures should be performed. This study is also focuses on a limited range of vortex parameters. Since the range of turbulent structures experienced in most practical flows is quite broad, a better representation of the applicable sizes and strengths is required.

The effects of surface curvature in multicomponent fuel mixtures have been addressed here. However, a more fundamental understanding of the mechanisms leading to flame propagation, and altered burning intensity is required. Much is known about the preferential diffusion in single-component fuels such as those studied by Mizomoto et al. [13] and Law et al. [14]. However, the dynamics of diffusion are changed in the presence of fuel-based hydrogen. More-diffuse fuels such as CH_4 in air must compete with H_2, whereas less-diffuse fuels such as C_3H_8 may not see substantial effects. Simulations of 2-D bunsen flames, or flame-vortex interactions with strong curvature, would be a great way to examine the exact effects of H_2 in various fuels.

The specification of a turbulent flame speed is of critical importance to turbulent combustion models. However, little work has been done to address the accuracy of these flame speed models when exposed to various fuel mixtures, or altered reaction rates. This does

not strictly apply to multicomponent fuel mixtures. Similar effects are also observed along stretched flame fronts, particularly along those with significant changes in curvature. The enhancement of flame surface area during H_2 addition is a good indication that current S_T models may not be equipped to handle such mixtures.

The range of imaginable physical scenarios is essentially infinite. However, the range of realizable numerical simulation scenarios is limited. Improvements related to physical models and computational efficiency are generally performed on a case-by-case basis, and are rarely universal. For the most part, the current study has only slightly deviated from this fact. The implementation of a multicomponent transport model is often overlooked based on its added computational cost, and its (questionably) marginal impact on the flame structure. The same can be said for thermally-perfect gas models and extended chemical mechanisms.

While it is nearly impossible to realize all of these things simultaneously, some improvements can be made. The ISAT algorithm can be expanded to include multicomponent transport properties, thus reducing the expense of accurate transport computations. At this point, ISAT optimization is generally ad hoc, and requires a more generic interpretation to handle a wide variety of problems. In developing this generic interpretation, improvements to storage and accuracy may facilitate broader applications, such as the one mentioned here.

Another important factor in numerical combustion simulations is the use of reduced chemical mechanisms. For this study, a pre-existing mechanism was selected and validated within designated limits of accuracy. However, the purpose of these mechanisms is to accurately represent the particular problem at hand, such as methane or propane oxidation. Since this study focuses on the addition of *syngas*, a reduced chemical mechanism should be developed to include the relevant CH_4 reactions as well as the applicable CO and H_2 reactions. Some larger reduced mechanisms include these reactions, however, they include many reactions that are unrelated to CO and H_2 oxidation.

The ultimate goal would be to study turbulent flame stretch in a full range of fuel mixtures, including those studied here, pure *syngas* mixtures, and extended multicomponent mixtures (e.g. $CH_4/CO/H_2$). The flame-vortex interaction has already proven to be one of

the best techniques for studying stretched flame fronts. An optimized, black-box routine, including full control of the vortex parameters, should be developed in order to ensure consistency and accuracy between simulations.

Bibliography

[1] C.J. Mueller, J.F. Driscoll, D.L. Reuss, M.C. Drake, and M.E. Rosalik. Vorticity generation and attenuation as vortices convect through a premixed flame. *Combustion and Flame*, 112:342–358, 1998.

[2] I.R. Gran, T. Echekki, and J.H. Chen. Negative flame speed in an unsteady 2-D premixed flame: A computational study. In *Twenty-Sixth Symposium (International) on Combustion*, pages 323–329, Pittsburgh, 1996. The Combustion Institute.

[3] Richard L. Bechtold. *Alternative Fuels Guidebook: Properties, Storage, Dispensing, and Vehicle Facility Modifications*. Society of Automotive Engineers, Inc., 1997.

[4] U.S. Department of Energy. Monthly Energy Review-October, 1995. Technical Report DOE/EIA-0035(95/10), U.S. Department of Energy, October 1995.

[5] National Research Council. *Fuels to Drive our Future*. National Academy Press, Washington, D.C., 1990.

[6] J.-Y. Ren, W. Qin, F.N. Egolfopoulos, H. Mak, and T.T. Tsotsis. Methane reforming and its potential effect on the efficiency and pollutant emissions of lean methane-air combustion. *Chemical Engineering Science*, 56:1541–1549, 2001.

[7] Hailin Li, G.A. Karim, and A. Sohrabi. Knock and combustion characteristics of CH_4, CO, H_2 and their binary mixtures. *SAE Technical Paper Number 2003-01-3088*, 2003.

[8] G.R. James, P.T. Richards, and S.A. Wilmes. Methanol vs. Ethanol - 1997. In J.G. Reynolds and M.R. Khan, editors, *Designing Transportation Fuels for a Cleaner Environment*, chapter 7, pages 79–90. Academic Press, Inc., 1999.

[9] Thierry Poinsot and Denis Veynante. *Theoretical and Numerical Combustion*. R.T. Edwards, Inc., 2001.

[10] S.M. Candel and T.J. Poinsot. Flame stretch and the balance equation for the flame area. *Combustion Science and Technology*, 70:1–15, 1990.

[11] J.O. Sinibaldi, C.J. Mueller, and J.F. Driscoll. Local flame propagation speeds along wrinkled, unsteady, stretched premixed flames. In *Twenty-Seventh Symposium (International) on Combustion*, pages 827–832, Pittsburgh, 1998. The Combustion Institute.

[12] T. Echekki and J.H. Chen. Analysis of the contribution of curvature to premixed flame propagation. *Combustion and Flame*, 118:308–311, 1999.

[13] M. Mizomoto, Y. Asaka, S. Ikai, and C.K. Law. Effects of preferential diffusion on the burning intensity of curved flames. In *Twentieth Symposium (International) on Combustion*, pages 1933–1939, Pittsburgh, 1984. The Combustion Institute.

[14] C.K. Law, P. Cho, M. Mizomoto, and H. Yoshida. Flame curvature and preferential diffusion in the burning intensity of bunsen flames. In *Twenty-First Symposium (International) on Combustion*, pages 1803–1809, Pittsburgh, 1986. The Combustion Institute.

[15] T. G. Scholte and P. B. Vaags. Burning velocities of mixtures of hydrogen, carbon monoxide, and methane with air. *Combustion and Flame*, 3:511–524, 1959.

[16] C.M. Vagelopolous and F.N. Egolfopoulos. Laminar flame speeds and extinction strain rates of mixtures of carbon monoxide with hydrogen, methane, and air. In *Twenty-Fifth Symposium (International) on Combustion*, pages 1317–1323, Pittsburgh, 1994. The Combustion Institute.

[17] B. E. Milton and J. C. Keck. Laminar burning velocities in stoichiometric hydrogen and hydrogen-hydrocarbon gas mixtures. *Combustion and Flame*, 58:13–22, 1984.

[18] H. Kido, S. Huang, K. Tanoue, and T. Nitta. Improving the combustion performance of lean hydrocarbon mixtures by hydrogen addition. *JSAE Review*, 15(2):165–170, 1994.

[19] H. Kido, M. Nakahara, and K. Nakashima. A study on premixed turbulent combustion of hydrogen including hydrocarbon. *AIAA-2003-4638*, 2003.

[20] G. Yu, C. K. Law, and C. K. Wu. Laminar flame speeds of hydrocarbon + air mixtures with hydrogen addition. *Combustion and Flame*, 63:339–347, 1986.

[21] E. Sher and N. Ozdor. Laminar burning velocities of n-butane/air mixtures enriched with hydrogen. *Combustion and Flame*, 89:214–220, 1992.

[22] J.-Y. Ren, W. Qin, F.N. Egolfopoulos, and T.T. Tsotsis. Strain-rate effects on hydrogen-enhanced lean premixed combustion. *Combustion and Flame*, 124:717–720, 2001.

[23] R.W. Schefer. Combustion of hydrogen-enriched methane in a lean premixed swirl-stabilized burner. In *Twenty-Ninth Symposium (International) on Combustion*, pages 843–851, Pittsburgh, 2002. The Combustion Institute.

[24] T. Echekki and J.H. Chen. Unsteady strain rate and curvature effects in turbulent premixed methane-air flames. *Combustion and Flame*, 106:184–202, 1996.

[25] J.O. Sinibaldi, J.F. Driscoll, C.J. Mueller, J.M. Donbar, and C.D. Carter. Propagation speeds and stretch rates measured along wrinkled flames to assess the theory of flame stretch. *Combustion and Flame*, 133:323–334, 2003.

[26] W.L. Roberts, J.F. Driscoll, M.C. Drake, and L.P. Goss. Images of quenching of a flame by a vortex - to quantify regimes of turbulent combustion. *Combustion and Flame*, 94:58–69, 1993.

[27] T. Poinsot, D. Veynante, and S. Candel. Diagrams of premixed turbulent combustion based on direct simulation. In *Twenty-Third Symposium (International) on Combustion*, pages 613–619, Pittsburgh, 1990. The Combustion Institute.

[28] T. Poinsot, D. Veynante, and S. Candel. Quenching processes and premixed turbulent combustion diagrams. *Journal of Fluid Mechanics*, 228:561–606, 1991.

[29] G. Patnaik and K. Kailasanath. A computational study of local quenching in flame-vortex interactions with radiative losses. In *Twenty-Seventh Symposium (International) on Combustion*, pages 711–717, Pittsburgh, 1998. The Combustion Institute.

[30] G.P. Smith, D.M. Golden, M. Frenklach, N.W. Moriarty, B. Eiteneer, M Goldenberg,

C.T. Bowman, K. Hanson, R, S. Song, Jr. Gardiner, W.C., V.V. Lissianski, and Z. Qin. GRI-Mech 3.0. *http://www.me.berkeley.edu/gri_mech/*, 1999.

[31] R. J. Kee, J. F. Grcar, M. D. Smooke, and J. A. Miller. A FORTRAN Program for Modeling Steady Laminar One-Dimensional Premixed Flames. Technical Report SAND85-8240, Sandia National Labs, Livermore, CA, 1993.

[32] A.E. Lutz, R.J. Kee, J.F. Grcar, and F.M. Rupley. OPPDIF: A FORTRAN Program for Computing Opposed-Flow Diffusion Flames. Technical Report SAND96-8243, Sandia National Laboratories, Livermore, CA, 1997.

[33] R. J. Kee, F. M. Rupley, and J. A. Miller. Chemkin-II: A FORTRAN Chemical Kinetics Package for the Analysis of Gas Phase Chemical Kinetics. Technical Report SAND89-8009B, Sandia National Laboratories, Livermore, CA, 1993.

[34] H. Tennekes and J. L. Lumley. *A First Course in Turbulence*. MIT Press, 1972.

[35] S. Turns. *An Introduction to Combustion: Concepts and Applications*. McGraw-Hill, 1999.

[36] J.H. Chen, T. Echekki, and W. Kollmann. The mechanism of two-dimensional pocket formation in lean premixed methane-air flames with implications to turbulent combustion. *Combustion and Flame*, 116(1):15–48, 1999.

[37] J.H. Chen and H.G. Im. Correlation of flame speed with stretch in turbulent premixed methane-air flames. *Twenty-seventh symposium (international) on combustion, the combustion institute*, pages 819–826, 1998.

[38] R. J. Kee, G. Dixon-Lewis, J. Warnatz, M. E. Coltrin, and J. A. Miller. The Chemkin Transport Database. Technical Report SAND86-8246, Sandia National Laboratories, Livermore, CA, 1986.

[39] G. Dixon-Lewis. Flame structure and flame reaction kinetics II: Transport phenomena in multicomponent systems. *Proceedings of the Royal Society*, A.307:111–135, 1968.

[40] R.J. Kee, G. Dixon-Lewis, J. Warnatz, M.E. Coltrin, and J.A. Miller. A FORTRAN Computer Code Package for the Evolution of Gas-Phase Multicomponent Transport Properties. Technical Report SAND86-8246, Sandia National Laboratories, Livermore, CA, 1986.

[41] C. P. Stone. *Large-Eddy Simulation of Combustion Dynamics in Swirling Flows*. PhD thesis, School of Aerospace Engineering, Georgia Institute of Technology, Atlanta, GA, March 2003.

[42] R. MacCormack. The effects of viscosity in hyper-velocity impact cratering. *AIAA Paper 69-354*, 1969.

[43] V. Sankaran. *Sub-grid Combustion Modeling for Compressible Two-Phase Reacting Flows*. PhD thesis, School of Aerospace Engineering, Georgia Institute of Technology, Atlanta, GA, December 2003.

[44] C.C. Nelson. *Simulations of Spatially Evolving Compressible Turbulence Using a Local Dynamic Subgrid Model*. PhD thesis, School of Aerospace Engineering, Georgia Institute of Technology, Atlanta, GA, December 1997.

[45] M. Baum, T. Poinsot, and D. Thevenin. Accurate boundary conditions for multicomponent reactive flows. *Journal of Computational Physics*, 116:247–261, 1994.

[46] K. W. Thompson. Time-dependent boundary conditions for hyperbolic systems. *Journal of Computational Physics*, 68:1–24, 1987.

[47] T. Poinsot and S. K. Lele. Boundary conditions for direct simulations of compressible viscous flows. *Journal of Computational Physics*, 101:104–129, 1992.

[48] D. H. Rudy and J. C. Strikwerda. A nonreflecting outflow boundary condition for subsonic Navier-Stokes calculations. *Journal of Computational Physics*, 36:55–70, 1980.

[49] G. W. Hedstrom. Non-reflecting boundary conditions for nonlinear hyperbolic systems. *Journal of Computational Physics*, 30:222–237, 1979.

[50] H. Lamb. *Hydrodynamics 6th Ed.* Cambridge University Press, 1932.

[51] C.J. Sung, C.K. Law, and J.-Y. Chen. An augmented reduced mechanism for methane oxidation with comprehensive global parametric validation. In *Twenty-Seventh Symposium (International) on Combustion*, pages 295–304, Pittsburgh, 1998. The Combustion Institute.

[52] R. J. Kee, F. M. Rupley, and J. A. Miller. The Chemkin Thermodynamic Database. Technical Report SAND87-8215B, Sandia National Laboratories, Livermore, CA, 1987.

[53] R. J. Kee, Miller J. A., G. H. Evans, and G. Dixon-Lewis. A computational model of the structure and extinction of strained, opposed flow premixed methane-air flames. In *Twenty-Second Symposium (International) on Combustion*, pages 1479–1494, Pittsburgh, 1986. The Combustion Institute.

[54] T. von Karman. *NACA Technical Memorandum 1092.* 1921.

[55] S.B. Pope. Computationally efficient implementation of combustion chemistry using *in situ* adaptive tabulation. *Combustion Theory and Modelling*, 1:41–63, 1997.

[56] M. Embouazza, D.C. Haworth, and N. Darabiha. Implementation of detailed chemical mechanisms into multidimensional CFD using in situ adaptive tabulation: Application to HCCI engines. *SAE Paper No. 2002-01-2773*, 2002.

[57] N. Peters. *Turbulent Combustion.* Cambridge University Press, 2000.

[58] P. Flohr and H. Pitsch. A turbulent flame speed closure model for LES of industrial burner flows. In *Proceedings of the 2000 Summer Program.* Center for Turbulence Research, 2000.

[59] V. L. Zimont. The theory of turbulent combustion at high Reynolds numbers. *Combustion, Explosions, and Shock Waves*, 15:305–311, 1979.

VITA

On the night of July 7^{th}, 1979, Justin David Weiler was born, the third of three sons, to Gary and Robin Weiler in Rome, New York. He received his secondary education from the Adirondack Central School in Boonville, New York and, upon graduation, attended the Rochester Institute of Technology (RIT) from which he received his Bachelor of Science degree in Mechanical Engineering. As an undergraduate, he specialized in Aerospace studies, including aerodynamics and propulsion, and held multiple co-op positions with TRW Aeronautical Systems in Utica, New York, and the Thermal Analysis Lab at RIT. While working in the Thermal Analysis Lab, he managed and participated in contracted research projects for IBM, and the U.S. Army, under the advisement of Dr. Satish Kandlikar. In the Spring of 2002, he accepted a research assistantship from the Daniel Guggenheim School of Aerospace Engineering at Georgia Tech. That Summer, he joined the Computational Combustion Lab under the guidance of Dr. Suresh Menon.